# SANDIA REPORT

SAND2006-6286
Unlimited Release
Printed October 2006

# Solution-Verified Reliability Analysis and Design of Bistable MEMS Using Error Estimation and Adaptivity

Brian M. Adams, Barron J. Bichon, Brian Carnes, Kevin D. Copps,
Michael S. Eldred, Matthew M. Hopkins, David C. Neckels,
Patrick K. Notz, Samuel R. Subia, and Jonathan W. Wittwer

Prepared by
Sandia National Laboratories
Albuquerque, New Mexico 87185 and Livermore, California 94550

Sandia is a multiprogram laboratory operated by Sandia Corporation,
a Lockheed Martin Company, for the United States Department of Energy's
National Nuclear Security Administration under Contract DE-AC04-94-AL85000.



Issued by Sandia National Laboratories, operated for the United States Department of Energy by Sandia Corporation.



Available to DOE and DOE contractors from
U.S. Department of Energy
Office of Scientific and Technical Information
P.O. Box 62
Oak Ridge, TN 37831

Telephone: (865) 576-8401
Facsimile: (865) 576-5728
E-Mail: reports@adonis.osti.gov
Online ordering: http://www.osti.gov/bridge

Available to the public from
U.S. Department of Commerce
National Technical Information Service
5285 Port Royal Rd
Springfield, VA 22161

Telephone: (800) 553-6847
Facsimile: (703) 605-6900
E-Mail: orders@ntis.fedworld.gov
Online ordering: http://www.ntis.gov/help/ordermethods.asp?loc=7-4-0#online

SAND2006-6286
Unlimited Release
Printed October 2006

# Solution-Verified Reliability Analysis and Design of Bistable MEMS Using Error Estimation and Adaptivity

Brian M. Adams, Barron J. Bichon, Michael S. Eldred
Optimization and Uncertainty Estimation Department

Brian Carnes, Kevin D. Copps, David C. Neckels
Advanced Computational Mechanics Architectures Department

Matthew M. Hopkins, Patrick K. Notz
Multiphase and Nanoscale Transport Processes Department

Samuel R. Subia
Thermal/Fluid Computational Engineering Sciences Department

Jonathan W. Wittwer
MEMS Core Technologies Department

Sandia National Laboratories
P.O. Box 5800
Albuquerque, NM 87185

**Abstract**

This report documents the results for an FY06 ASC Algorithms Level 2 milestone combining error estimation and adaptivity, uncertainty quantification, and probabilistic design capabilities applied to the analysis and design of bistable MEMS. Through the use of error estimation and adaptive mesh refinement, solution verification can be performed in an automated and parameter-adaptive manner. The resulting uncertainty analysis and probabilistic design studies are shown to be more accurate, efficient, reliable, and convenient.

# Contents

**Contents** **5**

**List of Figures** **8**

**List of Tables** **11**

**Executive Summary** **13**

**1 Introduction and Motivation** **15**

1.1 Reliability Analysis and Design . . . . . 16

1.2 Error Estimation . . . . . 18

1.3 Motivating Application: Bistable MEMS . . . . . 19

1.4 Numerical Challenges . . . . . 23

**2 Technical Components** **25**

2.1 Elasticity Model . . . . . 25

2.2 Error Estimation . . . . . 28

2.2.1 Surface Force Quantity of Interest . . . . . 28

2.2.2 A Posteriori Error Estimation for the Surface Force . . . . . 29

2.2.3 Gradient Recovery Operator . . . . . 30

2.2.4 Surface Force Error Estimator . . . . . 31

2.2.5 Global ZZ Estimator . . . . . 32

2.2.6 Adaptive Mesh Refinement Strategy . . . . . 33

2.2.7 Error Correction of the Surface Force . . . . . 34

2.3 Reliability Analysis . . . . . 35

2.3.1 Mean Value . . . 36
2.3.2 MPP Search Methods . . . 37
2.3.2.1 Limit state approximations . . . 39
2.3.2.2 Probability integrations . . . 42
2.3.2.3 Hessian approximations . . . 43
2.3.2.4 Optimization algorithms . . . 44
2.3.2.5 Warm starting of MPP searches . . . 44
2.4 Reliability-Based Design Optimization . . . 44
2.4.1 Bi-level RBDO . . . 45
2.4.2 Sequential/Surrogate-based RBDO . . . 47

**3 Computational Model and Results 49**

3.1 MEMS Computational Model . . . 49
3.1.1 Geometry, Design and Uncertain Variables, and Boundary Conditions . . . 49
3.1.2 Bistable MEMS Simulation and Baseline Results . . . 51
3.2 Error Estimation Results . . . 55
3.2.1 Error Estimation for Uniform Meshes . . . 55
3.2.2 Adaptive Mesh Refinement . . . 61
3.3 Parameter Study Results . . . 73
3.3.1 Uncertain variables . . . 73
3.3.2 Design variables . . . 77
3.4 Uncertainty Quantification Results . . . 78
3.5 Probabilistic Design Results . . . 91

**4 Accomplishments and Conclusions 97**

4.1 Observations on error estimation and adaptivity . . . 98
4.2 Observations on UQ and RBDO . . . 99

4.3 Accomplishments and Capability Development . . . . . 101

**References** **103**

# List of Figures


1.1 Scanning electron micrograph of a MEMS bistable mechanism . . . . . 21

1.2 Schematic of force–displacement curve for bistable MEMS mechanism including stability of equilibria. . . . . 21

1.3 Schematic of a tapered beam bistable mechanism in as-fabricated position (not to scale). . . . . 22

1.4 Contour plot of $F_{min}(\mathbf{d}, \mathbf{x})$ as a function of uncertain variables. . . . . 23

2.1 Typical nodal patch for the gradient recovery operator . . . . . 32

3.1 Design parameters for the tapered-beam fully-compliant bistable mechanism . . . . . 50

3.2 Boundary conditions and location of surface where force is calculated . . 51

3.3 Baseline force–displacement curve with selected points . . . . . 53

3.4 Von Mises stress on displaced beam for selected time steps . . . . . 54

3.5 Coarse uniform 200 element mesh. ($y$ axis scaled by 10) . . . . . 55

3.6 Dual displacement solution at time step 32 . . . . . 56

3.7 Force–displacement curves for uniform meshes of linear elements . . . . . 57

3.8 Estimated and exact error in the surface force for uniform meshes of linear elements. . . . . 59

3.9 Force error effectivity for uniform meshes of linear elements. . . . . 60

3.10 Exact error and effectivity for uniform meshes at selected time steps . . 60

3.11 Exact error for adaptive meshes using $\eta^Q$ and $\eta^{ZZ}$. . . . . 63

3.12 Effectivity for adaptive meshes using $\eta^Q$. . . . . 64

3.13 Exact and estimated error for adaptive meshes using $\eta^Q$ for all iterations. 66

3.14 Exact error for adaptive meshes using $\eta^{ZZ}$ for all iterations. . . . . 67

3.15 Exact error for meshes adapted using $\eta^Q$ and $\eta^{ZZ}$ at selected time steps. 67

3.16 Effectivity for adaptive meshes using $\eta^Q$ at selected time steps. . . . . 68

3.17 Refined meshes using $\eta^Q$ near right end of beam . . . . . 69

3.18 Refined meshes using $\eta^{ZZ}$ near right end of beam . . . . . 70

3.19 Error rates for corrected force at selected time steps using $\eta^Q$. . . . . 71

3.20 Smoothing by error correction for meshes adapted using $\eta^Q$ . . . . . 72

3.21 Estimated error in force as a function of uncertain variables. . . . . 74

3.22 Exact error in force as a function of uncertain variables. . . . . 75

3.23 Estimated force error relative to force magnitude as a function of uncertain variables. . . . . 76

3.24 Estimated error in force as a function of design variables. . . . . 77

3.25 Possible paths used to compute approximate and reference force-displacement curves. . . . . 79

3.26 CDFs generated with reference mesh and several linear element meshes to demonstrate convergence. . . . . 80

3.27 Plots of CDF error versus nodes using AMV$^2$+ from Table 3.4. . . . . 81

3.28 CDFs generated using AMV$^2$+ PMA with quadratic element meshes. . . 82

3.29 CDFs generated with reference mesh (3200 quadratic elements) and two coarse linear element meshes, with and without error-correction. . . 84

3.30 CDFs generated with reference mesh (3200 quadratic elements) and two fine linear element meshes, with and without error-correction. . . . . 85

3.31 CDFs generated using various reliability algorithm formulations with reference mesh. . . . . 86

3.32 CDFs generated using reference mesh and $\eta^{ZZ}$-adaptive mesh with 200 initial linear elements. . . . . 88

3.33 CDFs generated using reference mesh and $\eta^Q$-adaptive meshes, with and without error correction. . . . . 89

3.34 Central finite differences for surface force and adaptivity using $\eta^Q$ . . . . . 90

3.35 Response PDF control of mean and right tail . . . . . 92

3.36 Response PDF control of both tails . . . . . 93

3.37 Optimal force–displacement curves resulting from RBDO with various meshes. . . . . 95

3.38 Verified force–displacement curves generated using reference mesh. . . . . 96

# List of Tables


3.1 Uncertain variables $\mathbf{x} = [\Delta W, S_r]$ used in UQ and RBDO. . . . . 50

3.2 Values of tapered beam geometric parameters $\mathbf{d}$ used in UQ studies. . . 52

3.3 Default parameters for adaptive mesh refinement . . . . . 61

3.4 Computational cost and error for 13 point CDF generated with various methods and meshes. . . . . 83

3.5 Computational cost and error for 13 point CDF generated with various adaptive meshes. . . . . 87

3.6 RBDO results for MEMS bistable mechanism. . . . . 94

4.1 Comparison of solution verification strategies: H = high, M = medium, L = low . . . . . 98

# Executive Summary

An important component of verification and validation of computational models is solution verification, which focuses on the convergence of the desired solution quantities as one refines the spatial and temporal discretizations and iterative controls. Uncertainty analyses often treat solution verification as a separate issue, hopefully through the use of *a priori* grid convergence studies and selection of numerical models with acceptable discretization errors. When these convergence analyses are performed off-line, they may result in a relatively expensive model that has been verified for a single set of nominal design/uncertain parameters. With the advent of finite element error estimation techniques, approaches for on-line and parameter-adaptive solution verification become possible and hold potential for improving overall accuracy and efficiency.

In this milestone, a tighter connection between solution verification and uncertainty quantification is investigated. In particular, error estimation techniques, using global norm and quantity of interest error estimators, are applied to the nonlinear structural analysis of microelectromechanical systems (MEMS). Two primary approaches for uncertainty quantification are then developed: an error-corrected approach, in which simulation results are directly corrected for discretization errors, and an error-controlled approach, in which estimators are used to drive adaptive h-refinement of mesh discretizations. The former requires quantity of interest error estimates that are quantitatively accurate, whereas the latter can employ any estimator that is qualitatively accurate. Combinations of these error-corrected and error-controlled approaches are also explored. Each of these techniques treats solution verification and uncertainty analysis as a coupled problem, recognizing that the simulation errors may be influenced by, for example, conditions present in the tails of input probability distributions. The most effective and affordable of these approaches are carried forward in probabilistic design studies for robust and reliable operation of a bistable MEMS device.

The key milestone conclusion is that on-line solution verification approaches show significant promise. In terms of accuracy, controlling or correcting for errors leads to higher confidence in the uncertainty analysis and probabilistic design recommendations. In terms of computational expense, the use of error-correction on coarse meshes (from adjoint-based quantity of interest error estimates) is shown to result in less than 10% of the simulation expense of fully converged meshes with comparable accuracy. In terms of computational reliability, the parameter-adaptive nature of the on-line approach precludes the possibility of using computational model results that are converged for one set of parameters, but not for another. And in terms of convenience, the potential elimination of the need for manual convergence studies

should significantly reduce overhead for analysts and designers. Future directions for developing a more seamless production capability are also identified.

This milestone crosscuts multiple centers, with components including the uncertainty analysis and probabilistic design capabilities from DAKOTA (1400), global norm and quantity of interest error estimates from Coda (1500), nonlinear mechanics analysis from Aria (1500), data structures and $h$-refinement algorithms from SIERRA (1500), and MEMS model development and MESA program relevance (1700). Many new capabilities have been developed within these codes for use in this milestone.

# Chapter 1

# Introduction and Motivation

Verification and validation of computational models is an increasingly important mission objective as the Department of Energy shifts from primarily test-based certification approaches to approaches based more on modeling and simulation. An important component of verification and validation is the area of solution verification, which focuses on the convergence of the desired solution quantities as one refines the spatial and temporal discretizations and iterative controls [47, 3, 11]. Uncertainty analyses often treat solution verification as a separate issue, hopefully through the use of *a priori* grid convergence studies and selection of numerical models with acceptable discretization errors. When these convergence analyses are performed off-line, they may result in a relatively expensive model that has been verified for a single set of nominal design and/or uncertain parameters. With the advent of finite element error estimation techniques, approaches for on-line and parameter-adaptive solution verification become possible and hold potential for improving overall accuracy and efficiency.

In this milestone, a tighter connection between solution verification and uncertainty quantification is investigated. In particular, error estimation techniques, using energy norm and quantity of interest error estimators, are applied to the nonlinear structural analysis of microelectromechanical systems (MEMS). Two primary approaches for uncertainty quantification are then developed: an error-corrected approach, in which simulation results are directly corrected for discretization errors, and an error-controlled approach, in which estimators are used to drive uniform and adaptive h-refinement of mesh discretizations. The former requires quantity of interest error estimates that are quantitatively accurate, whereas the latter can employ any estimator and only requires qualitative accuracy. Combinations of these error-corrected and error-controlled approaches are also explored. Each of these techniques treats solution verification and uncertainty analysis as a coupled problem, recognizing that the simulation errors may be influenced by, for example, conditions present in the tails of input probability distributions.

The most effective and affordable of these solution-verified uncertainty quantification approaches are carried forward in probabilistic design optimization studies. Reliability-based design optimization (RBDO) methods are employed to optimize the shape of a bistable MEMS device and obtain designs that are both robust and reliable with

respect to manufacturing uncertainties.

## 1.1 Reliability Analysis and Design

The technique selected for performing uncertainty quantification in this study is reliability analysis. Reliability analysis methods are probabilistic algorithms for quantifying the effect of input uncertainties on response metrics of interest. In particular, they compute approximate response function distribution statistics based on specified probability distributions for input random variables. These methods are often more efficient at computing statistics in the tails of the response distributions (events with low probability) than sampling-based approaches because the number of samples required to resolve a low probability can be prohibitive. Thus, these methods, as their name implies, are often used in a reliability context for assessing the probability of failure of a system when confronted with an uncertain environment.

A reliability analysis that captures the effect of random variables on response metrics for an inaccurate, inappropriate, or unconverged model is of limited utility. For this reason, it is prudent to first perform verification and validation activities for the computational model of interest. One portion of this is the area of solution verification, as described previously. Using finite element error estimation techniques, a number of different conceptual formulations are possible for incorporating solution verification within uncertainty analysis. If the discretization errors are not driven toward zero through the use of mesh refinement (in an error-controlled approach), then they need to be included within the uncertainty analysis (in an error-corrected approach) using one of the following conceptual models:

1. given error estimates for the response quantities of interest, model the discretization error as a deterministic quantity that can correct results for a particular mesh discretization. The results generated from the uncertainty analysis are then projected towards the fully converged results, but uncertainties in the accuracy of the error estimates are not modeled.

2. given error estimates for the response quantities of interest, model the true discretization error as being uncertain since the estimate will not in general be exact. In particular, model the discretization error as a random variable for which the deterministic error estimate generated for the current mesh discretization is interpreted as a realization (e.g., the expected value) of the random variable.

3. given error bounds for the response quantities of interest, model the true discretization error as an additional uncertainty using a bounded distribution within the UQ analysis. Given no additional data on the error distribution, modeling the error as an interval distribution and using epistemic uncertainty analysis approaches would be appropriate (which could then be combined with

the aleatoric components within an approach such as second-order/imprecise probability).

Put another way, one can attempt to eliminate the errors (through uniform or adaptive mesh refinement), account for the errors deterministically (approach 1), or account for the errors probabilistically (approaches 2 and 3). In this study, we employ approach 1, and do not model the discretization error as a random quantity. In addition, error bounds are much more challenging to obtain and are outside the scope of this report. Approaches 2 and 3 are directions for future research.

Classical reliability analysis methods include Mean-Value First-Order Second-Moment (MVFOSM), First-Order Reliability Method (FORM), and Second-Order Reliability Method (SORM) [38]. More recent methods seek to improve the efficiency of FORM analysis through limit state approximations, including the local and multipoint approximations of Advanced Mean Value methods (AMV/AMV+) [72] and Two-point Adaptive Nonlinearity Approximation-based methods (TANA) [66, 75], respectively. Each of the FORM-based methods can be employed for "forward" or "inverse" reliability analysis through the reliability index approach (RIA) or performance measure approach (PMA), respectively [64]. Recent algorithmic advances in reliability analysis are described in [26] and [27], and are summarized in Section 2.3.

The capability to assess reliability is broadly useful within a design optimization context, and reliability-based design optimization methods are popular approaches for designing systems while accounting for uncertainty. RBDO approaches may be broadly characterized as bi-level (in which the reliability analysis is nested within the optimization) [5], sequential (in which iteration occurs between optimization and reliability analysis) [73, 24], or unilevel (in which the design and reliability searches are combined into a single optimization) [2]. Bi-level RBDO methods are simple and general-purpose, but can be computationally demanding. Sequential and unilevel methods seek to reduce computational expense by breaking the nested relationship through the use of iterated/surrogate or simultaneous approaches, respectively. Due to the analytic structure of the reliability analysis formulations, each of these techniques can take advantage of analytic sensitivities of the reliability results with respect to design variables, for cases where the design variables either define distribution parameters for the uncertain variables or are separate from the uncertain variables. Recent algorithmic advances in bi-level and sequential RBDO are described in [26] and [27], and Section 2.4 summarizes these algorithms. The design studies in this report focus on bilevel RBDO methods using semi-analytic design sensitivities of the reliability metrics with respect to the design variables.

## 1.2 Error Estimation

Our test problem for solution-verified reliability analysis comes from the structural mechanics simulation of a bistable MEMS switch. The geometric nonlinearity and large displacements of the problem motivate a fully nonlinear finite strain 2D elasticity model for the bistable switch. In order to compute an estimate of the error in the force at each displacement step resulting from the mesh discretization, an *a posteriori* error estimate was derived for this quantity of interest. This "goal-oriented" estimator is defined by integrating the finite element residual weighted by the error in an associated global linearized adjoint problem. Local element contributions to the global error estimate can then be used to drive adaptive mesh refinement. In this case, the mesh is adapted to minimize the error in the force, which is known as goal-oriented adaptivity.

When mathematical models are approximated by discrete numerical methods such as finite elements, finite differences, finite volumes, etc., it is natural and essential to quantify and minimize the numerical error resulting from the discrete approximation. The total error in a calculation can include components from model selection error, geometry error, initial and boundary condition error, material coefficient error, mesh discretization error, linearization error, quadrature error, iterative solver error, and roundoff error, to name a few. The task of controlling mesh discretization error is accomplished by methods for *a posteriori* error estimation and adaptivity, which seek to provide computable estimates of the numerical error as well as adaptive procedures for reducing the error. The error estimates can be for global norms of the solution error or for error in functionals of the solution, known as quantities of interest. In the case of finite element methods, the adaptive procedures include local refinement/coarsening of the mesh ($h$–adaptivity), local enrichment of the finite element shape functions ($p$–adaptivity), and local adjustment of the mesh topology and locations ($r$–adaptivity).

Development of finite element based error estimates for the error in global norms begin in the 1970s with the work of Carey [18], Babuška and Rheinboldt [10], and others [7, 12]. Major types of error estimators for global norms include explicit residual, implicit residual, and recovery estimators (for a complete discussion see [3, 11, 19] and the references within). In the 1990s, a new class of error estimators began to be developed which are designed to provide error estimators in various outputs computed from the finite element solution, the so–called quantity of interest or goal–oriented error estimators. Early work by Babuška and Miller [8, 9] and Eriksson and Johnson [32] led the way to the use of an auxiliary problem, the so–called dual or adjoint problem. Eventually, a number of authors including Estep [33, 35], Becker and Rannacher [13], Rannacher [56], Prudhomme and Oden [52], Paraschivoiu and Patera [51], and Larsson et al. [45] introduced various error estimators based on the adjoint approach. In almost all of these cases, the error in the quantity is represented by a weighted residual expression, where the weights are the error in the adjoint problem.

For the MEMS application that we study in this work, the quantity of interest is the force needed to move the beam for a prescribed displacement. Since the displacement and force are both specified on a surface of the beam, the quantity is a surface integral of the force along this surface in a particular direction. Such a quantity does not fit directly in the standard theory of error estimators for the quantity of interest due to a technical problem with the solution space containing the solutions to the continuous variational form of the elasticity equations. However, this problem can be avoided by using the well–known technique in solid mechanics of postprocessing the stress to get a more accurate surface force. In this case, we replace the exact surface integral of the normal stress with a volume integral of the stress against a particular weight function that vanishes away from the surface. Such postprocessing techniques were used with error estimation by Babuška and Miller [8, 9] in the case of point values of displacement and stress, and in the case of stress intensity factors for crack singularities. Other approaches to this problem include regularization of the surface integral by integrating over a thin volume adjacent to the surface [13] or direct use of the surface integral of the force [57]. Recently, Wildey et al. [67] used an adjoint problem with a prescribed Dirichlet boundary condition along the surface. The form of the error estimate used the dual solution along with integration by parts to derive an estimate for the surface integral of the force. We have modified this approach for use with the postprocessed volume integral of the surface force and to handle the nonlinearities of our elasticity model.

An important issue with quantity of interest estimators is the approximation of the solution of the adjoint problem [45]. Several authors have proposed that the adjoint solution be approximated using a higher order discretization than the one used for the original model [34, 67]. However, it has also been proposed to solve the adjoint problem using the same discretization as the original problem [13, 56, 52]. In the latter case, some postprocessing of the adjoint solution is needed in order to derive a useful error estimate. In this work we solve the adjoint problem using the same approximation space as for the original problem and use a gradient recovery operator to recover a higher order gradient. This choice is justified since the only term in the weighted residual involves the error in the gradient of the adjoint solution.

## 1.3 Motivating Application: Bistable MEMS

Pre-fabrication design optimization of microelectromechanical systems (MEMS) is an important emerging application of uncertainty quantification (UQ) and reliability-based design optimization (RBDO). Typically crafted of silicon, polymers, metals, or a combination thereof, MEMS serve as micro-scale sensors, actuators, switches, and machines with applications including robotics, biology and medicine, automobiles, RF electronics, and optical displays [4]. Design optimization of these devices is crucial due to high cost and long fabrication times. Uncertainty in the micromachining and etching processes used to manufacture MEMS can lead to large uncertainty in the

behavior of the finished products. RBDO, coupled with computational mechanics models of MEMS, offers a means to quantify this uncertainty and determine a priori the most reliable and robust design that meets performance criteria [1].

Uncertainty and sensitivity analysis techniques [21, 60] that predate modern reliability methods have historically been used to understand variability in systems and these have natural application to MEMS. Recently, Monte Carlo and robust optimization techniques have been explored in this context as well [61]. These tools analyze the expected performance variability or robustness for a particular design.

A compelling technical advantage of microsystems is that, like integrated circuits, they can be batch fabricated for high volume applications. Designing MEMS that are less sensitive to manufacturing process variations results in higher yield of reliable devices. Recognizing the importance of designing reliable and robust systems, researchers have coupled uncertainty analysis and reliability methods with design optimization for MEMS. Many have considered design problems similar to those presented in this paper. For example, Liu, et al., sought designs robust to width variations [46] and Mawardi and Pitchumanu applied robust optimization to resonators [49]. Compliant MEMS were also explored by Maute and Frangopol who investigated topology optimization with reliability-based design methods [48]. Wittwer, et al., united modern uncertainty analysis, model validation, and robust optimization techniques in a comprehensive design method accounting for process uncertainties [69].

In this report, a new tapered beam topology for a fully compliant bistable mechanism is presented. The uncertainty quantification and reliability analysis algorithms in DAKOTA are applied to finite element-based simulations of a compliant bistable micromechanism. Results presented in Sections 3.4 and 3.5 include uncertainty analysis for a particular beam design and RBDO where the beam geometry is optimized to reliably achieve a specified actuation force, while simultaneously reducing predicted force variability due to material properties and manufacturing.

MEMS bistable mechanisms toggle between two stable positions, making them useful as micro switches, relays, and nonvolatile memory. In particular, the focus here is on shape optimization of compliant bistable mechanisms, where instead of mechanical joints, material elasticity and geometry enable the bistability of the mechanism [44, 6, 42]. Figure 1.1 contains an electron micrograph of a MEMS compliant bistable mechanism in its second stable position. The first stable position is the as-fabricated position. Transfer between stable states (moving the shuttle past an unstable equilibrium) is achieved by applying force to the center shuttle via a thermal actuator, electrostatic actuator, or other means.

Bistable switch actuation characteristics depend on the relationship between actuation force and shuttle displacement for the manufactured switch. Figure 1.2 contains a schematic of a typical force–displacement curve for a bistable mechanism. The switch characterized by this curve has three equilibria: $E_1$ and $E_3$ are stable equilibria whereas $E_2$ is an unstable equilibrium (arrows indicate stability). A device with

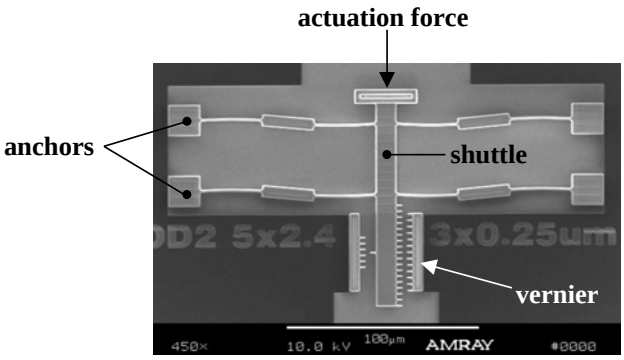


**Figure 1.1.** Scanning electron micrograph of a MEMS bistable mechanism in its second stable position. The attached vernier provides position measurements [68].

such a force–displacement curve could be used as a switch or actuator by setting the shuttle to position $E_3$ as shown in Figure 1.1 (requiring large actuator force $F_{max}$) and then actuating by applying the comparably small force $F_{min}$ in the opposite direction to transfer back through $E_2$ toward the equilibrium $E_1$. One could utilize this force profile to complete a circuit by placing a switch contact near the displaced position corresponding to maximum (closure) force as illustrated. Repeated actuation of the switch relies on being able to reset it with actuation force $F_{max}$.

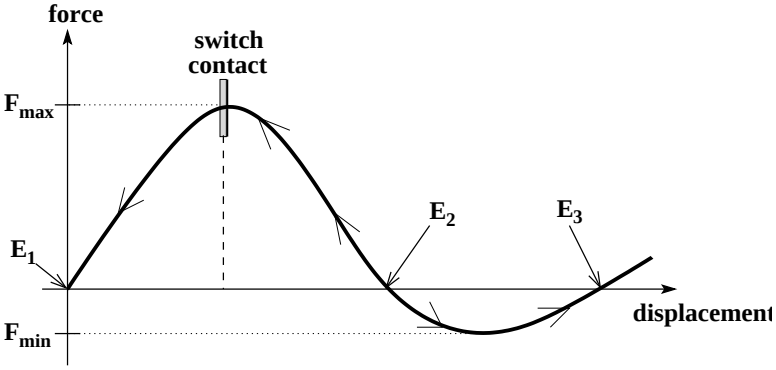


**Figure 1.2.** Schematic of force–displacement curve for bistable MEMS mechanism. The arrows indicate stability of equilibria $E_1$ and $E_3$ and instability of $E_2$.

The device design considered in this paper is similar to that in the electron micrograph in Figure 1.1, for which design optimization has been previously considered [42], as has robust design under uncertainty with mean value methods [69]. The primary structural difference in the present design is the tapering of the legs, shown schematically in Figure 1.3. This topology is a cross between Jensen's fully compliant bistable

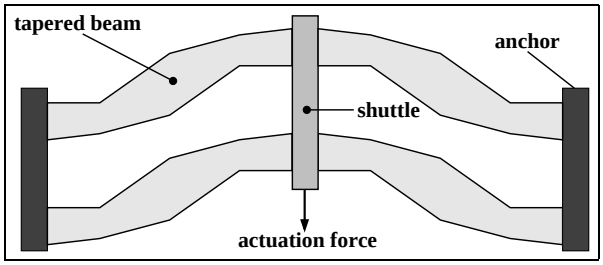


**Figure 1.3.** Schematic of a tapered beam bistable mechanism in as-fabricated position (not to scale).

mechanism [42] and Qiu's thickness-modulated curved beam [53]. As described in the optimization problem below, this tapered geometry offers many degrees of freedom for design.

An appropriately designed bistable switch actuates predictably with prescribed force $\bar{F}_{min}$ and is robust to fabrication variations. The switch investigated here is subject to the following design criteria:

- reliably achieves specified actuation force $\bar{F}_{min} = -5\,\mu$N;
- is bistable ($F_{max} > 0$ and $F_{min} < 0$);
- attains at least $50\,\mu$N force $F_{max}$ at switch contact to reduce electrical contact resistance, but requires no more than $150\,\mu$N actuation force to set;
- unstable point $E_2$ occurs at no more than $8\,\mu$m (limited by the actuator displacement); and
- maximum stress no more than 1200 MPa.

The maximum stress constraint is removed in the analysis and optimization conducted here, since the mathematical model contains singularities where the stress may be infinite. The actual device has stress-reducing fillets, which in a more rigorous analysis would be modeled and therefore accounted for during design optimization. The force–displacement profile of a compliant bistable MEMS device is highly sensitive to design geometry, so one can vary manufactured geometry to achieve these design criteria.

Bistable MEMS devices are often characterized in terms of their structural response at specific points on the device over some operational range. In order to evaluate the bistable MEMS device studied here, Figure 1.1, one must characterize the relationship between actuation force and shuttle displacement over device configurations that include several equilibrium positions. Rather than study the structural displacement response to actuation force, the approach used here is to study the actuation force corresponding to a series of quasi-statically prescribed shuttle displacements,

Figure 1.2. In achieving these configurations the MEMS device experiences finite deformations and large rotations.

## 1.4 Numerical Challenges

Engineering design problems can present significant challenges for reliability analysis methods. In Figure 1.4, we see the results of parameter studies performed in earlier work [1] for the metric $F_{min}(\mathbf{d}, \mathbf{x})$ as a function of the uncertain variables $\mathbf{x}$ for two fixed sets of design variables $\mathbf{d}$. Since the uncertain variables are both normal, the transformation to u-space used by MPP search methods is linear. For the design variable set associated with the left plot the limit state is relatively linear and well-behaved in the range of interest. First-order probability integrations would be sufficiently accurate. For the second design variable set, however, multiple computational challenges are evident. In this case, the limit state has significant nonlinearity (requiring more sophisticated probability integrations) and its simulation can be seen to be unreliable in the left tail of the edge bias (resulting from too flimsy a structure). This highlights a number of difficulties common in engineering applications: nonlinear, nonsmooth, and multimodal limit states and simulation failures caused by, e.g., evaluations in the tails of input distributions. This also implies that error estimates may have a significant parameter dependence (especially for shape parameters evaluated in the tails of probability distributions), such that one could be misled by off-line mesh convergence analyses that are performed for only a single set of nominal parameters.

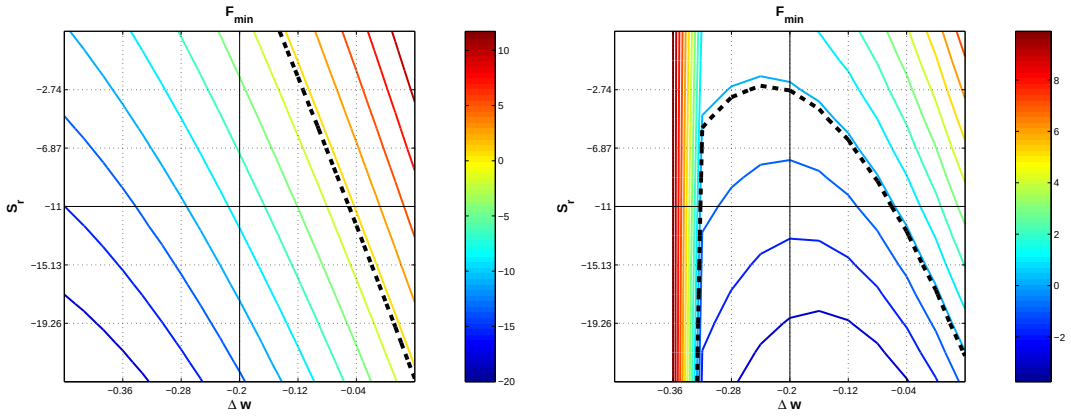


(a) Well-behaved $\mathbf{d}$ (b) Problematic $\mathbf{d}$

**Figure 1.4.** Contour plot of $F_{min}(\mathbf{d}, \mathbf{x})$ as a function of uncertain variables for different design variable sets. Dashed line shows where limit state $g(\mathbf{x}) = F_{min}(\mathbf{x}) = 0$.

In the remainder of this report, Chapter 2 overviews the various technical components of the milestone, Chapter 3 presents computational results, and Chapter 4 provides concluding remarks and future directions.

# Chapter 2

# Technical Components

## 2.1 Elasticity Model

The underlying mathematical model for the bistable MEMS problem is that of planar elasticity; because the problem contains geometric nonlinearities, we must consider large displacements and finite strains. In this analysis the material behavior is modeled using a nonlinear neo-Hookean model. In this section we provide a brief overview of the equations of nonlinear elasticity, develop the weak variational form of the equations, and define the finite element approximation.

Suppose that the reference configuration of a body at some initial state is the domain $\Omega_a$. The physical domain after deformation $\Omega$ is the image of the reference configuration of the body $\Omega_a$ under the deformation map

$$(\boldsymbol{x}_a, t) \mapsto \boldsymbol{x} \equiv \phi(\boldsymbol{x}_a, t). \tag{2.1}$$

Since we are only interested in quasi-static problems in this work, time dependence and the variable $t$ is neglected in what follows. We denote derivatives with respect to $\boldsymbol{x}$ as $\boldsymbol{\nabla}$ and derivatives with respect to $\boldsymbol{x}_a$ as $\boldsymbol{\nabla}_a$.

The deformation map $\phi$ can also be expressed using the displacement map $\boldsymbol{u}(\boldsymbol{x}_a)$ which is defined as

$$\boldsymbol{u}(\boldsymbol{x}_a) \equiv \boldsymbol{x} - \boldsymbol{x}_a = \phi(\boldsymbol{x}_a) - \boldsymbol{x}_a, \quad \boldsymbol{x}_a \in \Omega_a. \tag{2.2}$$

The derivative of the deformation map $\phi$ is the deformation gradient

$$\boldsymbol{F} \equiv \boldsymbol{\nabla}_a \phi = \boldsymbol{\nabla}_a(\boldsymbol{x}_a + \boldsymbol{u}) = \boldsymbol{I} + \boldsymbol{\nabla}_a \boldsymbol{u}. \tag{2.3}$$

The equation for conservation of linear momentum in the current configuration is given by

$$-\boldsymbol{\nabla} \cdot \boldsymbol{T} = \boldsymbol{f}, \quad \boldsymbol{x} \in \Omega. \tag{2.4}$$

Here $\boldsymbol{T}$ is the Cauchy stress tensor which is defined in the deformed configuration $\boldsymbol{x} \in \Omega$. Also $(\boldsymbol{\nabla}\cdot)$ is the divergence operator with respect to the coordinate $\boldsymbol{x}$, and $\boldsymbol{f}$ is the body force vector.

In our analysis of the MEMS beam, we utilize the hyperelastic neo-Hookean model for stress [62, 63]

$$\boldsymbol{T} \equiv \frac{\mu}{|\boldsymbol{F}|}\left(\boldsymbol{F}\boldsymbol{F}^T - \boldsymbol{I}\right) + \frac{\lambda \ln|\boldsymbol{F}|}{|\boldsymbol{F}|}\boldsymbol{I}, \tag{2.5}$$

where $\lambda$ and $\mu$ are the usual Lamé coefficients and $|\cdot|$ denotes the determinant.

In addition to the stresses resulting from external loading, we also include residual stresses that might arise from the manufacturing process. These stress contributions are assumed to be of the form

$$\boldsymbol{T}_{residual} \equiv S_r\,\boldsymbol{I}, \tag{2.6}$$

where the scalar $S_r$ has units of stress. The residual stress is added into the Cauchy stress tensor in order to get the expression for the total stress.

The nonlinearities in this problem arise from several sources. Since the neo-Hookean material model depends upon the equilibrium configuration it is a highly nonlinear function of the unknown displacement $\boldsymbol{u}$. Moreover, the domain $\Omega$ and hence all spatial derivative operators are also functions of displacement.

In order to derive a weak variational formulation, we begin by multiplying the vector-valued conservation law in (2.4) by a vector-valued test function $\boldsymbol{v}$. Integrating by parts over $\Omega$ we derive the equation

$$\int_\Omega \boldsymbol{T} : \boldsymbol{\nabla v}\,\mathrm{d}\Omega - \int_\Gamma (\boldsymbol{T}\,\boldsymbol{n})\cdot\boldsymbol{v}\,\mathrm{d}\Gamma = \int_\Omega \boldsymbol{f}\cdot\boldsymbol{v}\,\mathrm{d}\Omega, \tag{2.7}$$

which is naturally coupled to the neo-Hookean stress law (2.5) in the reference configuration. Here the notation $\boldsymbol{A} : \boldsymbol{B}$ denotes the tensor inner product

$$\boldsymbol{A} : \boldsymbol{B} \equiv \sum_{i,j} A_{ij}\,B_{ji}.$$

We assign Dirichlet boundary conditions to a portion of the domain boundary $\Gamma_D$

$$\boldsymbol{u} = \boldsymbol{u}_D, \tag{2.8}$$

from which we impose the condition $\boldsymbol{v} = \boldsymbol{0}$ for the test functions on $\Gamma_D$. Neumann boundary conditions are specified along $\Gamma_N$, the remainder of the domain boundary $\Gamma$,

$$\boldsymbol{T}\,\boldsymbol{n} = \boldsymbol{g}_N. \tag{2.9}$$

Substituting these boundary conditions into (2.7), we obtain the variational problem for $\boldsymbol{u}$ satisfying (2.8) and

$$\int_\Omega \boldsymbol{T} : \boldsymbol{\nabla v}\,\mathrm{d}\Omega = \int_\Omega \boldsymbol{f}\cdot\boldsymbol{v}\,\mathrm{d}\Omega + \int_{\Gamma_N} \boldsymbol{g}_N\cdot\boldsymbol{v}\,\mathrm{d}\Gamma, \tag{2.10}$$

for all test functions $\boldsymbol{v}$ that vanish on $\Gamma_D$.

Now we can see that the variational problem is a nonlinear function of the displacement, through the stress relation in (2.5) and the various terms depending on $\boldsymbol{u}$ in (2.10). Although this problem can be explicitly linearized, instead we define an abstract nonlinear variational problem using the residual defined by (2.10) in order to simplify the equations needed in the next section. Given an appropriate Sobolev space of functions $\mathcal{V}$ as described in [17], we can define a subspace $V$ as

$$V \equiv \{\boldsymbol{v} \in \mathcal{V} \,|\, \boldsymbol{v}|_{\Gamma_D} = \boldsymbol{0}\}.$$

We will also use the notation

$$\langle \tau, \boldsymbol{v} \rangle_{\mathcal{V}^*,\mathcal{V}} = \langle \tau, \boldsymbol{v} \rangle \,, \quad \tau \in \mathcal{V}^*, \boldsymbol{v} \in \mathcal{V},$$

to denote the duality pairing between a linear functional $\tau$ in the dual space $\mathcal{V}^*$ and a function $\boldsymbol{v} \in \mathcal{V}$. The exact form of value of $\langle \tau, \boldsymbol{v} \rangle$ depends on the functional $\tau$, and may include, for example, integrals of $\tau$ and $\boldsymbol{v}$ and their derivatives over $\Omega$. This notation is convenient for representing variational forms in a generic way as we will do in (2.12). Finally let $\boldsymbol{u}_D$ denote any function in $\mathcal{V}$ that satisfies (2.8), using the same notation as the boundary data $\boldsymbol{u}_D$. The variational problem is then defined abstractly as: find $\boldsymbol{u} \in \boldsymbol{u}_D + V$:

$$\langle R(\boldsymbol{u}), \boldsymbol{v} \rangle = 0, \quad \boldsymbol{v} \in V, \tag{2.11}$$

where the residual functional $R$ is the nonlinear map from $\boldsymbol{u} \in \mathcal{V}$ to $R(\boldsymbol{u}) \in \mathcal{V}^*$ defined by

$$\langle R(\boldsymbol{u}), \boldsymbol{v} \rangle \equiv \int_\Omega \boldsymbol{T} : \boldsymbol{\nabla} \boldsymbol{v} \, \mathrm{d}\Omega - \int_\Omega \boldsymbol{f} \cdot \boldsymbol{v} \, \mathrm{d}\Omega - \int_{\Gamma_N} \boldsymbol{g}_N \cdot \boldsymbol{v} \, \mathrm{d}\Gamma, \quad \boldsymbol{u}, \boldsymbol{v} \in \mathcal{V}. \tag{2.12}$$

For the finite element approximation, we choose a family of finite-dimensional subspaces $V_h$ of $V$. Such a space is typically defined by a mesh $\mathcal{T}_h$ of elements that cover the reference domain $\Omega_a$ and a space of shape functions $V_h(K)$ on each element $K \in \mathcal{T}_h$. For conforming (Galerkin) finite elements, the global space $V_h$ is then defined by

$$V_h \equiv \{\boldsymbol{v} \in V \,:\, \boldsymbol{v}|_K \in V_h(K), \quad \forall \; K \in \mathcal{T}_h\}.$$

Given such a family of spaces $V_h$, the Galerkin finite element approximation is the solution to the problem: find $\boldsymbol{u}_h \in \boldsymbol{u}_{Dh} + V_h$:

$$\langle R(\boldsymbol{u}_h), \boldsymbol{v}_h \rangle = 0, \quad \boldsymbol{v}_h \in V_h, \tag{2.13}$$

where $\boldsymbol{u}_{Dh}$ is an approximation of $\boldsymbol{u}_D$ using the finite element shape functions.

This nonlinear system of equations for the discrete displacement variables can be solved using a nonlinear iterative solver coupled with a linear solver for the resulting sequence of linear systems of equations. For all of the MEMS beam calculations in this work, we used Aria, a Galerkin finite element-based program for coupled-physics

problems implemented in Sandia National Laboratories' Sierra framework of multiphysics codes [25]. In order to solve the nonlinear elasticity model, a neo-Hookean material model (2.5) and a surface force post-processor (described in Section 2.2) was added to Aria.

The simulations are done on quadrilateral meshes using bilinear or biquadratric elements. The nonlinear solver is a Newton iteration with analytical sensitivities and the linear solver is a direct LU solver. When adaptive mesh refinement is used, the continuity of the displacement at hanging nodes is maintained by enforcing hanging node constraints internally in the linear solver.

## 2.2 Error Estimation

Our goal in this section is to derive an error estimator for the surface force over a portion of the boundary. Although there are a wide variety of other design quantities of interest, the surface force has direct relevance to bistable MEMS devices, since they are characterized through an accurate calculation of the nonlinear force-displacement response curves.

### 2.2.1 Surface Force Quantity of Interest

We consider a nonlinear functional $Q$ which is defined to be the $i$-th component of the integrated surface force

$$Q(\boldsymbol{u}) \equiv \int_{\Gamma_0} (\boldsymbol{T}(\boldsymbol{u})\,\boldsymbol{n}) \cdot \mathbf{e}_i \, \mathrm{d}\Gamma, \tag{2.14}$$

where $\mathbf{e}_i$ is the $i$-th unit vector and $\Gamma_0$ is a subset of the Dirichlet boundary ($\Gamma_0 \subset \Gamma_D$). When directly evaluating the approximate force as $Q(\boldsymbol{u}_h)$, this expression is not typically accurate enough for practical use, because it depends on the finite element gradients on $\Gamma_0$ through the stress. Instead, a post-processed surface force may be calculated using the nodal shape functions supported on $\Gamma_0$. First we define a mesh-dependent function $\psi_h$ by setting the value for component $i$ to one at the nodes on $\Gamma_0$ and zero at all other nodes and components. Then the post-processed surface force functional $Q_h$ is defined as

$$Q_h(\boldsymbol{u}) \equiv \int_\Omega \boldsymbol{T}(\boldsymbol{u}) : \boldsymbol{\nabla}\psi_h \, \mathrm{d}\Omega - \int_\Omega \boldsymbol{f} \cdot \psi_h \, \mathrm{d}\Omega + \int_{\Gamma_N} \mathbf{g}_N \cdot \psi_h \, \mathrm{d}\Gamma = \langle R(\boldsymbol{u}), \psi_h \rangle \,. \tag{2.15}$$

When evaluated at the exact solution $\boldsymbol{u}$ to (2.11), we have the equality

$$Q(\boldsymbol{u}) = Q_h(\boldsymbol{u}).$$

Thus it is reasonable to use either $Q$ or $Q_h$ to compute the surface force for the approximate solution $\boldsymbol{u}_h$. In fact, any function that agrees with $\psi_h$ on $\Gamma_D$ will also produce the exact surface force when $\boldsymbol{u}$ is the exact solution.

Because $Q_h(\boldsymbol{u}_h)$ is generally more accurate than $Q(\boldsymbol{u}_h)$, we will focus only on $Q_h$ for the remainder of this work. However, our method should be applicable to the choice of $Q$ as the surface force with some minor modifications.

### 2.2.2 A Posteriori Error Estimation for the Surface Force

We now derive an error estimator for the error in the surface force $Q_h$ defined in (2.15). Specifically, we wish to derive a quantity $\eta^Q$, which is computable using only the approximate solution $\boldsymbol{u}_h$ and the data in (2.12). Ideally $\eta^Q$ should approximate the exact error, which is defined as

$$E \equiv Q_h(\boldsymbol{u}) - Q_h(\boldsymbol{u}_h) = \langle R(\boldsymbol{u}) - R(\boldsymbol{u}_h), \psi_h \rangle \,.$$

The efficiency and reliability of such an estimator is measured by the *global effectivity index*, or simply the *effectivity*, which we define as

$$\theta \equiv \frac{\eta^Q}{E}. \tag{2.16}$$

We say that $\eta^Q$ is *reliable* (*efficient*) if there exists a mesh-independent constant $C > 0$, such that $\theta \geq C$ ($\theta \leq C$).

In order to define the error estimator, we introduce a linearized adjoint problem, of the form suggested by Wildey et al. [67]. First we define the adjoint Dirichlet data on the Dirichlet part of the boundary $\Gamma_D$ by

$$\boldsymbol{z}_D = \begin{cases} \boldsymbol{e}_i, & s \in \Gamma_0, \\ \boldsymbol{0}, & s \in \Gamma_D / \Gamma_0. \end{cases} \tag{2.17}$$

Here we note that $\boldsymbol{z}_D$ agrees with $\psi_h$ on $\Gamma_D$. Next we define the linearized residual operator $DR(\boldsymbol{u})$ as the Gateaux derivative of the residual operator $R$ defined by

$$\langle DR(\boldsymbol{u})\boldsymbol{w}, \boldsymbol{v} \rangle \equiv \lim_{\epsilon \to 0^+} \epsilon^{-1} \, \langle R(\boldsymbol{u} + \epsilon \, \boldsymbol{w}) - R(\boldsymbol{u}), \boldsymbol{v} \rangle \,, \quad \boldsymbol{u}, \boldsymbol{v}, \boldsymbol{w} \in \mathcal{V}. \tag{2.18}$$

Now we are ready to define the adjoint problem: find $\boldsymbol{z} \in \boldsymbol{z}_D + V$:

$$\langle DR(\boldsymbol{u}_h)\boldsymbol{v}, \boldsymbol{z} \rangle = 0, \quad \boldsymbol{v} \in V. \tag{2.19}$$

Note that since the order of $\boldsymbol{z}$ and $\boldsymbol{v}$ is reversed from the usual order, $z$ is formally the solution of the linear adjoint problem, written abstractly as

$$DR(\boldsymbol{u}_h)^* \, \boldsymbol{z} = \boldsymbol{0},$$

where $\langle DR(\boldsymbol{u}_h)^* \boldsymbol{z}, \boldsymbol{v} \rangle \equiv \langle DR(\boldsymbol{u}_h)\boldsymbol{v}, \boldsymbol{z} \rangle$. Let $\boldsymbol{z}_h$ be the finite element approximation to $\boldsymbol{z}$, defined by: find $\boldsymbol{z}_h \in \boldsymbol{z}_D + V_h$:

$$\langle DR(\boldsymbol{u}_h)\boldsymbol{v}_h, \boldsymbol{z}_h \rangle = 0, \quad \boldsymbol{v}_h \in V_h. \tag{2.20}$$

When a Newton iteration is being used to solve (2.13) for $\boldsymbol{u}_h$, the transpose of the Jacobian matrix evaluated at $\boldsymbol{u}_h$ is exactly the matrix corresponding to the linear system in (2.20). This allows re-use of the underlying matrix assembly that was used to compute $\boldsymbol{u}_h$.

Because $\boldsymbol{z} - \psi_h \in V$ and $\boldsymbol{z}_h - \psi_h \in V_h$, we can use (2.11) and (2.13) to obtain

$$\langle R(\boldsymbol{u}), \boldsymbol{z} - \psi_h \rangle = 0. \tag{2.21}$$

and

$$\langle R(\boldsymbol{u}_h), \boldsymbol{z}_h - \psi_h \rangle = 0. \tag{2.22}$$

Assuming that $R$ is sufficiently smooth, we can use (2.19), (2.21), and (2.22) to estimate the error in $E$ as

$$\begin{aligned} E &= Q_h(\boldsymbol{u}) - Q_h(\boldsymbol{u}_h) \\ &= \langle R(\boldsymbol{u}), \psi_h \rangle - \langle R(\boldsymbol{u}_h), \psi_h \rangle \\ &= \langle R(\boldsymbol{u}), \boldsymbol{z} \rangle - \langle R(\boldsymbol{u}_h), \boldsymbol{z}_h \rangle \\ &= \langle R(\boldsymbol{u}_h) + DR(\boldsymbol{u}_h)\,(\boldsymbol{u} - \boldsymbol{u}_h), \boldsymbol{z} \rangle - \langle R(\boldsymbol{u}_h), \boldsymbol{z}_h \rangle + \text{h.o.t.} \\ &= \langle R(\boldsymbol{u}_h), \boldsymbol{z} - \boldsymbol{z}_h \rangle + \text{h.o.t.}. \end{aligned} \tag{2.23}$$

Now we use (2.12) to return to the specific form of the residual $R$. Expanding (2.23) we get the terms

$$E = \int_\Omega \boldsymbol{T}(\boldsymbol{u}_h) : \boldsymbol{\nabla}(\boldsymbol{z} - \boldsymbol{z}_h)\ \mathrm{d}\Omega - \int_\Omega \boldsymbol{f} \cdot (\boldsymbol{z} - \boldsymbol{z}_h)\ \mathrm{d}\Omega - \int_{\Gamma_N} \mathbf{g}_N \cdot (\boldsymbol{z} - \boldsymbol{z}_h)\ \mathrm{d}\Gamma + \text{h.o.t.}. \tag{2.24}$$

At this point we have an error estimator that is accurate up to higher order terms. However, it still contains the exact solution $\boldsymbol{z}$ to the adjoint problem in (2.19). Because we are solving $\boldsymbol{z}_h$ in the same approximation space as $\boldsymbol{u}_h$, we choose to approximate $\boldsymbol{z}$ and $\boldsymbol{\nabla z}$ using a recovery technique. Since the data $\boldsymbol{f}$ and $\mathbf{g}_N$ are zero in our MEMS problem, we will only need a gradient recovery operator for $\boldsymbol{\nabla z}$.

### 2.2.3 Gradient Recovery Operator

The gradient recovery operator $\boldsymbol{G}$ defines a $C^0$ representation of the displacement gradient. Because in a displacement formulation the finite element displacement field solution is $C^0$-represented as piecewise linear or quadratic using Lagrange polynomial elements, the resulting gradients have jumps between elements. In practice, and in

many finite element codes, the gradients, strains, or stresses are frequently postprocessed to recover a smoothed $C^0$ field. This recovery is typically computed by various recipes involving nodal averaging, projections, or weighted projections.

In Aria, the recovered gradient is computed in a two step process. First, nodal values for the gradient are computed for each node in the mesh by evaluating a local linear least squares fit of the gradient of the finite element solution. The sampling points of the least squares projection for a given node are the quadrature points in elements that depend on the node. Second, a $C^0$ representation of the gradients is formed by using these nodal values as coefficients of the same Lagrange polynomial nodal basis functions used for the displacement approximation. Below, we examine the first step in more detail.

Our initial interest lies in finding a value of the displacement gradient at node $k$ with coordinates $(x_k, y_k)$ in a mesh of linear quadrilateral elements. Let

$$\partial_j^* u_i(x, y) = a_1 + a_2 x + a_3 y + a_4 xy \tag{2.25}$$

be a bilinear representation of the $j$th partial derivative of the $i$th component of the displacement in the neighborhood of node $k$. Here, $\{a_l \,|\, l = 1, \ldots, 4\}$ are coefficients to be determined by a least squares fit, and $\partial_j^* u_i(x_k, y_k)$ will be the desired nodal value of the gradient. Thus, the least squares problem is

$$\begin{aligned} \text{minimize} \quad & \sum_{q=1}^{N} \left[\partial_j u_{hi}(x_q, y_q) - \partial_j^* u_i(x_q, y_q; \mathbf{a})\right]^2 \\ \mathbf{a} \in \mathbb{R}^4 \quad & \end{aligned} \tag{2.26}$$

where $\partial_j u_{hi}(x_q, y_q),\ q = 1, \ldots, N$ are values of the finite element solution gradient sampled at the quadrature points $(x_q, y_q)$ of the elements that depend on node $k$. Figure 2.1 depicts a set of the quadrature points contained in a typical patch of elements defined by a node.

The recovered gradient $\boldsymbol{G}(\boldsymbol{\nabla} \boldsymbol{u}_h)$ is then defined componentwise as

$$G_{ji}(\boldsymbol{\nabla} \boldsymbol{u}_h) \equiv \sum_{k=1}^{\text{nodes}} \partial_j^* u_i(x_k, y_k) \phi_k \tag{2.27}$$

where $\phi_k$ are the scalar valued basis functions associated with the nodes of the Lagrange finite elements.

### 2.2.4 Surface Force Error Estimator

Now that we have an a posteriori error estimate and a gradient recovery operator, we are ready to combine them to define a computable error estimator for the surface

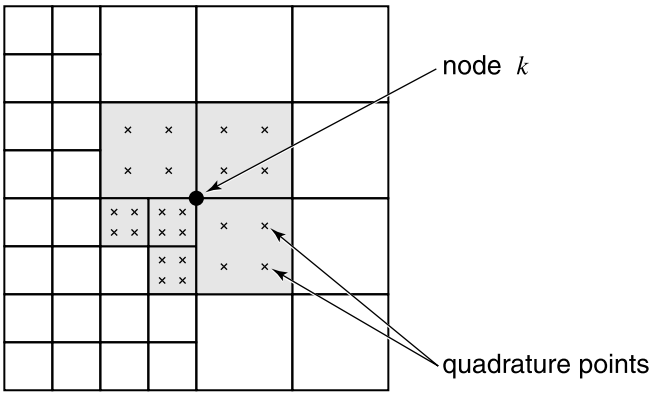


**Figure 2.1.** A typical nodal patch defining the input data for the recovery of a gradient value for a node $k$. The patch consists of the set of elements that depend on node $k$ (note that this set includes those elements with hanging nodes that in turn depend on the node $k$. The quadrature points of the elements are the sampling points for the least squares fit.

force. We assume henceforth that $\boldsymbol{f} = \mathbf{g}_N = \mathbf{0}$, so that (2.24) contains only the leading term containing the stress $\boldsymbol{T}(\boldsymbol{u}_h)$. Replacing the exact gradient of $\boldsymbol{z}$ in (2.24) by the gradient recovery operator applied to $\boldsymbol{\nabla z}_h$, we derive the error estimator for the surface force quantity of interest

$$\eta^Q \equiv \int_\Omega \boldsymbol{T}(\boldsymbol{u}_h) : (\boldsymbol{G}(\boldsymbol{\nabla z}_h) - \boldsymbol{\nabla z}_h) \, \mathrm{d}\Omega. \tag{2.28}$$

This error estimator for $E$ can be computed by calculating element contributions

$$\eta_K^Q \equiv \int_K \boldsymbol{T}(\boldsymbol{u}_h) : (\boldsymbol{G}(\boldsymbol{\nabla z}_h) - \boldsymbol{\nabla z}_h) \, \mathrm{d}K, \quad K \in \mathcal{T}_h, \tag{2.29}$$

and summing to obtain

$$\eta^Q = \sum_{K \in \mathcal{T}_h} \eta_K^Q.$$

We note that our work is related to the work of Wildey, et al. [67], who developed an error estimator for the surface flux for a scalar linear elliptic problem. However, while Wildey, et al., chose to solve the associated dual problem using higher order quadratic elements, we have used the same order linear elements combined with gradient recovery.

### 2.2.5 Global ZZ Estimator

The gradient recovery operator is also used to compute a global error indicator related to the Zienkiewicz and Zhu (ZZ) estimator [76]. Given the finite element solution,

this estimator provides a global error indicator

$$\eta^{ZZ} \equiv \left[ \int_\Omega |\boldsymbol{G}(\boldsymbol{\nabla} \boldsymbol{u}_h) - \boldsymbol{\nabla} \boldsymbol{u}_h|^2 \, \mathrm{d}\Omega \right]^{1/2}. \tag{2.30}$$

Again the error estimator $\eta^{ZZ}$ can be computed by calculating element contributions

$$\eta_K^{ZZ} \equiv \left[ \int_K |\boldsymbol{G}(\boldsymbol{\nabla} \boldsymbol{u}_h) - \boldsymbol{\nabla} \boldsymbol{u}_h| \, \mathrm{d}K \right]^{1/2}, \quad K \in \mathcal{T}_h, \tag{2.31}$$

and summing to obtain

$$\eta^{ZZ} = \left[ \sum_{K \in \mathcal{T}_h} \left( \eta_K^{ZZ} \right)^2 \right]^{1/2}.$$

### 2.2.6 Adaptive Mesh Refinement Strategy

Computing either $\eta = \eta^Q$ or $\eta = \eta^{ZZ}$ results in a local quantity $\eta_K$ defined on each element $K$ of the mesh, defined by (2.29) or (2.31). These can be understood as local contributions to the total error, although they may not represent the actual local error in the solution or the quantity of interest. The goal of adaptive mesh refinement (AMR) is to use these local error indicators to drive the local mesh refinement process. In this work, we will only focus on $h$-adaptivity, which consists of element refinement (subdivision of an element into multiple elements) and coarsening (aggregation of several elements into one).

In order to decide which elements to refine/coarsen, the element indicators $\{\eta_K\}$ are used in a marking strategy that assigns to each element a flag denoting refine, coarsen, or do nothing. Since the element indicators can be negative for the case of a quantity of interest error estimator, the absolute values of the local indicators are used in the marking algorithms discussed below. Once a preliminary marking has been performed, it is then revised in order that the new mesh satisfy certain consistency requirements, such as the 2-1 rule [3]. Then the mesh is modified and the finite element fields are prolongated into new fields on the new mesh.

One popular and inexpensive marking strategy is to mark elements based on the global maximum element error indicator. This method requires two parameters $\gamma_{refine}$ and $\gamma_{coarsen}$, which lie in the interval $[0, 1]$ and whose sum is less than one. Elements are marked for refinement if

$$|\eta_K| > \gamma_{refine} \max_K |\eta_K|,$$

and for coarsening if

$$|\eta_K| < \gamma_{coarsen} \max_K |\eta_K|.$$

Another marking strategy is based on marking the elements with the largest contributions to a fixed fraction of the global error. First the indicators are sorted in

decreasing order

$$|\eta_{K_1}| \geq |\eta_{K_1}| \geq \cdots \geq |\eta_{K_N}|.$$

Then an element $K_i$ is marked for refinement if

$$\sum_{j=1}^{i} |\eta_{K_j}| < (1 - \gamma_{refine}) \sum_{j=1}^{N} |\eta_{K_j}|,$$

and marked for coarsening if

$$\sum_{j=i}^{N} |\eta_{K_j}| < \gamma_{coarsen} \sum_{j=1}^{N} |\eta_{K_j}|.$$

This second strategy is designed to attempt to insure that a given fraction of the error is reduced between the current mesh and the mesh resulting from the mesh adaptivity. Such an approach can be more robust in practice than marking using the maximum element error indicator strategy.

Finally, we need a stopping criterion for terminating the adaptive refinement. We use a simple global tolerance criterion which is relative for $\eta^{ZZ}$

$$|\eta^{ZZ}| \leq GTOL \left( \int_K |\boldsymbol{\nabla} u_h|^2 \, dx \right)^{1/2},$$

and absolute for $\eta^Q$

$$|\eta^Q| \leq QTOL.$$

### 2.2.7 Error Correction of the Surface Force

We conclude this section with some brief remarks on the possibility of using the error estimator $\eta^Q$ to correct the quantity of interest. If the error estimator is reasonably accurate, then we expect to have the approximation

$$\eta^Q \approx E = Q_h(\boldsymbol{u}) - Q_h(\boldsymbol{u}_h).$$

It follows that it is reasonable to correct the quantity by adding the error estimator to the computed quantity

$$Q_h(\boldsymbol{u}) \approx Q_h^{corr}(\boldsymbol{u}_h) \equiv Q_h(\boldsymbol{u}_h) + \eta^Q.$$

While we anticipate that $Q_h^{corr}(\boldsymbol{u}_h)$ will be more accurate than $Q_h(\boldsymbol{u}_h)$, it is difficult to prove a priori that the corrected force is more accurate. This problem is equivalent to estimating the error in the error estimator

$$Q_h(\boldsymbol{u}) - Q_h^{corr}(\boldsymbol{u}_h) = E - \eta^Q.$$

In the next section we will provide some numerical evidence to suggest that the corrected quantity is generally more accurate and may converge at a faster rate than the quantity itself.

## 2.3 Reliability Analysis

Reliability methods are probabilistic algorithms for quantifying the effect of uncertainties in simulation input on response metrics of interest. In particular, they perform uncertainty quantification (UQ) by computing approximate response function distribution statistics based on specified probability distributions for input random variables. These response statistics include response mean, response standard deviation, and cumulative or complementary cumulative distribution function (CDF/CCDF) pairings of response levels and either probability or reliability levels. These methods are often more efficient at computing statistics in the tails of the response distributions (events with low probability) than sampling-based approaches since the number of samples required to resolve a low probability can be prohibitive. Thus, these methods, as their name implies, are often used in a reliability context for assessing the probability of failure of a system when confronted with an uncertain environment.

A number of classical reliability analysis methods are discussed in [38], including Mean-Value First-Order Second-Moment (MVFOSM), First-Order Reliability Method (FORM), and Second-Order Reliability Method (SORM). More recent methods which seek to improve the efficiency of FORM analysis through limit state approximations include the use of local and multipoint approximations in Advanced Mean Value methods (AMV/AMV+ [72]) and Two-point Adaptive Nonlinearity Approximation-based methods (TANA [66, 75]), respectively. Each of the FORM-based methods can be employed for "forward" or "inverse" reliability analysis through the reliability index approach (RIA) or performance measure approach (PMA), respectively, as described in [64].

In order to provide access to a variety of uncertainty quantification capabilities for analysis of large-scale engineering applications on high-performance parallel computers, the DAKOTA project [30] at Sandia National Laboratories has developed a suite of algorithmic capabilities known as DAKOTA/UQ [70]. This package contains the reliability analysis capabilities described in this report and enables the RBDO approaches, and is freely available for download worldwide through an open source license.

This section overviews a variety of approaches for performing reliability analysis. In particular, forward and inverse reliability analyses are presented using multiple limit state approximation, probability integration, warm starting, Hessian approximation, and optimization algorithm selections. These uncertainty quantification capabilities have also provided a foundation for exploring bi-level and sequential RBDO formulations, as described in Sections 2.4.

### 2.3.1 Mean Value

The Mean Value method (MV, also known as MVFOSM in [38]) is the simplest, least-expensive reliability method because it estimates the response means, response standard deviations, and all CDF/CCDF response-probability-reliability levels from a single evaluation of response functions and their gradients at the uncertain variable means. This approximation can have acceptable accuracy when the response functions are nearly linear and their distributions are approximately Gaussian, but can have poor accuracy in other situations. The expressions for approximate response mean $\mu_g$, approximate response standard deviation $\sigma_g$, response target to approximate probability/reliability level mapping ($\bar{z} \rightarrow p, \beta$), and probability/reliability target to approximate response level mapping ($\bar{p}, \bar{\beta} \rightarrow z$) are

$$\mu_g = g(\mu_{\mathbf{x}}) \tag{2.32}$$

$$\sigma_g = \sum_i \sum_j Cov(i,j) \frac{dg}{dx_i}(\mu_{\mathbf{x}}) \frac{dg}{dx_j}(\mu_{\mathbf{x}}) \tag{2.33}$$

$$\beta_{cdf} = \frac{\mu_g - \bar{z}}{\sigma_g} \tag{2.34}$$

$$\beta_{ccdf} = \frac{\bar{z} - \mu_g}{\sigma_g} \tag{2.35}$$

$$z = \mu_g - \sigma_g \bar{\beta}_{cdf} \tag{2.36}$$

$$z = \mu_g + \sigma_g \bar{\beta}_{ccdf} \tag{2.37}$$

respectively, where $\mathbf{x}$ are the uncertain values in the space of the original uncertain variables ("x-space"), $g(\mathbf{x})$ is the limit state function (the response function for which probability-response level pairs are needed), and $\beta_{cdf}$ and $\beta_{ccdf}$ are the CDF and CCDF reliability indices, respectively.

With the introduction of second-order limit state information, MVSOSM calculates a second-order mean as

$$\mu_g = g(\mu_{\mathbf{x}}) + \frac{1}{2} \sum_i \sum_j Cov(i,j) \frac{d^2 g}{dx_i dx_j}(\mu_{\mathbf{x}}) \tag{2.38}$$

This is commonly combined with a first-order variance (2.33), since second-order variance involves higher order distribution moments (skewness, kurtosis) [38] which are often unavailable.

The first-order CDF probability $p(g \leq z)$, first-order CCDF probability $p(g > z)$,

$\beta_{cdf}$, and $\beta_{ccdf}$ are related to one another through

$$
\begin{aligned}
p(g \leq z) &= \Phi(-\beta_{cdf}) && (2.39)\\
p(g > z) &= \Phi(-\beta_{ccdf}) && (2.40)\\
\beta_{cdf} &= -\Phi^{-1}(p(g \leq z)) && (2.41)\\
\beta_{ccdf} &= -\Phi^{-1}(p(g > z)) && (2.42)\\
\beta_{cdf} &= -\beta_{ccdf} && (2.43)\\
p(g \leq z) &= 1 - p(g > z) && (2.44)
\end{aligned}
$$

where $\Phi()$ is the standard normal cumulative distribution function. A common convention in the literature is to define $g$ in such a way that the CDF probability for a response level $z$ of zero (i.e., $p(g \leq 0)$) is the response metric of interest. The formulations in this report are not restricted to this convention and are designed to support CDF or CCDF mappings for general response, probability, and reliability level sequences.

### 2.3.2 MPP Search Methods

All other reliability methods solve a nonlinear optimization problem to compute a most probable point (MPP) and then integrate about this point to compute probabilities. The MPP search is performed in uncorrelated standard normal space ("u-space") since it simplifies the probability integration: the distance of the MPP from the origin has the meaning of the number of input standard deviations separating the mean response from a particular response threshold. The transformation from correlated non-normal distributions (x-space) to uncorrelated standard normal distributions (u-space) is denoted as $\mathbf{u} = T(\mathbf{x})$ with the reverse transformation denoted as $\mathbf{x} = T^{-1}(\mathbf{u})$. These transformations are nonlinear in general, and possible approaches include the Rosenblatt [58], Nataf [23], and Box-Cox [15] transformations. The nonlinear transformations may also be linearized, and common approaches for this include the Rackwitz-Fiessler [55] two-parameter equivalent normal and the Chen-Lind [20] and Wu-Wirsching [74] three-parameter equivalent normals. The results in this report employ the Nataf nonlinear transformation which occurs in the following two steps. To transform between the original correlated x-space variables and correlated standard normals ("z-space"), the CDF matching condition is used:

$$\Phi(z_i) = F(x_i) \tag{2.45}$$

where $F()$ is the cumulative distribution function of the original probability distribution. Then, to transform between correlated z-space variables and uncorrelated u-space variables, the Cholesky factor $\mathbf{L}$ of a modified correlation matrix is used:

$$\mathbf{z} = \mathbf{L}\mathbf{u} \tag{2.46}$$

where the original correlation matrix for non-normals in x-space has been modified to represent the corresponding correlation in z-space [23].

The forward reliability analysis algorithm of computing CDF/CCDF probability/reliability levels for specified response levels is called the reliability index approach (RIA), and the inverse reliability analysis algorithm of computing response levels for specified CDF/CCDF probability/reliability levels is called the performance measure approach (PMA) [64]. The differences between the RIA and PMA formulations appear in the objective function and equality constraint formulations used in the MPP searches. For RIA, the MPP search for achieving the specified response level $\bar{z}$ is formulated as

$$\begin{aligned} \text{minimize} \quad & \mathbf{u}^T\mathbf{u} \\ \text{subject to} \quad & G(\mathbf{u}) = \bar{z} \end{aligned} \tag{2.47}$$

and for PMA, the MPP search for achieving the specified reliability/probability level $\bar{\beta}, \bar{p}$ is formulated as

$$\begin{aligned} \text{minimize} \quad & \pm G(\mathbf{u}) \\ \text{subject to} \quad & \mathbf{u}^T\mathbf{u} = \bar{\beta}^2 \end{aligned} \tag{2.48}$$

where $\mathbf{u}$ is a vector centered at the origin in u-space and $g(\mathbf{x}) \equiv G(\mathbf{u})$ by definition. In the RIA case, the optimal MPP solution $\mathbf{u}^*$ defines the reliability index from $\beta = \pm\|\mathbf{u}^*\|_2$, which in turn defines the CDF/CCDF probabilities using (2.39)–(2.40) in the case of first-order integration. The sign of $\beta$ is defined by

$$G(\mathbf{u}^*) > G(\mathbf{0}) : \beta_{cdf} < 0, \beta_{ccdf} > 0 \tag{2.49}$$
$$G(\mathbf{u}^*) < G(\mathbf{0}) : \beta_{cdf} > 0, \beta_{ccdf} < 0 \tag{2.50}$$

where $G(\mathbf{0})$ is the median limit state response computed at the origin in u-space (where $\beta_{cdf} = \beta_{ccdf} = 0$ and first-order $p(g \leq z) = p(g > z) = 0.5$). In the PMA case, the sign applied to $G(\mathbf{u})$ (equivalent to minimizing or maximizing $G(\mathbf{u})$) is similarly defined by $\bar{\beta}$

$$\bar{\beta}_{cdf} < 0, \bar{\beta}_{ccdf} > 0 : \text{maximize } G(\mathbf{u}) \tag{2.51}$$
$$\bar{\beta}_{cdf} > 0, \bar{\beta}_{ccdf} < 0 : \text{minimize } G(\mathbf{u}) \tag{2.52}$$

and the limit state at the MPP ($G(\mathbf{u}^*)$) defines the desired response level result.

When performing PMA with specified $\bar{p}$, one must compute $\bar{\beta}$ to include in (2.48). While this is a straightforward one-time calculation for first-order integrations (2.41)–(2.42), the use of second-order integrations complicates matters since the $\bar{\beta}$ corresponding to the prescribed $\bar{p}$ is a function of the Hessian of $G$, see (2.69), which in turn

is a function of location in u-space. A generalized reliability index (2.81), which would allow a one-time calculation, may not be used since equality with $\mathbf{u}^T\mathbf{u}$ is not meaningful. The $\bar{\beta}$ target must therefore be updated in (2.48) as the minimization progresses (e.g., using Newton's method to solve (2.69) for $\bar{\beta}$ given $\bar{p}$ and $\kappa_i$). This works best when $\bar{\beta}$ can be fixed during the course of an approximate optimization, such as for the AMV$^2$+ and TANA methods described in Section 2.3.2.1. For second-order PMA without limit state approximation cycles (i.e., PMA SORM), the constraint must be continually updated and the constraint derivative should include $\nabla_{\mathbf{u}}\bar{\beta}$, which would require third-order information for the limit state to compute derivatives of the principal curvatures. This is impractical, so the PMA SORM constraint derivatives are only approximated analytically or estimated numerically. Potentially for this reason, PMA SORM has not been widely explored in the literature.

#### 2.3.2.1 Limit state approximations

There are a variety of algorithmic variations that can be explored within RIA/PMA reliability analysis. First, one may select among several different limit state approximations that can be used to reduce computational expense during the MPP searches. Local, multipoint, and global approximations of the limit state are possible. [26] investigated local first-order limit state approximations, and [27] investigated local second-order and multipoint approximations. These techniques include:

1. a single Taylor series per response/reliability/probability level in x-space centered at the uncertain variable means. The first-order approach is commonly known as the Advanced Mean Value (AMV) method:

$$g(\mathbf{x}) \cong g(\mu_{\mathbf{x}}) + \nabla_x g(\mu_{\mathbf{x}})^T(\mathbf{x} - \mu_{\mathbf{x}}) \tag{2.53}$$

   and the second-order approach has been named AMV$^2$:

$$g(\mathbf{x}) \cong g(\mu_{\mathbf{x}}) + \nabla_{\mathbf{x}} g(\mu_{\mathbf{x}})^T(\mathbf{x} - \mu_{\mathbf{x}}) + \frac{1}{2}(\mathbf{x} - \mu_{\mathbf{x}})^T\nabla^2_{\mathbf{x}} g(\mu_{\mathbf{x}})(\mathbf{x} - \mu_{\mathbf{x}}) \tag{2.54}$$

2. same as AMV/AMV$^2$, except that the Taylor series is expanded in u-space. The first-order option has been termed the u-space AMV method:

$$G(\mathbf{u}) \cong G(\mu_{\mathbf{u}}) + \nabla_u G(\mu_{\mathbf{u}})^T(\mathbf{u} - \mu_{\mathbf{u}}) \tag{2.55}$$

   where $\mu_{\mathbf{u}} = T(\mu_{\mathbf{x}})$ and is nonzero in general, and the second-order option has been named the u-space AMV$^2$ method:

$$G(\mathbf{u}) \cong G(\mu_{\mathbf{u}}) + \nabla_{\mathbf{u}} G(\mu_{\mathbf{u}})^T(\mathbf{u} - \mu_{\mathbf{u}}) + \frac{1}{2}(\mathbf{u} - \mu_{\mathbf{u}})^T\nabla^2_{\mathbf{u}} G(\mu_{\mathbf{u}})(\mathbf{u} - \mu_{\mathbf{u}}) \tag{2.56}$$

3. an initial Taylor series approximation in x-space at the uncertain variable means, with iterative expansion updates at each MPP estimate ($\mathbf{x}^*$) until the MPP converges. The first-order option is commonly known as AMV+:

$$g(\mathbf{x}) \cong g(\mathbf{x}^*) + \nabla_x g(\mathbf{x}^*)^T(\mathbf{x} - \mathbf{x}^*) \tag{2.57}$$

and the second-order option has been named AMV$^2$+:

$$g(\mathbf{x}) \cong g(\mathbf{x}^*) + \nabla_{\mathbf{x}} g(\mathbf{x}^*)^T(\mathbf{x} - \mathbf{x}^*) + \frac{1}{2}(\mathbf{x} - \mathbf{x}^*)^T \nabla^2_{\mathbf{x}} g(\mathbf{x}^*)(\mathbf{x} - \mathbf{x}^*) \tag{2.58}$$

4. same as AMV+/AMV$^2$+, except that the expansions are performed in u-space. The first-order option has been termed the u-space AMV+ method.

$$G(\mathbf{u}) \cong G(\mathbf{u}^*) + \nabla_u G(\mathbf{u}^*)^T(\mathbf{u} - \mathbf{u}^*) \tag{2.59}$$

and the second-order option has been named the u-space AMV$^2$+ method:

$$G(\mathbf{u}) \cong G(\mathbf{u}^*) + \nabla_{\mathbf{u}} G(\mathbf{u}^*)^T(\mathbf{u} - \mathbf{u}^*) + \frac{1}{2}(\mathbf{u} - \mathbf{u}^*)^T \nabla^2_{\mathbf{u}} G(\mathbf{u}^*)(\mathbf{u} - \mathbf{u}^*) \tag{2.60}$$

5. a multipoint approximation in x-space. This approach involves a Taylor series approximation in intermediate variables where the powers used for the intermediate variables are selected to match information at the current and previous expansion points. Based on the two-point exponential approximation concept (TPEA, [36]), the two-point adaptive nonlinearity approximation (TANA-3, [75]) approximates the limit state as:

$$g(\mathbf{x}) \cong g(\mathbf{x}_2) + \sum_{i=1}^{n} \frac{\partial g}{\partial x_i}(\mathbf{x}_2) \frac{x_{i,2}^{1-p_i}}{p_i}(x_i^{p_i} - x_{i,2}^{p_i}) + \frac{1}{2}\epsilon(\mathbf{x}) \sum_{i=1}^{n}(x_i^{p_i} - x_{i,2}^{p_i})^2 \tag{2.61}$$

where $n$ is the number of uncertain variables and:

$$p_i = 1 + \ln\left[\frac{\frac{\partial g}{\partial x_i}(\mathbf{x}_1)}{\frac{\partial g}{\partial x_i}(\mathbf{x}_2)}\right] \Big/ \ln\left[\frac{x_{i,1}}{x_{i,2}}\right] \tag{2.62}$$

$$\epsilon(\mathbf{x}) = \frac{H}{\sum_{i=1}^{n}(x_i^{p_i} - x_{i,1}^{p_i})^2 + \sum_{i=1}^{n}(x_i^{p_i} - x_{i,2}^{p_i})^2} \tag{2.63}$$

$$H = 2\left[g(\mathbf{x}_1) - g(\mathbf{x}_2) - \sum_{i=1}^{n} \frac{\partial g}{\partial x_i}(\mathbf{x}_2) \frac{x_{i,2}^{1-p_i}}{p_i}(x_{i,1}^{p_i} - x_{i,2}^{p_i})\right] \tag{2.64}$$

and $\mathbf{x}_2$ and $\mathbf{x}_1$ are the current and previous MPP estimates in x-space, respectively. Prior to the availability of two MPP estimates, x-space AMV+ is used.

6. a multipoint approximation in u-space. The u-space TANA-3 approximates the limit state as:

$$G(\mathbf{u}) \cong G(\mathbf{u}_2) + \sum_{i=1}^{n} \frac{\partial G}{\partial u_i}(\mathbf{u}_2) \frac{u_{i,2}^{1-p_i}}{p_i}(u_i^{p_i} - u_{i,2}^{p_i}) + \frac{1}{2}\epsilon(\mathbf{u}) \sum_{i=1}^{n}(u_i^{p_i} - u_{i,2}^{p_i})^2 \quad (2.65)$$

where:

$$p_i = 1 + \ln\left[\frac{\frac{\partial G}{\partial u_i}(\mathbf{u}_1)}{\frac{\partial G}{\partial u_i}(\mathbf{u}_2)}\right] \Big/ \ln\left[\frac{u_{i,1}}{u_{i,2}}\right] \quad (2.66)$$

$$\epsilon(\mathbf{u}) = \frac{H}{\sum_{i=1}^{n}(u_i^{p_i} - u_{i,1}^{p_i})^2 + \sum_{i=1}^{n}(u_i^{p_i} - u_{i,2}^{p_i})^2} \quad (2.67)$$

$$H = 2\left[G(\mathbf{u}_1) - G(\mathbf{u}_2) - \sum_{i=1}^{n} \frac{\partial G}{\partial u_i}(\mathbf{u}_2) \frac{u_{i,2}^{1-p_i}}{p_i}(u_{i,1}^{p_i} - u_{i,2}^{p_i})\right] \quad (2.68)$$

and $\mathbf{u}_2$ and $\mathbf{u}_1$ are the current and previous MPP estimates in u-space, respectively. Prior to the availability of two MPP estimates, u-space AMV+ is used.

7. the MPP search on the original response functions without the use of any approximations.

The Hessian matrices in AMV$^2$ and AMV$^2$+ may be available analytically, estimated numerically, or approximated through quasi-Newton updates. The quasi-Newton variant of AMV$^2$+ is conceptually similar to TANA in that both approximate curvature based on a sequence of gradient evaluations. TANA estimates curvature by matching values and gradients at two points and includes it through the use of exponential intermediate variables and a single-valued diagonal Hessian approximation. Quasi-Newton AMV$^2$+ accumulates curvature over a sequence of points and then uses it directly in a second-order series expansion. Therefore, these methods may be expected to exhibit similar performance.

The selection between x-space or u-space for performing approximations depends on where the approximation will be more accurate, since this will result in more accurate MPP estimates (AMV, AMV$^2$) or faster convergence (AMV+, AMV$^2$+, TANA). Since this relative accuracy depends on the forms of the limit state $g(x)$ and the transformation $T(x)$ and is therefore application dependent in general, DAKOTA/UQ supports both options. A concern with approximation-based iterative search methods (i.e., AMV+, AMV$^2$+ and TANA) is the robustness of their convergence to the MPP. It is possible for the MPP iterates to oscillate or even diverge. However, to date, this occurrence has been relatively rare, and DAKOTA/UQ contains checks that monitor for this behavior. Another concern with TANA is numerical safeguarding. First, there is the possibility of raising negative $x_i$ or $u_i$ values to nonintegral $p_i$ exponents in (2.61), (2.63)–(2.65), and (2.67)–(2.68). This is particularly likely for u-space.

Safeguarding techniques include the use of linear bounds scaling for each $x_i$ or $u_i$, offsetting negative $x_i$ or $u_i$, or promotion of $p_i$ to integral values for negative $x_i$ or $u_i$. In numerical experimentation, the offset approach has been the most effective in retaining the desired data matches without overly inflating the $p_i$ exponents. Second, there are a number of potential numerical difficulties with the logarithm ratios in (2.62) and (2.66). In this case, a safeguarding strategy is to revert to either the linear ($p_i = 1$) or reciprocal ($p_i = -1$) approximation based on which approximation has lower error in $\frac{\partial g}{\partial x_i}(\mathbf{x}_1)$ or $\frac{\partial G}{\partial u_i}(\mathbf{u}_1)$.

#### 2.3.2.2 Probability integrations

The second algorithmic variation involves the integration approach for computing probabilities at the MPP, which can be selected to be first-order (2.39)–(2.40) or second-order integration. Second-order integration involves applying a curvature correction [16, 40, 41]. Breitung applies a correction based on asymptotic analysis [16]:

$$p = \Phi(-\beta_p) \prod_{i=1}^{n-1} \frac{1}{\sqrt{1 + \beta_p \kappa_i}} \tag{2.69}$$

where $\kappa_i$ are the principal curvatures of the limit state function (the eigenvalues of an orthonormal transformation of $\nabla^2_{\mathbf{u}} G$, taken positive for a convex limit state) and $\beta_p \geq 0$ (select CDF or CCDF probability correction to obtain correct sign for $\beta_p$). An alternate correction in [40] is consistent in the asymptotic regime ($\beta_p \to \infty$) but does not collapse to first-order integration for $\beta_p = 0$:

$$p = \Phi(-\beta_p) \prod_{i=1}^{n-1} \frac{1}{\sqrt{1 + \psi(-\beta_p)\kappa_i}} \tag{2.70}$$

where $\psi() = \frac{\phi()}{\Phi()}$ and $\phi()$ is the standard normal density function. [41] applies further corrections to (2.70) based on point concentration methods.

To invert a second-order integration and compute $\beta_p$ given $p$ and $\kappa_i$ (e.g., for second-order PMA as described in Section 2.3.2), Newton's method can be applied as described in [27]. Combining the no-approximation option of the MPP search with first-order and second-order integration approaches results in the traditional first-order and second-order reliability methods (FORM and SORM). Additional probability integration approaches can involve importance sampling in the vicinity of the MPP [40, 71], but are outside the scope of this report. While second-order integrations could be performed anywhere a limit state Hessian has been computed, the additional computational effort is most warranted for fully converged MPPs from AMV+, AMV$^2$+, TANA, FORM, and SORM, and is of reduced value for MVFOSM, MVSOSM, AMV, or AMV$^2$.

#### 2.3.2.3 Hessian approximations

To use a second-order Taylor series or a second-order integration when second-order information ($\nabla^2_{\mathbf{x}} g$, $\nabla^2_{\mathbf{u}} G$, and/or $\kappa$) is not directly available, one can estimate the missing information using finite differences or approximate it through use of quasi-Newton approximations. These procedures will often be needed to make second-order approaches practical for engineering applications.

In the finite difference case, numerical Hessians are commonly computed using either first-order forward differences of gradients using

$$\nabla^2 g(\mathbf{x}) \cong \frac{\nabla g(\mathbf{x} + h\mathbf{e}_i) - \nabla g(\mathbf{x})}{h} \tag{2.71}$$

to estimate the $i^{th}$ Hessian column when gradients are analytically available, or second-order differences of function values using

$$\nabla^2 g(\mathbf{x}) \cong \frac{g(\mathbf{x}+h\mathbf{e}_i+h\mathbf{e}_j) - g(\mathbf{x}+h\mathbf{e}_i-h\mathbf{e}_j) - g(\mathbf{x}-h\mathbf{e}_i+h\mathbf{e}_j) + g(\mathbf{x}-h\mathbf{e}_i-h\mathbf{e}_j)}{4h^2} \tag{2.72}$$

to estimate the $ij^{th}$ Hessian term when gradients are not directly available. This approach has the advantage of locally-accurate Hessians for each point of interest (which can lead to quadratic convergence rates in discrete Newton methods), but has the disadvantage that numerically estimating each of the matrix terms can be expensive.

Quasi-Newton approximations, on the other hand, do not reevaluate all of the second-order information for every point of interest. Rather, they accumulate approximate curvature information over time using secant updates. Since they utilize the existing gradient evaluations, they do not require any additional function evaluations for evaluating the Hessian terms. The quasi-Newton approximations of interest include the Broyden-Fletcher-Goldfarb-Shanno (BFGS) update

$$\mathbf{B}_{k+1} = \mathbf{B}_k - \frac{\mathbf{B}_k \mathbf{s}_k \mathbf{s}_k^T \mathbf{B}_k}{\mathbf{s}_k^T \mathbf{B}_k \mathbf{s}_k} + \frac{\mathbf{y}_k \mathbf{y}_k^T}{\mathbf{y}_k^T \mathbf{s}_k} \tag{2.73}$$

which yields a sequence of symmetric positive definite Hessian approximations, and the Symmetric Rank 1 (SR1) update

$$\mathbf{B}_{k+1} = \mathbf{B}_k + \frac{(\mathbf{y}_k - \mathbf{B}_k \mathbf{s}_k)(\mathbf{y}_k - \mathbf{B}_k \mathbf{s}_k)^T}{(\mathbf{y}_k - \mathbf{B}_k \mathbf{s}_k)^T \mathbf{s}_k} \tag{2.74}$$

which yields a sequence of symmetric, potentially indefinite, Hessian approximations. $\mathbf{B}_k$ is the $k^{th}$ approximation to the Hessian $\nabla^2 g$, $\mathbf{s}_k = \mathbf{x}_{k+1} - \mathbf{x}_k$ is the step and $\mathbf{y}_k = \nabla g_{k+1} - \nabla g_k$ is the corresponding yield in the gradients. The selection of BFGS versus SR1 involves the importance of retaining positive definiteness in the Hessian approximations; if the procedure does not require it, then the SR1 update can be more accurate if the true Hessian is not positive definite. Initial scalings for $\mathbf{B}_0$ and numerical safeguarding techniques (damped BFGS, update skipping) are described in [27].

#### 2.3.2.4 Optimization algorithms

The next algorithmic variation involves the optimization algorithm selection for solving (2.47) and (2.48). The Hasofer-Lind Rackwitz-Fissler (HL-RF) algorithm [38] is a classical approach that has been broadly applied. It is a Newton-based approach lacking line search/trust region globalization, and is generally regarded as computationally efficient but occasionally unreliable. DAKOTA/UQ takes the approach of employing robust, general-purpose optimization algorithms with provable convergence properties. This report employs the sequential quadratic programming (SQP) and nonlinear interior-point (NIP) optimization algorithms from the NPSOL [37] and OPT++ [50] libraries, respectively.

#### 2.3.2.5 Warm starting of MPP searches

The final algorithmic variation involves the use of warm starting approaches for improving computational efficiency [26] describes the acceleration of MPP searches through warm starting with approximate iteration increment, with $z/p/\beta$ level increment, and with design variable increment. Warm started data includes the expansion point and associated response values and the MPP optimizer initial guess. Projections are used when an increment in $z/p/\beta$ level or design variables occurs. Warm starts were consistently effective in [26], with greater effectiveness for smaller parameter changes, and are used for all computational experiments presented in this report.

## 2.4 Reliability-Based Design Optimization

The capability to assess reliability is broadly useful within a design optimization context, and reliability-based design optimization (RBDO) methods are popular approaches for designing systems while accounting for reliability metrics. RBDO approaches may be broadly characterized as bi-level (in which the reliability analysis is nested within the optimization, e.g. [5]), sequential (in which iteration occurs between optimization and reliability analysis, e.g. [73, 24]), or unilevel (in which the design and reliability searches are combined into a single optimization, e.g. [2]). Bi-level RBDO methods are simple and general-purpose, but can be computationally demanding. Sequential and unilevel methods seek to reduce computational expense by breaking the nested relationship through the use of iterated or simultaneous approaches.

The reliability analysis capabilities described in Section 2.3 provide a rich foundation for exploring a variety of RBDO formulations. [26] investigated bi-level, fully-analytic bi-level, and first-order sequential RBDO approaches employing underlying first-order reliability assessments. [27] investigated fully-analytic bi-level and second-order sequential RBDO approaches employing underlying second-order reliability assessments. These methods are overviewed in the following sections.

### 2.4.1 Bi-level RBDO

The simplest and most direct RBDO approach is the bi-level approach in which a full reliability analysis is performed for every optimization function evaluation. This involves a nesting of two distinct levels of optimization within each other, one at the design level and one at the MPP search level.

Since an RBDO problem will typically specify both the $\bar{z}$ level and the $\bar{p}/\bar{\beta}$ level, one can use either the RIA or the PMA formulation for the UQ portion and then constrain the result in the design optimization portion. In particular, RIA reliability analysis maps $\bar{z}$ to $p/\beta$, so RIA RBDO constrains $p/\beta$:

$$\begin{aligned} \text{minimize} \quad & f \\ \text{subject to} \quad & \beta \geq \bar{\beta} \\ \text{or} \quad & p \leq \bar{p} \end{aligned} \tag{2.75}$$

And PMA reliability analysis maps $\bar{p}/\bar{\beta}$ to $z$, so PMA RBDO constrains $z$:

$$\begin{aligned} \text{minimize} \quad & f \\ \text{subject to} \quad & z \geq \bar{z} \end{aligned} \tag{2.76}$$

where $z \geq \bar{z}$ is used as the RBDO constraint for a cumulative failure probability (failure defined as $z \leq \bar{z}$) but $z \leq \bar{z}$ would be used as the RBDO constraint for a complementary cumulative failure probability (failure defined as $z \geq \bar{z}$). It is worth noting that DAKOTA is not limited to these types of inequality-constrained RBDO formulations; rather, they are convenient examples. DAKOTA supports general optimization under uncertainty mappings [31] which allow flexible use of statistics within multiple objectives, inequality constraints, and equality constraints.

An important performance enhancement for bi-level methods is the use of sensitivity analysis to analytically compute the design gradients of probability, reliability, and response levels. When design variables are separate from the uncertain variables (i.e., they are not distribution parameters), then the following first-order expressions may be used [39, 43, 5]:

$$\nabla_{\mathbf{d}} z = \nabla_{\mathbf{d}} g \tag{2.77}$$

$$\nabla_{\mathbf{d}} \beta_{cdf} = \frac{1}{\| \nabla_{\mathbf{u}} G \|} \nabla_{\mathbf{d}} g \tag{2.78}$$

$$\nabla_{\mathbf{d}} p_{cdf} = -\phi(-\beta_{cdf}) \nabla_{\mathbf{d}} \beta_{cdf} \tag{2.79}$$

where it is evident from (2.43)–(2.44) that $\nabla_{\mathbf{d}} \beta_{ccdf} = -\nabla_{\mathbf{d}} \beta_{cdf}$ and $\nabla_{\mathbf{d}} p_{ccdf} = -\nabla_{\mathbf{d}} p_{cdf}$.

In the case of second-order integrations, (2.79) must be expanded to include the curvature correction. For Breitung's correction (2.69),

$$\nabla_{\mathbf{d}} p_{cdf} = \left[ \Phi(-\beta_p) \sum_{i=1}^{n-1} \left( \frac{-\kappa_i}{2(1+\beta_p\kappa_i)^{\frac{3}{2}}} \prod_{\substack{j=1 \\ j\neq i}}^{n-1} \frac{1}{\sqrt{1+\beta_p\kappa_j}} \right) - \phi(-\beta_p) \prod_{i=1}^{n-1} \frac{1}{\sqrt{1+\beta_p\kappa_i}} \right] \nabla_{\mathbf{d}} \beta_{cdf} \tag{2.80}$$

where $\nabla_{\mathbf{d}}\kappa_i$ has been neglected and $\beta_p \geq 0$ (see Section 2.3.2.2). Other approaches assume the curvature correction is nearly independent of the design variables [54], which is equivalent to neglecting the first term in (2.80).

To capture second-order probability estimates within an RIA RBDO formulation using well-behaved $\beta$ constraints, a generalized reliability index can be introduced where, similar to (2.41),

$$\beta^*_{cdf} = -\Phi^{-1}(p_{cdf}) \tag{2.81}$$

for second-order $p_{cdf}$. This reliability index is no longer equivalent to the magnitude of $\mathbf{u}$, but rather is a convenience metric for capturing the effect of more accurate probability estimates. The corresponding generalized reliability index sensitivity, similar to (2.79), is

$$\nabla_{\mathbf{d}} \beta^*_{cdf} = -\frac{1}{\phi(-\beta^*_{cdf})} \nabla_{\mathbf{d}} p_{cdf} \tag{2.82}$$

where $\nabla_{\mathbf{d}} p_{cdf}$ is defined from (2.80). Even when $\nabla_{\mathbf{d}} g$ is estimated numerically, (2.77)–(2.82) can be used to avoid numerical differencing across full reliability analyses.

When the design variables are distribution parameters of the uncertain variables, $\nabla_{\mathbf{d}} g$ is expanded with the chain rule and (2.77) and (2.78) become

$$\nabla_{\mathbf{d}} z = \nabla_{\mathbf{d}} \mathbf{x} \nabla_{\mathbf{x}} g \tag{2.83}$$

$$\nabla_{\mathbf{d}} \beta_{cdf} = \frac{1}{\| \nabla_{\mathbf{u}} G \|} \nabla_{\mathbf{d}} \mathbf{x} \nabla_{\mathbf{x}} g \tag{2.84}$$

where the design Jacobian of the transformation ($\nabla_{\mathbf{d}} \mathbf{x}$) may be obtained analytically for uncorrelated $\mathbf{x}$ or semi-analytically for correlated $\mathbf{x}$ ($\nabla_{\mathbf{d}} \mathbf{L}$ is evaluated numerically) by differentiating (2.45) and (2.46) with respect to the distribution parameters. Meanwhile (2.79)–(2.82) remain the same as before. For this design variable case, all required information for the sensitivities is available from the MPP search.

Since (2.77)–(2.84) are derived using the Karush-Kuhn-Tucker optimality conditions for a converged MPP, they are appropriate for RBDO using AMV+, AMV$^2$+, TANA, FORM, and SORM, but not for RBDO using MVFOSM, MVSOSM, AMV, or AMV$^2$.

### 2.4.2 Sequential/Surrogate-based RBDO

An alternative RBDO approach is the sequential approach, in which additional efficiency is sought through breaking the nested relationship of the MPP and design searches. The general concept is to iterate between optimization and uncertainty quantification, updating the optimization goals based on the most recent probabilistic assessment results. This update may be based on safety factors [73] or other approximations [24].

A particularly effective approach for updating the optimization goals is to use the $p/\beta/z$ sensitivity analysis of (2.77)–(2.84) in combination with local surrogate models [77]. In [26] and [27], first-order and second-order Taylor series approximations were employed within a trust-region model management framework [28] in order to adaptively manage the extent of the approximations and ensure convergence of the RBDO process. Surrogate models were used for both the objective function and the constraints, although the use of constraint surrogates alone is sufficient to remove the nesting.

In particular, RIA trust-region surrogate-based RBDO employs surrogate models of $f$ and $p/\beta$ within a trust region $\Delta^k$ centered at $\mathbf{d}_c$. For first-order surrogates:

$$\begin{aligned} \text{minimize} \quad & f(\mathbf{d}_c) + \nabla_d f(\mathbf{d}_c)^T(\mathbf{d}-\mathbf{d}_c) \\ \text{subject to} \quad & \beta(\mathbf{d}_c) + \nabla_d \beta(\mathbf{d}_c)^T(\mathbf{d}-\mathbf{d}_c) \geq \bar{\beta} \\ \text{or} \quad & p(\mathbf{d}_c) + \nabla_d p(\mathbf{d}_c)^T(\mathbf{d}-\mathbf{d}_c) \leq \bar{p} \\ & \| \mathbf{d}-\mathbf{d}_c \|_\infty \leq \Delta^k \end{aligned} \tag{2.85}$$

and for second-order surrogates:

$$\begin{aligned} \text{minimize} \quad & f(\mathbf{d}_c) + \nabla_{\mathbf{d}} f(\mathbf{d}_c)^T(\mathbf{d}-\mathbf{d}_c) + \tfrac{1}{2}(\mathbf{d}-\mathbf{d}_c)^T\nabla^2_{\mathbf{d}} f(\mathbf{d}_c)(\mathbf{d}-\mathbf{d}_c) \\ \text{subject to} \quad & \beta(\mathbf{d}_c) + \nabla_{\mathbf{d}} \beta(\mathbf{d}_c)^T(\mathbf{d}-\mathbf{d}_c) + \tfrac{1}{2}(\mathbf{d}-\mathbf{d}_c)^T\nabla^2_{\mathbf{d}} \beta(\mathbf{d}_c)(\mathbf{d}-\mathbf{d}_c) \geq \bar{\beta} \\ \text{or} \quad & p(\mathbf{d}_c) + \nabla_{\mathbf{d}} p(\mathbf{d}_c)^T(\mathbf{d}-\mathbf{d}_c) + \tfrac{1}{2}(\mathbf{d}-\mathbf{d}_c)^T\nabla^2_{\mathbf{d}} p(\mathbf{d}_c)(\mathbf{d}-\mathbf{d}_c) \leq \bar{p} \\ & \| \mathbf{d}-\mathbf{d}_c \|_\infty \leq \Delta^k \end{aligned} \tag{2.86}$$

For PMA trust-region surrogate-based RBDO, surrogate models of $f$ and $z$ are employed within a trust region $\Delta^k$ centered at $\mathbf{d}_c$. For first-order surrogates:

$$\begin{aligned} \text{minimize} \quad & f(\mathbf{d}_c) + \nabla_d f(\mathbf{d}_c)^T(\mathbf{d}-\mathbf{d}_c) \\ \text{subject to} \quad & z(\mathbf{d}_c) + \nabla_d z(\mathbf{d}_c)^T(\mathbf{d}-\mathbf{d}_c) \geq \bar{z} \\ & \| \mathbf{d}-\mathbf{d}_c \|_\infty \leq \Delta^k \end{aligned} \tag{2.87}$$

and for second-order surrogates:

$$\begin{aligned} \text{minimize} \quad & f(\mathbf{d}_c) + \nabla_{\mathbf{d}} f(\mathbf{d}_c)^T(\mathbf{d} - \mathbf{d}_c) + \tfrac{1}{2}(\mathbf{d} - \mathbf{d}_c)^T \nabla^2_{\mathbf{d}} f(\mathbf{d}_c)(\mathbf{d} - \mathbf{d}_c) \\ \text{subject to} \quad & z(\mathbf{d}_c) + \nabla_{\mathbf{d}} z(\mathbf{d}_c)^T(\mathbf{d} - \mathbf{d}_c) + \tfrac{1}{2}(\mathbf{d} - \mathbf{d}_c)^T \nabla^2_{\mathbf{d}} z(\mathbf{d}_c)(\mathbf{d} - \mathbf{d}_c) \geq \bar{z} \\ & \| \mathbf{d} - \mathbf{d}_c \|_\infty \leq \Delta^k \end{aligned} \tag{2.88}$$

where the sense of the $z$ constraint may vary as described previously. The second-order information in (2.86) and (2.88) will typically be approximated with quasi-Newton updates.

# Chapter 3

# Computational Model and Results

## 3.1 MEMS Computational Model

In Section 1.3, design issues with bistable MEMS are overviewed. In this section the specific MEMS tapered beam model is presented, including design parameters, uncertain parameters, geometry, boundary conditions, and the relevant Aria solver parameters. We conclude with some baseline results for the force–displacement curve, the beam displacement, and stress distribution.

### 3.1.1 Geometry, Design and Uncertain Variables, and Boundary Conditions

Figure 3.1 shows a drawing of one tapered beam leg (one quarter of the full switch system). A single leg is approximately 100 $\mu m$ wide and 5–10 $\mu m$ tall and is parametrized by the 13 design variables $\mathbf{d}$ indicated in Figure 3.1, including widths $W_i$ and lengths $L_i$ of beam segments as well as angles $\theta_i$ between segments. Along the right surface ($x = 0$) the $x$ displacement is fixed, and a $y$ displacement is applied in the negative direction. A fixed displacement condition is applied to the left surface (see Figure 3.2). The reaction force is the integral of the $y$ component of the normal stress integrated along the right surface ($x = 0$). With appropriate scaling of reaction force (to account for device thickness and number of legs), these allow the quarter model to reasonably represent the full four-leg switch system.

Due to manufacturing processes, fabricated geometry can deviate significantly from design-specified beam geometry. As a consequence of photo lithography and etching processes, fabricated in-plane geometry edges (contributing to widths and lengths) can be $0.1 \pm 0.08\,\mu m$ less than specified. This uncertainty in the manufactured geometry leads to substantial uncertainty in the positions of the stable equilibria and in the maximum and minimum force on the force–displacement curve. The manufactured thickness of the device is also uncertain, though this does not contribute as much to variability in the force–displacement behavior. Uncertain material properties such as Young's modulus and residual stress also influence the characteristics of the fabricated beam. For this application, two key uncertain variables are considered:

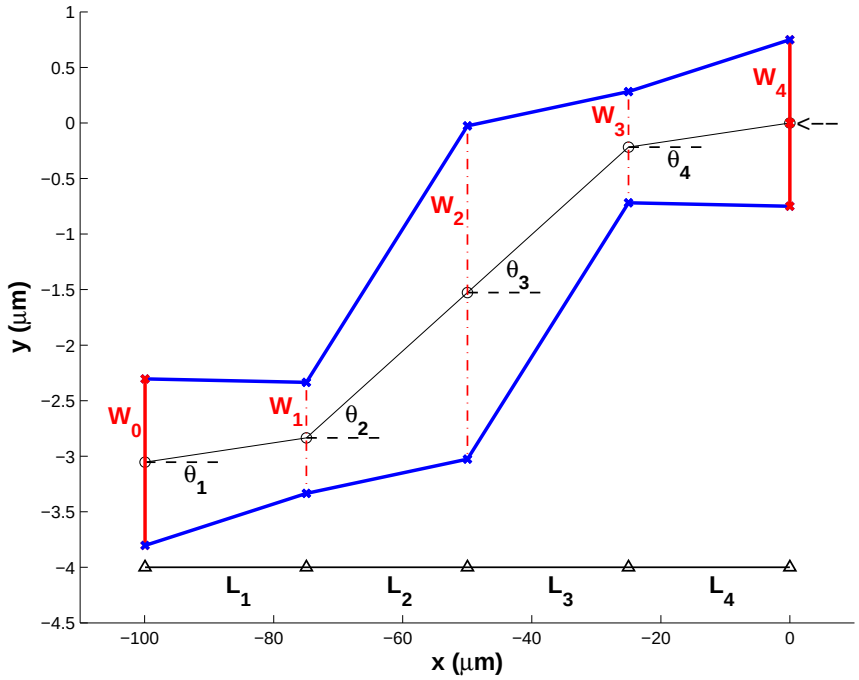


**Figure 3.1.** Design parameters for the tapered-beam fully-compliant bistable mechanism (geometry not to scale). Displacement is applied in the negative $y$ direction at the right face ($x = 0$), while at the left face, a fixed displacement condition is enforced.

$\Delta W$ (effect of edge bias, applied $\frac{\Delta W}{2}$ to each edge, yielding effective manufactured widths $W_i + \Delta W, i = 0, \ldots, 4$) and $S_r$ (residual stress in the manufactured device), with distributions shown in Table 3.1.

**Table 3.1.** Uncertain variables $\mathbf{x} = [\Delta W, S_r]$ used in UQ and RBDO.

| variable | mean ($\mu$) | std. dev. | distribution |
|---|---|---|---|
| $\Delta W$ (width bias) | -0.2 $\mu m$ | 0.08 | normal |
| $S_r$ (residual stress) | -11 Mpa | 4.13 | normal |

Iterative uncertainty quantification, reliability analysis, and design optimization are performed with DAKOTA. Throughout UQ or RBDO, for each set of specified geometric design parameters and realizations of uncertain variables, we create and mesh the tapered beam geometry using Sandia's FASTQ in batch mode [22].

In Section 2.2, for the error estimator studies, the geometric variables are fixed and the uncertain variables are taken to be their mean values. Then in Section 3.4, uncertainty

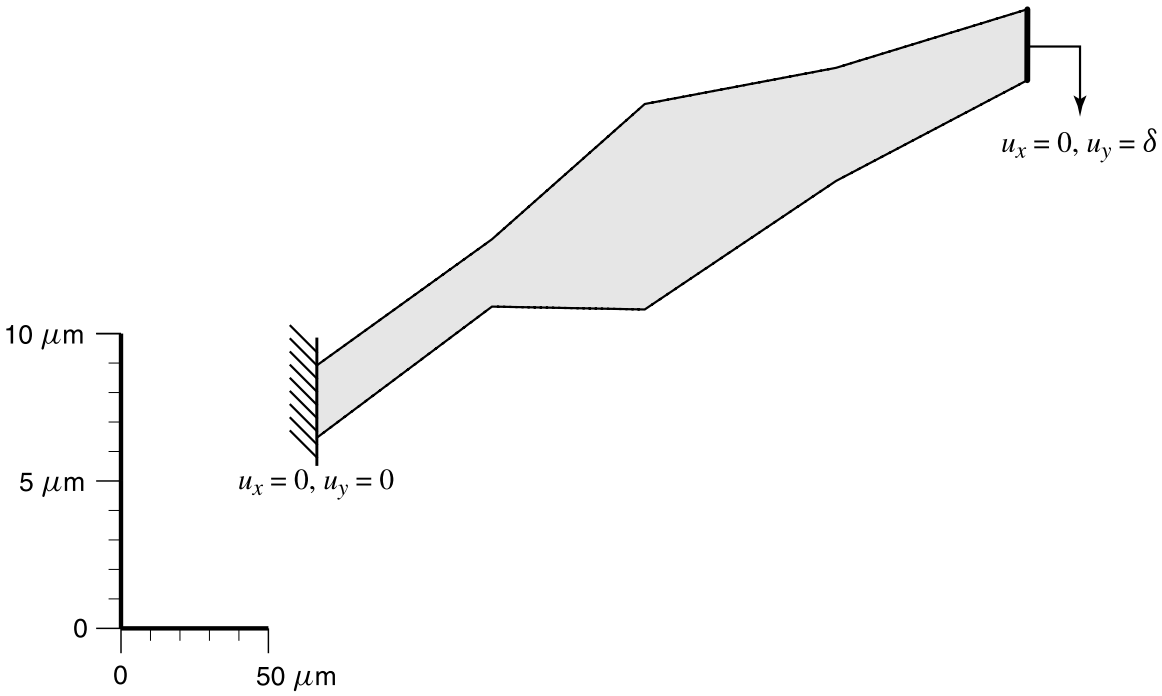


**Figure 3.2.** Boundary conditions and location of surface where force is calculated

quantification is performed for fixed geometry, considering the effect of the uncertain variables $\mathbf{x} = [\Delta W, S_r]$ on the reaction force For these studies, beam geometry is fixed at the baseline values shown in Table 3.2. In contrast, in Section 3.5, the beam is iteratively simulated with varying values of the geometric variables during RBDO.

### 3.1.2 Bistable MEMS Simulation and Baseline Results

In this section we describe the computations for bistable MEMS beam simulation and present baseline results, where the design parameters are fixed at the baseline values in Table 3.2 and the uncertain parameters are set at the mean values in Table 3.1. For all computational results in this report, finite element analysis is performed using the model described in Section 2.1, as implemented in the SIERRA code Aria, to simulate the nonlinear elastic deformation of the beam through discrete displacement steps to produce a force–displacement curve. Nonlinear solves employ a Newton method with the following parameters

```
Maximum Nonlinear Iterations = 20
Nonlinear Residual Tolerance = 1e-8
Nonlinear Correction Tolerance = 1e-4
Nonlinear Relaxation Factor = 1.0
```

**Table 3.2.** Values of tapered beam geometric parameters **d** used in UQ studies. Parameters are identified in Figure 3.1.

| parameter | value |
|---|---|
| $L_1$ | 2.803411216948874e+01 |
| $L_2$ | 2.441718869610307e+01 |
| $L_3$ | 3.057800292245615e+01 |
| $L_4$ | 3.055180849252218e+01 |
| $\theta_1$ | 4.200263518351102e+00 |
| $\theta_2$ | 2.480682485407754e+00 |
| $\theta_3$ | 2.464573895851033e+00 |
| $\theta_4$ | 2.384172184484739e+00 |
| $w_0$ | 1.355040383611968e+00 |
| $w_1$ | 1.274677949068451e+00 |
| $w_2$ | 3.480576539521997e+00 |
| $w_3$ | 2.006017307477350e+00 |
| $w_4$ | 1.332643531136223e+00 |

using a direct solver (amesos-superlu) for the required linear solves. Maximum and minimum force values as well as displacement equilibria are determined from the force-displacement curve. Maximum stress $S_{max}$ is calculated as the maximum Von Mises stress over all nodes and all displacement steps. All switch simulations employ the quarter model (single beam) system described above, with appropriate boundary conditions and multipliers to recover the full system.

In all results, units of force are $\mu N$ and units of displacement (including equilibrium positions) are $\mu m$. We plot in Figure 3.3 the force-displacement curve for the baseline case. Selected points are labeled for further investigation in Section 3.2. In Figure 3.4 we plot the nodal Von Mises stress for the displacement positions labeled in Figure 3.3. For these solutions, a uniform mesh of 12,800 linear elements was used. We observe large displacements and rotations of the beam, as well as localized large stresses at the corners.

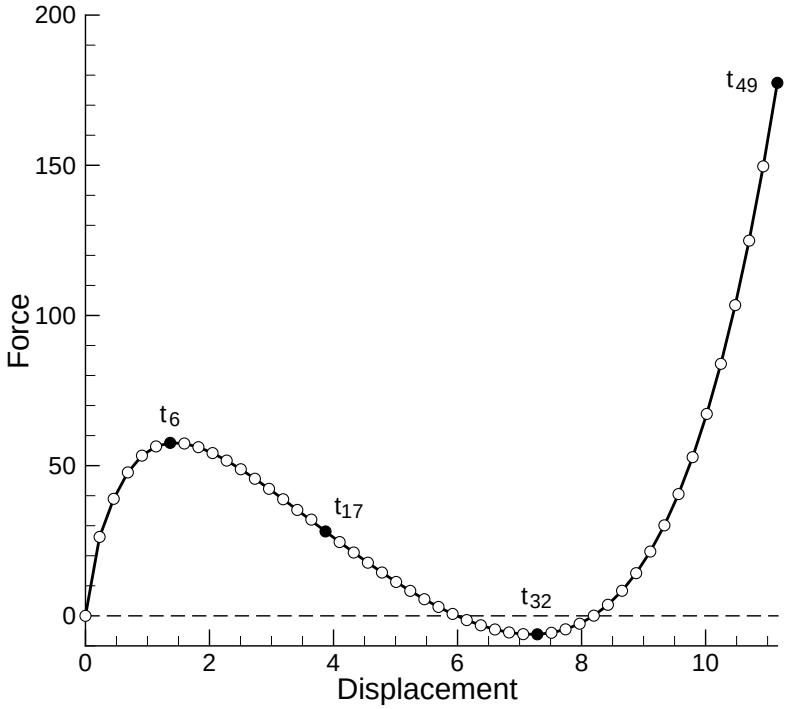


**Figure 3.3.** Baseline force–displacement curve with selected points indicated for further study in subsequent results.

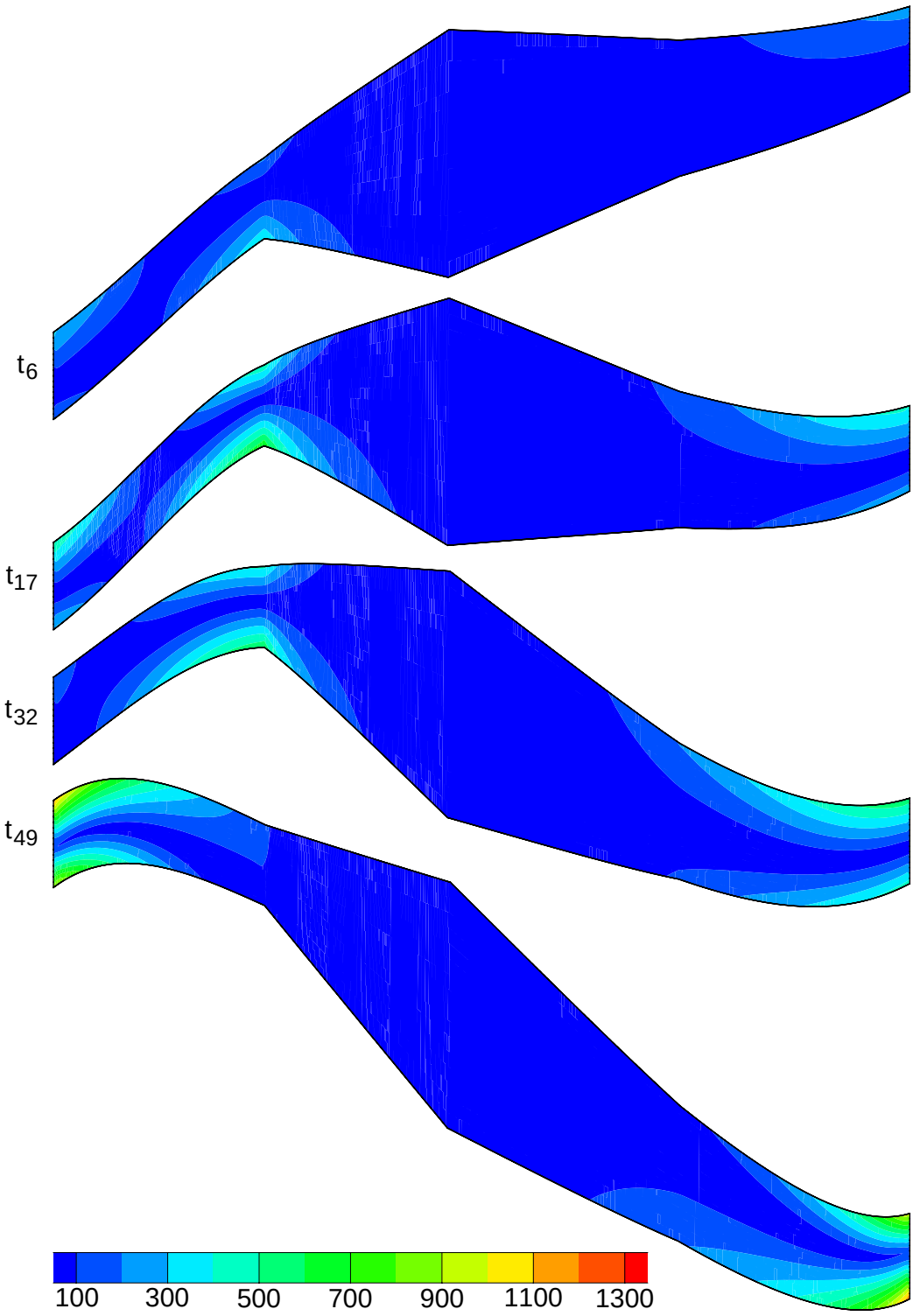


**Figure 3.4.** Von Mises stress on displaced beam for selected time steps ($y$ axis scaled by 10). Meshes contain 12,800 linear quadrilateral elements.

## 3.2 Error Estimation Results

In this section we present basic results to illustrate the error estimators described in Sec. 2.2. We test using both uniform and adaptive refinement, and compare the performance of the error estimators. As in Section 3.1.2, we fix the geometry parameters to be the default values and the uncertain parameters to be the mean values.

### 3.2.1 Error Estimation for Uniform Meshes

For any fixed mesh, we can compute the entire force–displacement curve and simultaneously compute an estimate of the error in the surface force at each step using $\eta^Q$. We plot our coarsest uniform mesh in Figure 3.5 for reference. Since the global

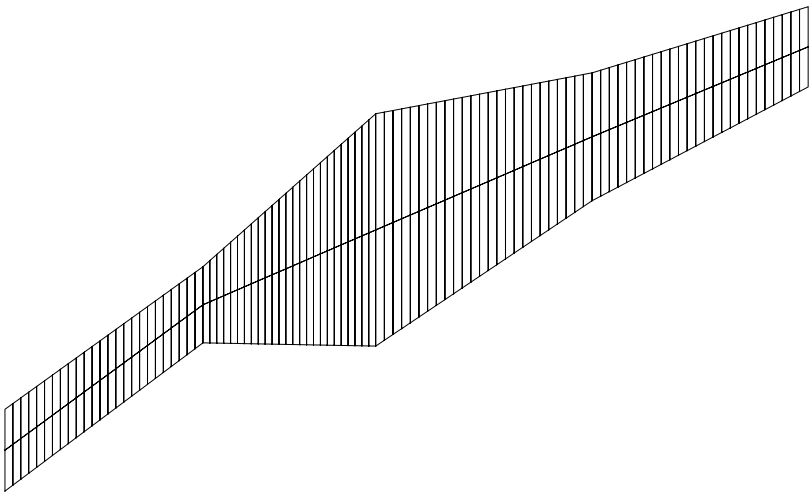

**Figure 3.5.** Coarse uniform 200 element mesh. ($y$ axis scaled by 10)

estimator $\eta^{ZZ}$ does not produce an estimate for the error in the surface force, we will not use it until the next section on mesh adaptivity. We first perform a study of the accuracy of the error estimator using a sequence of uniform meshes, which can be produced by uniformly refining the initial coarse mesh in Figure 3.5. Uniform mesh refinement is typically used in evaluating the performance of a posteriori error estimators for meshes that are fairly regular. This is also be useful for circumstances where one would like to use the error estimator as an error correction, such as in an optimization or uncertainty quantification algorithm. In contrast, in the next section we will evaluate the behavior of the estimators under local adaptive mesh refinement, which is generally a more stringent test of the estimator, because of the mesh irregularities.

Let us introduce the term "exact" error, which we define as the difference between the computed surface force and the force computed using a reference solution; the reference solution is computed on a fine mesh of 3200 quadratic elements. Let $\bar{Q}$ denote the surface force computed on the reference discretization. In order to assess the accuracy of the estimator, we compute the ratio of the estimator to the exact error. The ratio which is the global effectivity $\theta$ that was defined in (2.16). When $\theta$ is close to one, then the estimator is a reasonable predictor of the exact error in the surface force. Even if $\theta$ is only bounded in some interval

$$0 < c_1 \leq \theta \leq c_2,$$

where $c_1$ and $c_2$ are mesh–independent, then the estimator can be used to estimate the order of magnitude in the exact error or in adaptive mesh refinement algorithms.

Before we present results on the performance of the error estimator, we plot an example of the approximate dual solution $z_h$, defined in (2.20). Because the dual displacements $z$ do not vary as much as the primal displacements $u$, we only plot $z_h$ near the minimum force (time step 32 in Figure 3.3). We see in Figure 3.6 that the $y$ component of the solution has a strong linear variation in the $x$ direction, and that the $x$ component has a small linear variation in the $y$ direction.

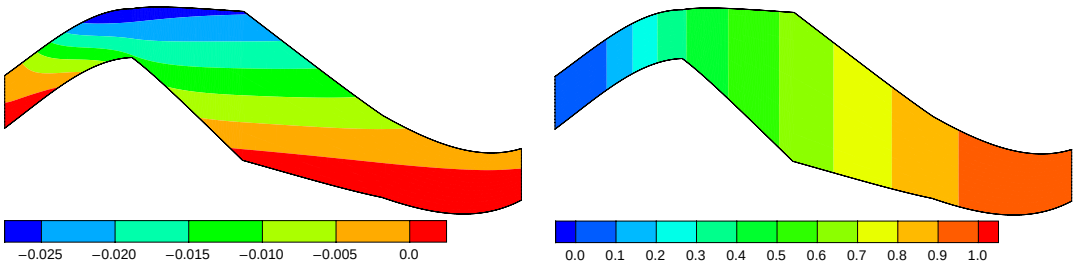


(a) X component (b) Y component

**Figure 3.6.** Dual displacement solution on displaced beam for time step 32 ($y$ axis scaled by 10). Mesh contains 12,800 linear quadrilateral elements.

In Figure 3.7(a) we plot the force–displacement curves computed using a sequence of uniformly refined meshes of linear elements along with a fine mesh of 3200 quadratic elements, which is used as a reference solution. Looking at the entire curve, only the curves from the two coarsest meshes are distinguishable from the finer grids. However, on closer inspection in a region near the minimum force value, we see in Figure 3.7(b) that the rate of convergence to the reference curve is superlinear. By measuring the error rates versus the number of nodes (or elements) in the mesh at fixed time values, we can estimate the rate more precisely (see Figure 3.10 below).

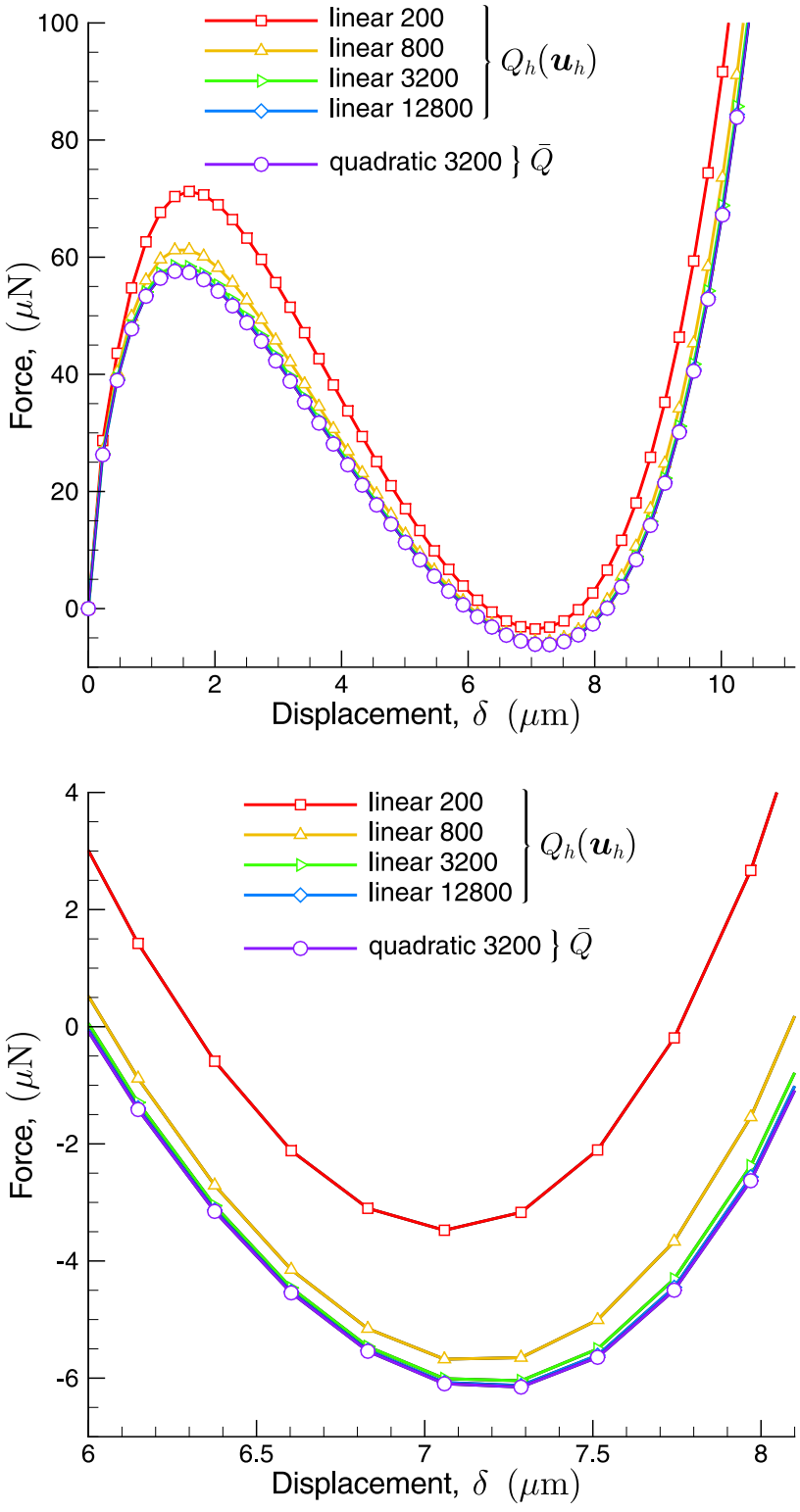


**Figure 3.7.** Force–displacement curves for uniform meshes of linear elements and a fine mesh of quadratic elements. Top figure is entire curve, bottom figure is curve near minimum force.

In Figure 3.8 we plot the error estimator $\eta^Q$ and the exact error in the surface force computed using linear elements for each displacement step. We can see that both the estimator and the exact error are typically negative, and converge to zero in absolute value as the mesh is refined. Again the error rate appears to be superlinear.

In order to quantify the accuracy of $\eta^Q$, we plot in Figure 3.9 the global effectivity $\theta$ for each displacement step. It is clear that this ratio is always between 0.7 and 1.4, and tends to one as the mesh is refined. Thus we have demonstrated that for sequences of *uniform* meshes, the estimator $\eta^Q$ is a reasonable predictor of the error in the surface force for our MEMS application problem. Furthermore, the predictive capability improves as the meshes are refined.

Finally, in order to assess the rate of convergence of the exact force error and the effectivity of the error estimator, we select a subset of time steps at which we plot the exact error and effectivity versus the number of nodes as the mesh is uniformly refined. These are chosen near local maxima, minima, and inflection points as seen in Figure 3.3. In Figure 3.10 we plot the exact error rates and global effectivity index versus the number of nodes in the mesh for each of the four selected time steps. Since the relation between the mesh size $h$ and number of nodes $N$ for a uniform mesh in $d$ dimensions is

$$h \approx N^{-1/d},$$

a second order error rate for our $2d$ problem would have a slope of $(-2/d = -1)$ in a log–log plot of error versus the number of unknowns. We have plotted a line with this slope in Figure 3.10(a) in order to compare the actual slopes with the formal second order slope. Upon inspection of the slopes in Figure 3.10(a), we see that the rate is nearly second order as a function of the mesh size. We also compare the effectivity index of the error estimator under uniform refinement in Figure 3.10(b) and see that it tends to one, as in Figure 3.9.

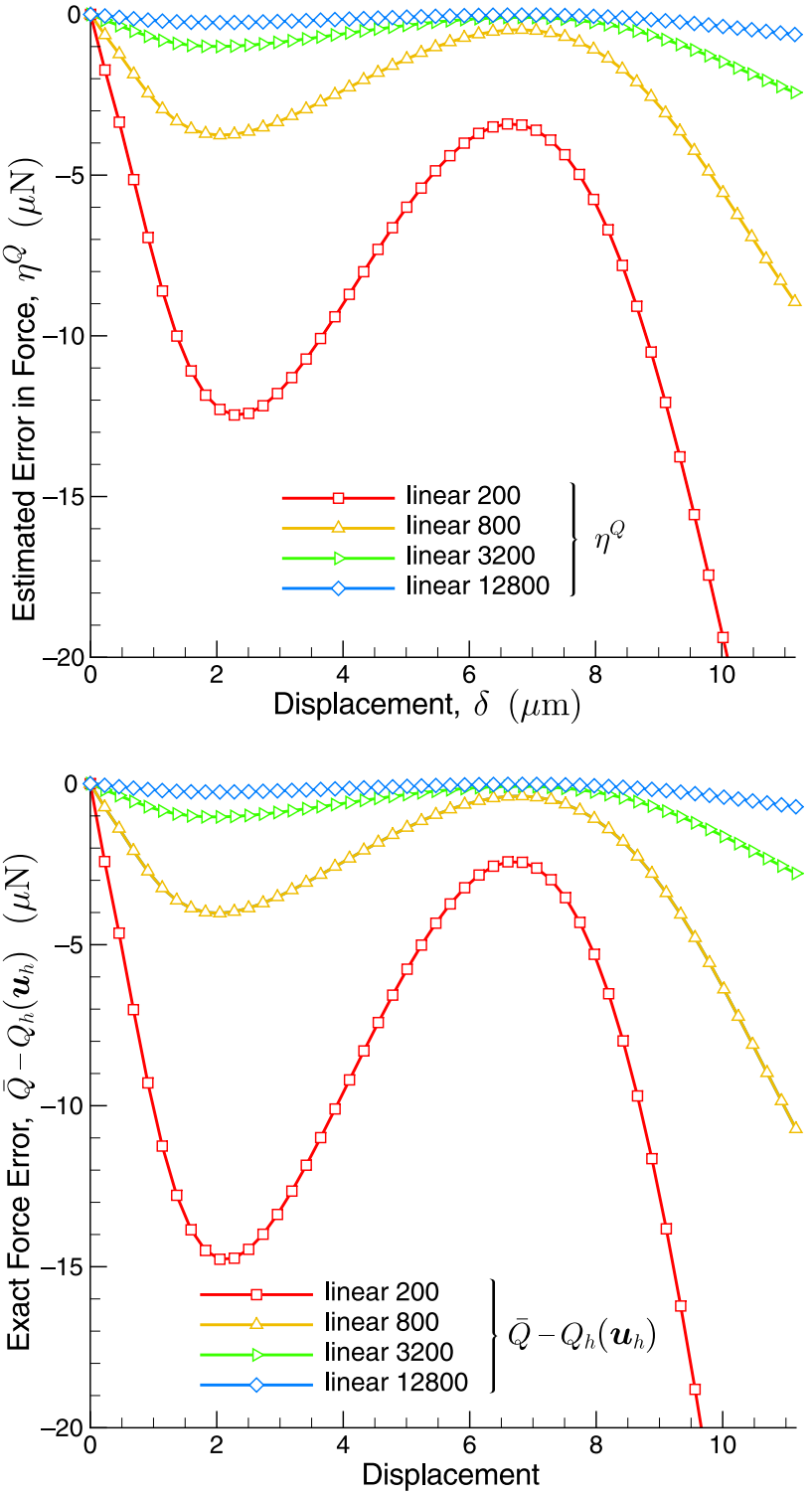


**Figure 3.8.** Estimated (top) and exact (bottom) error in the surface force for uniform meshes of linear elements.

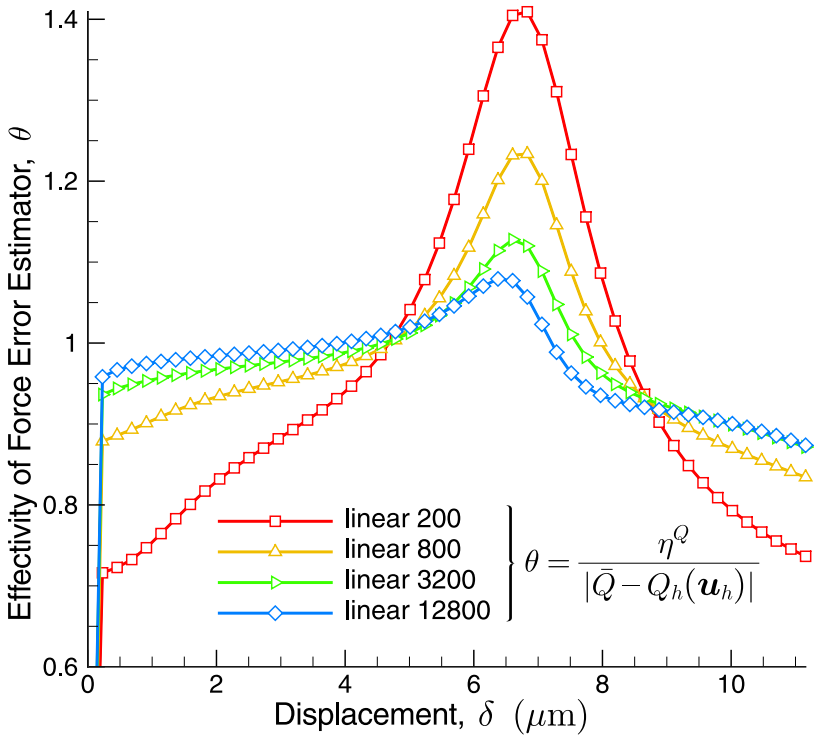


**Figure 3.9.** Force error effectivity for uniform meshes of linear elements.

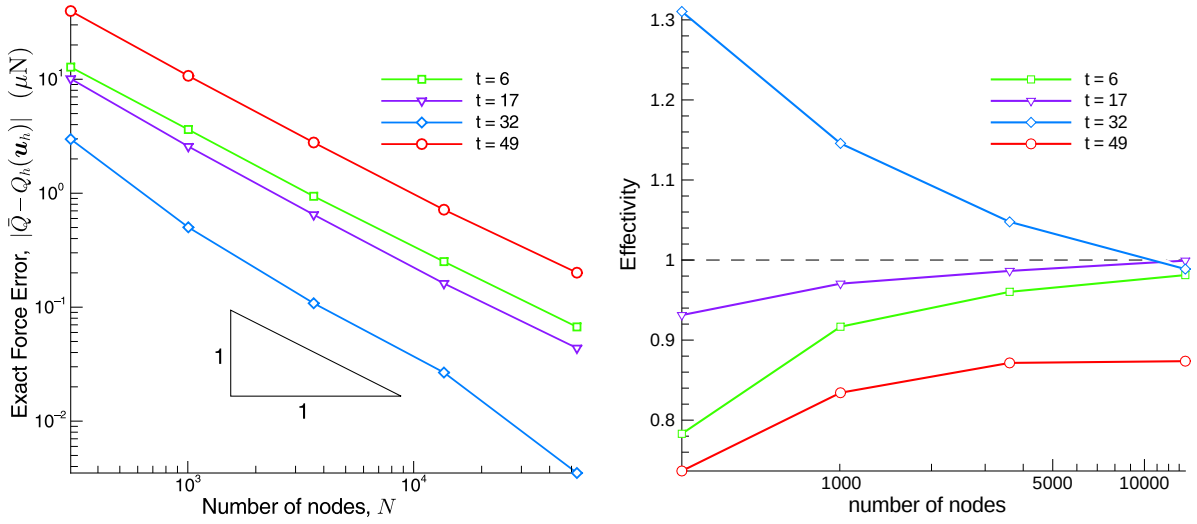


(a) exact error

(b) effectivity

**Figure 3.10.** Exact error and effectivity for uniform meshes at selected time steps.

### 3.2.2 Adaptive Mesh Refinement

We now turn to calculations with the error estimators $\eta^Q$ and $\eta^{ZZ}$ in an adaptive mesh refinement algorithm. In these calculations, the nonlinear solve at each time step is wrapped in an outer adaptive iteration. The adaptive iteration proceeds through the following steps:

1. Solve the nonlinear system for $u_h$
2. Calculate the error estimator $\eta = \eta^Q$ or $\eta^{ZZ}$
3. If the error estimator exceeds the given tolerance, then apply the marking algorithm to mark elements for refinement/coarsening; otherwise exit the adaptive loop
4. Adapt the mesh based on the markers and prolongate all fields (coordinates, displacements, etc.) onto the new mesh.

The adaptive iteration can also be terminated or skipped if the total number of elements exceeds some specified maximum, or if the current time step is outside some specified time interval.

The default parameters for the adaptive mesh refinement are given in Table 3.3. We note that the tolerances are different for the two estimators. For the quantity of interest estimator, the tolerance is in absolute units of the surface force, and is thus directly relevant to the overall accuracy of any calculation using the force quantity. Choice of this tolerance depends on various factors, such as, for example, the the relative size of the uncertainties in the problem parameters. On the other hand, the tolerance for $\eta^{ZZ}$ is based on a relative error in some global measure of the error in the displacement gradients. Because its relation to the error in the surface force is unknown, it can only be understood as a parameter that can be adjusted to produce various levels of adaptive mesh refinement. In particular, the value in Table 3.3 was chosen by trial and error for the application problem of interest. The refinement

| | $\gamma_{refine}$ | $\gamma_{coarsen}$ | $TOL$ |
|---|---|---|---|
| $\eta^Q$ | 0.50 | 0.01 | 0.5 |
| $\eta^{ZZ}$ | 0.50 | 0.01 | 0.0015 |

**Table 3.3.** Default parameters for adaptive mesh refinement

parameter $\gamma_{refine}$ was chosen in order to produce fairly aggressive refinement, minimizing the number of adaptive iterations required to reach the specified tolerance. The coarsening parameter $\gamma_{coarsen}$ was chosen to be fairly small, so as to allow some

coarsening in the mesh as the solution changes in time. In all cases, the marking strategy was based on the fixed fraction criteria defined in Section 2.2.6.

We plot the exact force error (in absolute value) obtained using adaptivity and the estimators $\eta^Q$ and $\eta^{ZZ}$ using a coarse uniform mesh (200 elements) and various error tolerances in Figure 3.11. These tolerances were chosen to be $QTOL = \{4, 2, 1, 0.5, 0.25, 0.0125\}$ for $\eta^Q$ and $GTOL = \{0.008, 0.006, 0.004, 0.002, 0.001\}$ for $\eta^{ZZ}$. As the error tolerance – indicated by the horizontal line in Figure 3.11(a) – is varied, we see that when using $\eta^Q$, the exact error is nearly always reduced below the specified tolerance. In contrast, the adaptive tolerance for the global estimator $\eta^{ZZ}$ does not control the error in the surface force directly. Instead, we see that as the tolerance is reduced, adaptivity based on the global error estimator gradually reduces the exact error in the force, through a much less smooth process than can be obtained using the quantity of interest estimator. The ability to adapt the mesh so that the exact error is near or below a specified tolerance is directly related to the accuracy of the error estimator. In Figure 3.12 we plot the global effectivity of the estimator $\eta^Q$. We see that even under the conditions of local mesh refinement, the error estimator is still quite accurate throughout the series of displacement steps.

We can also illustrate each actual adaptive iteration, as defined above, by plotting all of the error–displacement data points on the same graph. This means that for a given displacement step, there can be multiple output points as the adaptive algorithm adapts the mesh to minimize the global error estimator. In Figure 3.13 we plot such a data set for the exact and estimated error computed using the estimator $\eta^Q$ and various refinement tolerances. For this example we have increased the refinement parameter $\gamma_{refine}$ to the value 0.9 in order to allow for more adaptive refinement steps. Looking at any fixed displacement step, we can also see the number of adaptive iterations taken indicated by the points on the same vertical line. Also, we can see where the error decreases, typically from refinement of elements, and where it sometimes increases, typically from coarsening of elements. We see that while the estimator is reduced below the tolerance at each displacement step, the exact error may not be less than the tolerance. This is related to the accuracy of the estimator, which improves as the error tolerance is decreased. However, the adaptive algorithm maintains the *estimated error* to be less than the error tolerance in absolute value. We can also plot the data for the exact error obtained using the global estimator $\eta^{ZZ}$. In Figure 3.14 we see that the exact error in the force is reduced by the adaptive refinement iterations. However, because the estimator is not based on the error in the force, there is no reliable criteria to start or stop the adaptivity. As a result, the error generally tends to zero as the refinement tolerance is reduced, but not in a way that can be predicted or controlled.

As we did for the case of uniform mesh refinement, we present in Figure 3.15 the error rates for both estimators obtained using adaptivity at our sample points on the force–displacement curve. At the selected time steps, the number of nodes, estimated error, exact error, and effectivity were computed for $\eta^Q$. For $\eta^{ZZ}$ only the number of

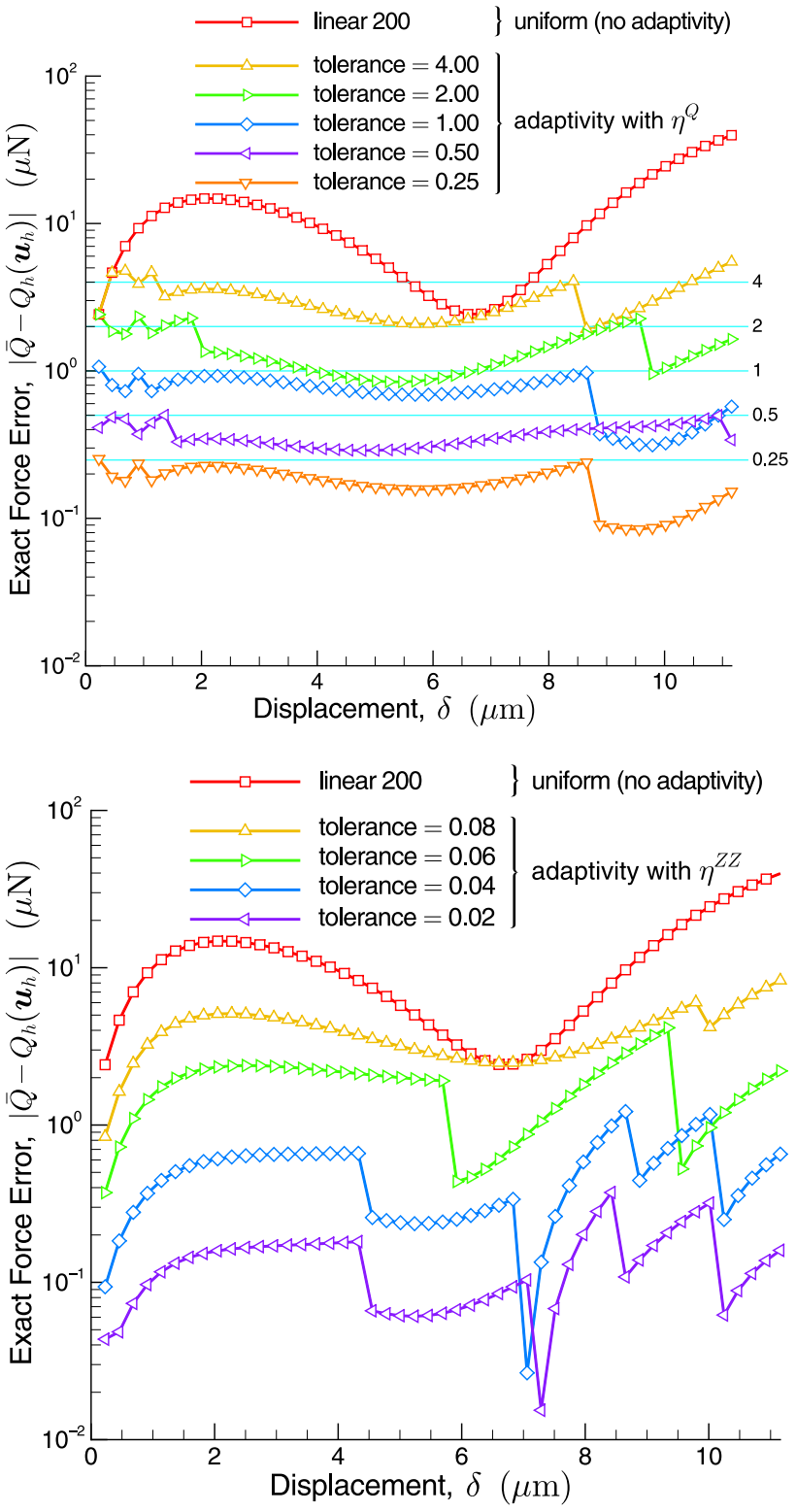


**Figure 3.11.** Exact error for adaptive meshes using $\eta^Q$ (top) and $\eta^{ZZ}$ (bottom).

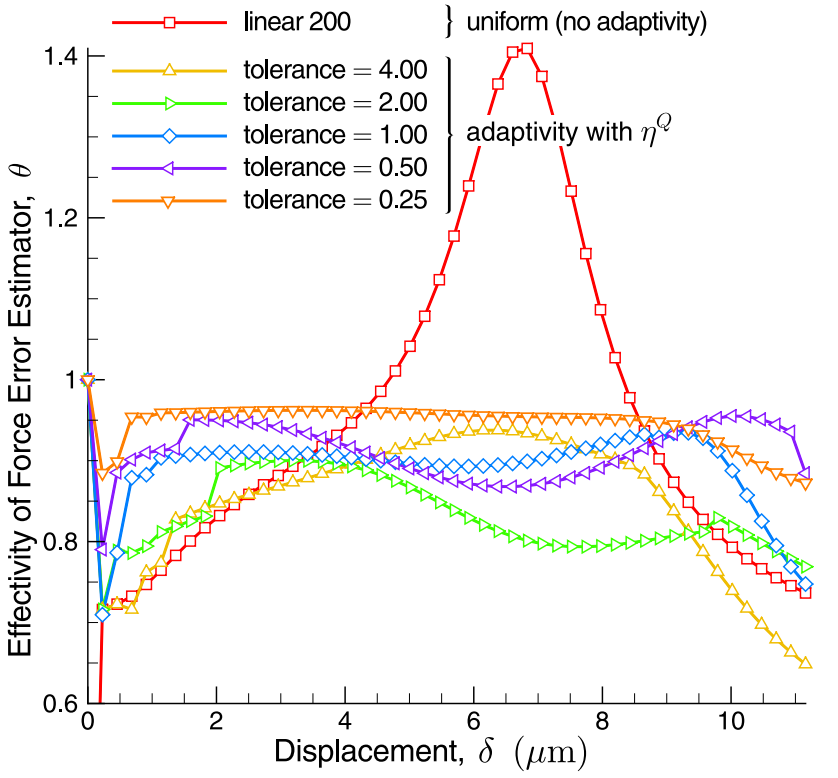


**Figure 3.12.** Effectivity for adaptive meshes using $\eta^Q$.

nodes and exact error were computed. As in the case of linear elements and uniform refinement in the previous section (Figure 3.10), we see nearly a second order rate of convergence. We also plot the effectivity for adaptivity with $\eta^Q$ in Figure 3.16. In the adaptive case, the effectivity is typically less than one, indicating that the estimator is underestimating the exact error. However, the effectivity is between 0.65 and 1.3 and tends to one, as in the case of uniform mesh refinement.

In order to gain some understanding of the local mesh adaptivity that is driven by the local element error estimators $\eta_K^Q$, in Figure 3.17 we plot the meshes near the right side of the beam in the reference configuration for four error tolerances. Since this is where the postprocessed surface force is calculated, we expect that the computed surface force will be sensitive to the mesh in this region. The plots of the meshes show a gradual refinement into the surface, with a very localized refinement occurring in the upper right corner of the beam. Similarly, we can plot a sequence of adapted meshes obtained from using the local element error indicators $\eta_K^{ZZ}$. In Figure 3.18 we see that the mesh refinement grades the mesh towards the end of the beam where the force is measured. However, the refinement is nearly uniform within patches, without any of the local features that are seen in Figure 3.17 when adapting with $\eta_K^Q$.

We conclude this section with some results that relate to the UQ/RBDO calculations in Sections 3.4 and 3.5. We first explore the possibility of adding the quantity of interest error estimator $\eta^Q$ to the computed force. This can be done in both uniform and adaptive refinement, in order to compute a more accurate force as we see in our examples. In Figure 3.19 we plot the exact error in the force using either just the postprocessed force defined in (2.15) or else the corrected force defined as the sum of the postprocessed force and the error estimator $\eta^Q$. We can see that the corrected force is always more accurate than the simple postprocessed force, under both uniform and adaptive refinement. Moreover, for some points under uniform refinement in Figure 3.19(a), the error in the corrected force appears to be converging at a higher rate than that of the simple force. This effect is even stronger under adaptivity, as seen in Figure 3.19(b), where the rate for the corrected force appears to be approximately $O(N^{-2})$, or twice the rate of the simple force.

Because we plan to use the error estimator $\eta^Q$ as a correction to the force, we are also interested in the possibility that the corrected force curve will avoid the non–smooth behavior that can occur when the mesh is adapted and the force may change significantly. In Figure 3.20 we plot some portions of the force–displacement curve to illustrate the smoothing effect of using the corrected force instead of the simple force in the case of adaptivity. The kinks in the simple force–displacement curve arise from the adaptive iterations which become active when the error tolerance is not maintained. However, the corrected force is less sensitive to the mesh adaptivity, and therefore produces a smoother force–displacement curve.

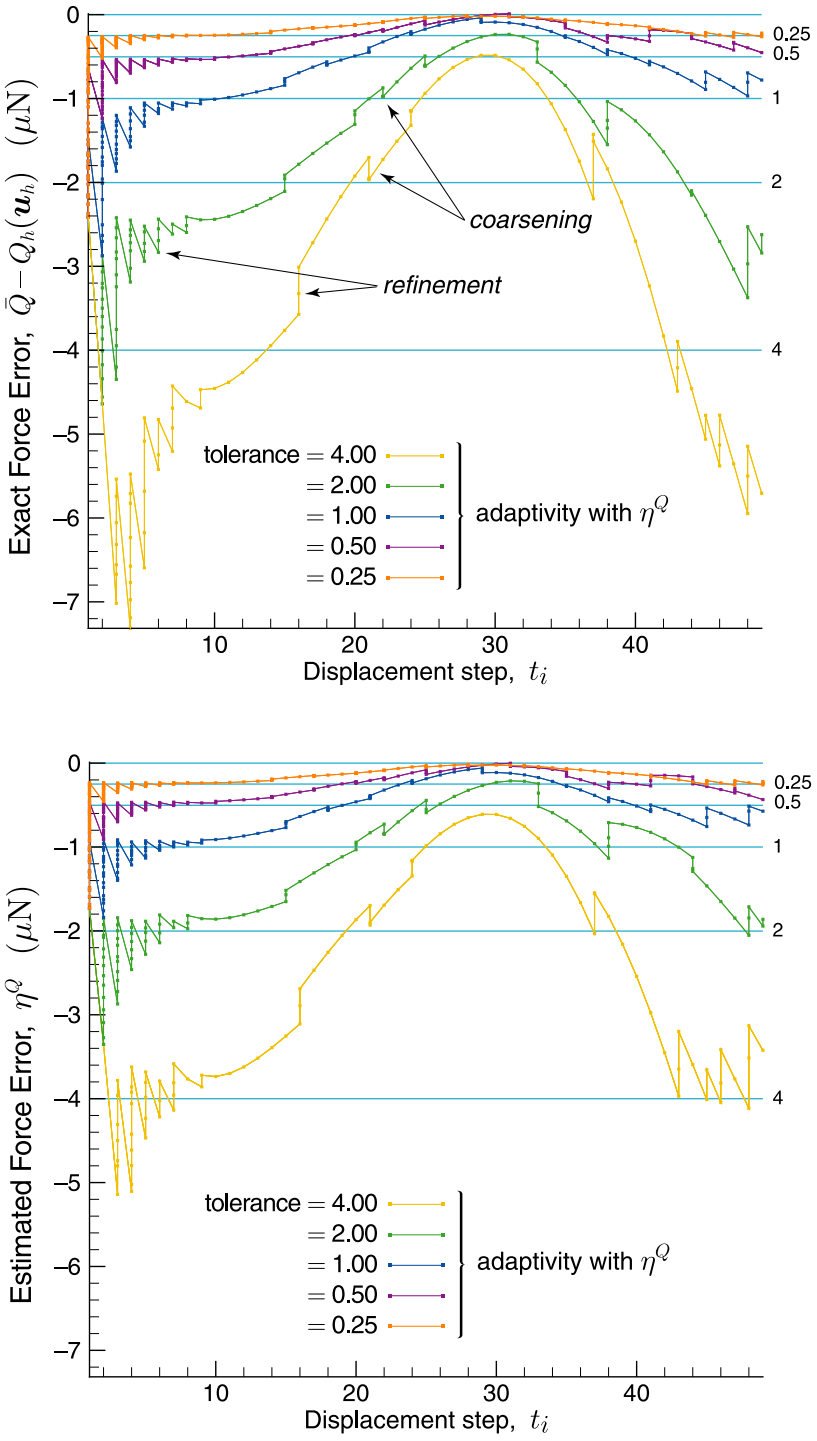


**Figure 3.13.** Exact (top) and estimated (bottom) error for adaptive meshes using $\eta^Q$ for all iterations.

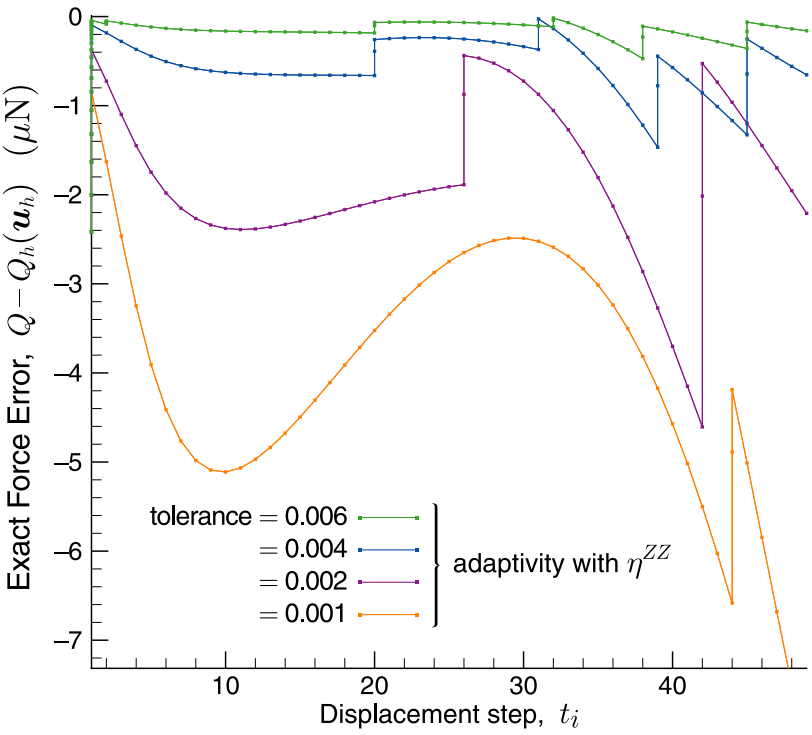


**Figure 3.14.** Exact error for adaptive meshes using $\eta^{ZZ}$ for all iterations.

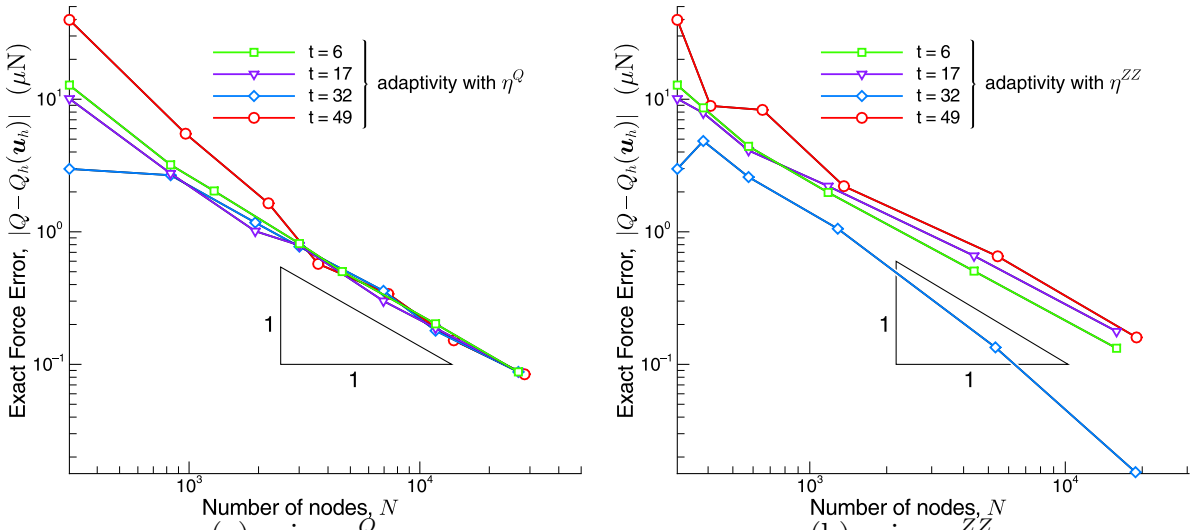


(a) using $\eta^Q$ (b) using $\eta^{ZZ}$

**Figure 3.15.** Exact error for meshes adapted using $\eta^Q$ and $\eta^{ZZ}$ at selected time steps.

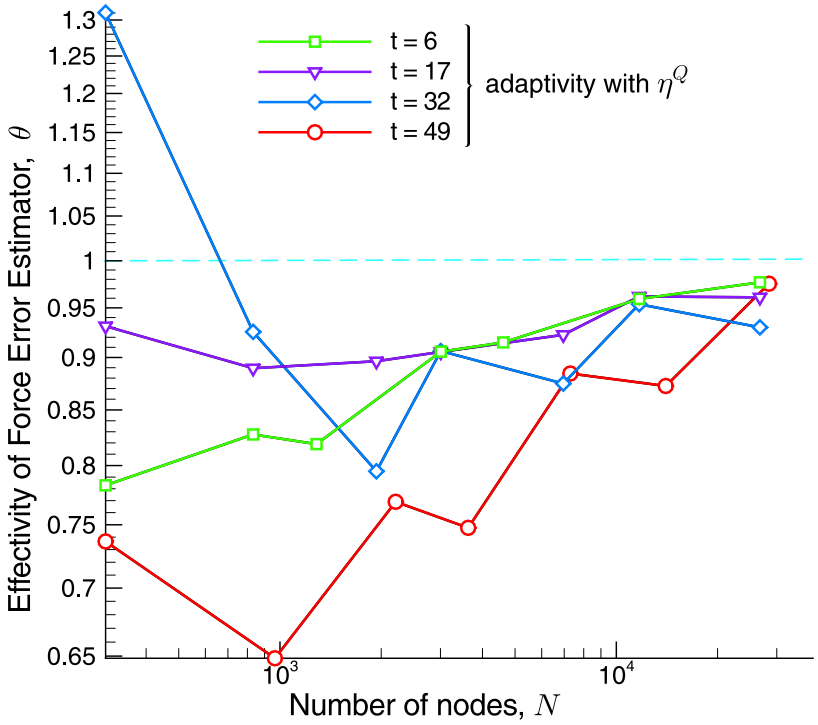


**Figure 3.16.** Effectivity for adaptive meshes using $\eta^Q$ at selected time steps.

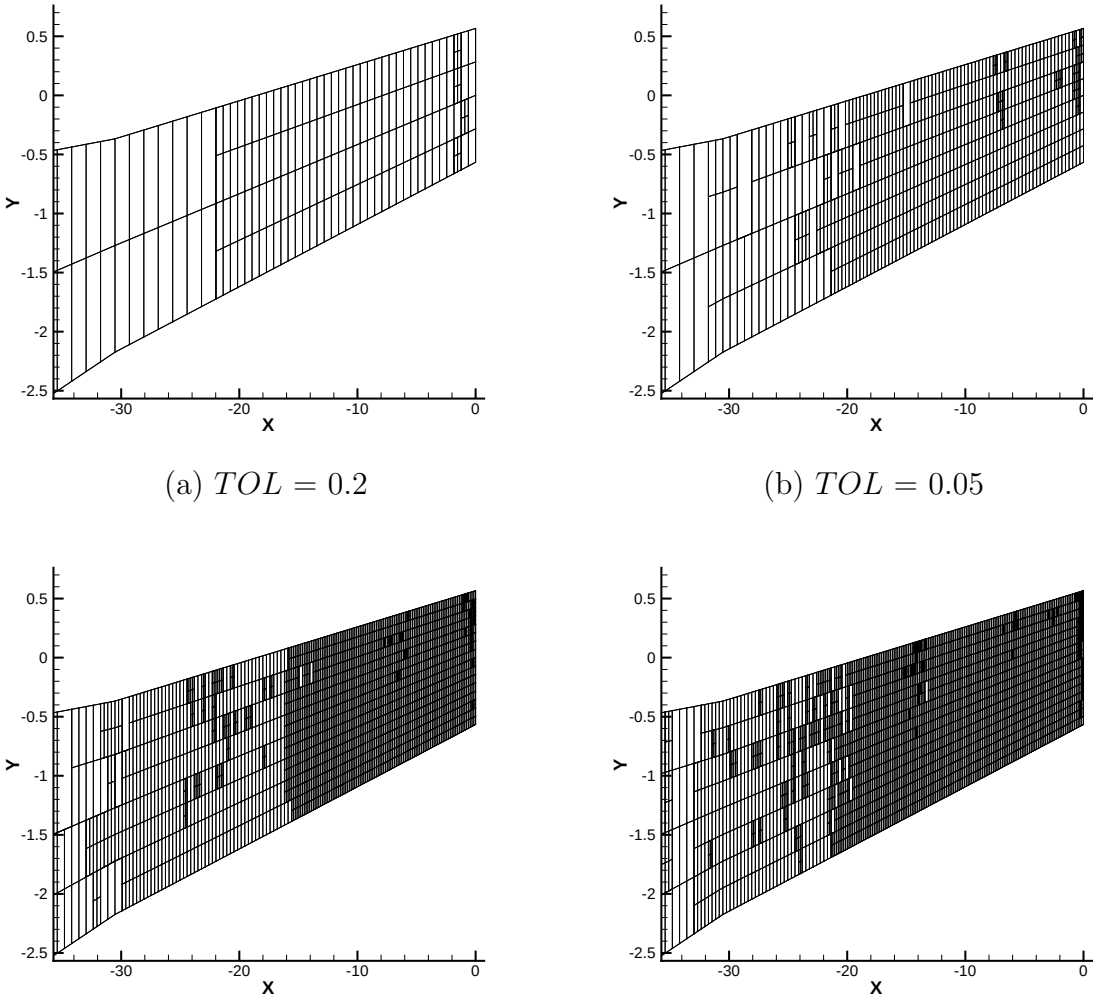


(a) $TOL = 0.2$

(b) $TOL = 0.05$

(c) $TOL = 0.025$

(d) $TOL = 0.0125$

**Figure 3.17.** Refined meshes near the right side of the beam at time step 32. Adapted using $\eta^Q$ and various global error tolerances (given in units of force).

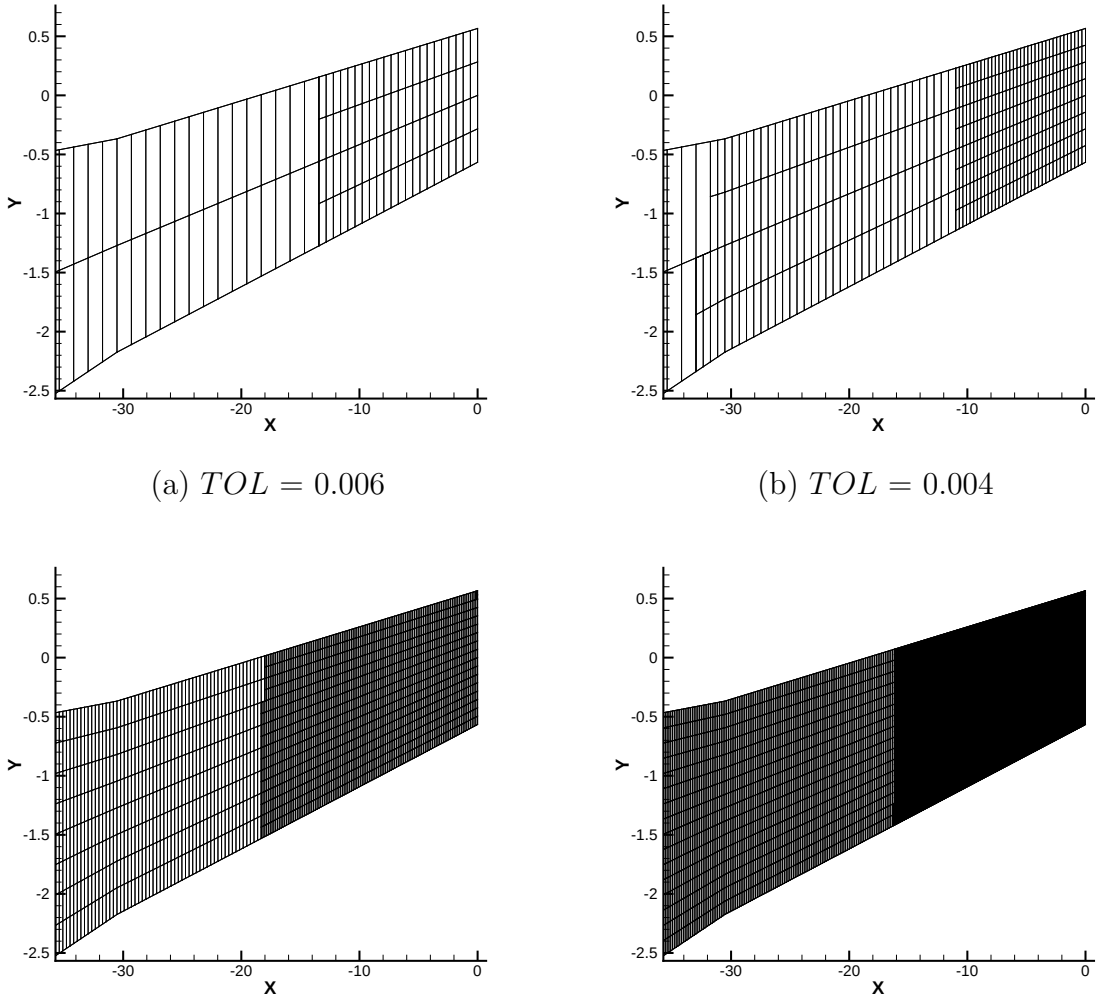


(a) $TOL = 0.006$

(b) $TOL = 0.004$

(c) $TOL = 0.002$

(d) $TOL = 0.001$

**Figure 3.18.** Refined meshes near the right side of the beam at time step 32. Adapted using $\eta^{ZZ}$ and various global error tolerances (given in relative units).

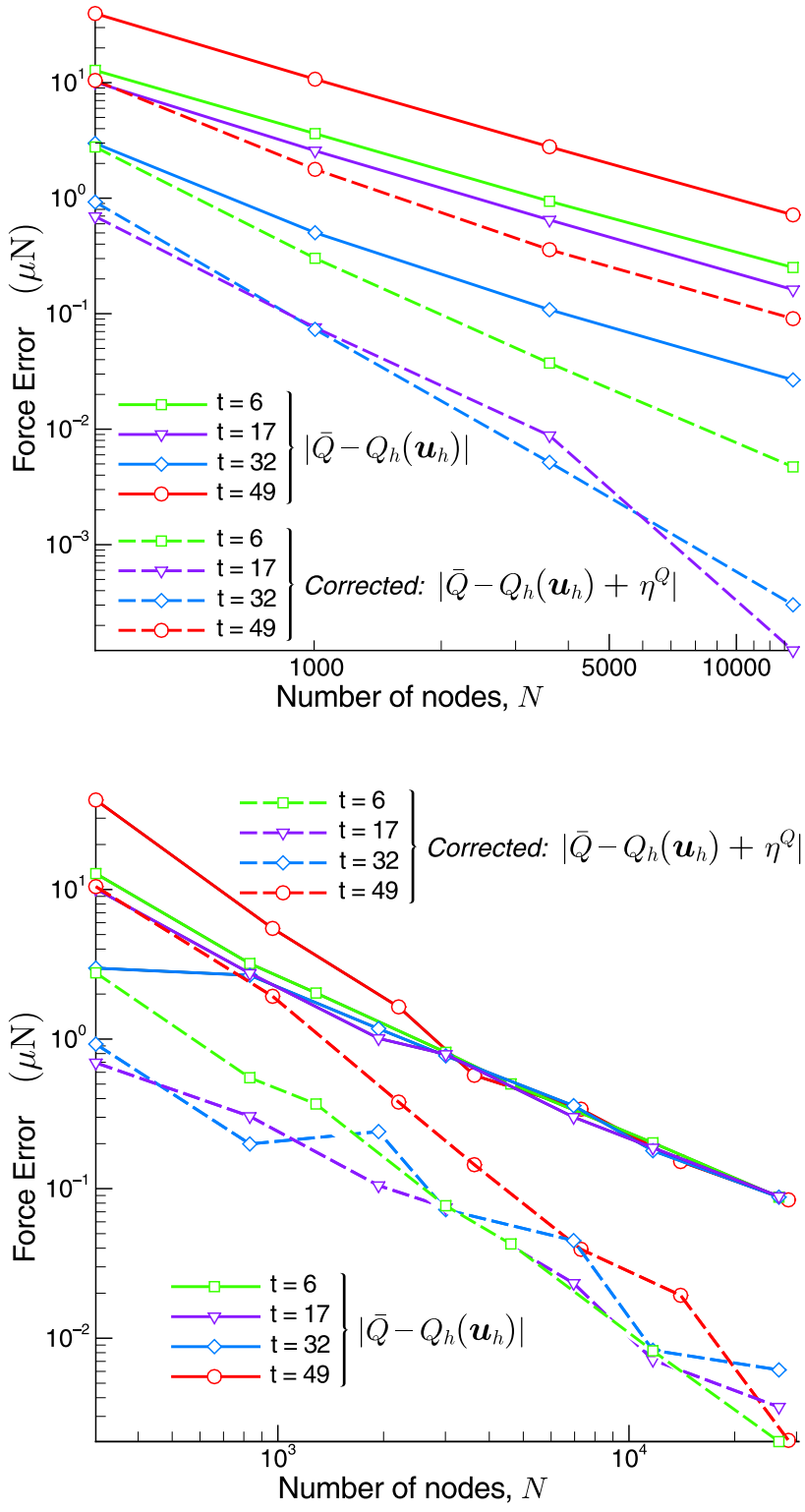


**Figure 3.19.** Error rates for corrected force at selected time steps using $\eta^Q$ with uniform meshes (top) and adapted meshes (bottom).

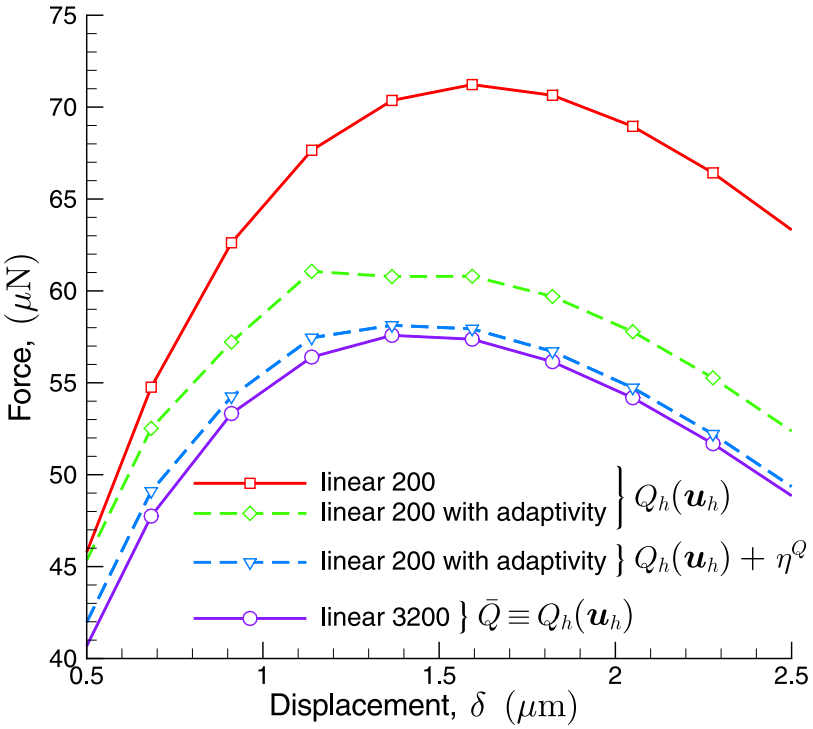


(a) displacement interval $[0.5, 2.5]$

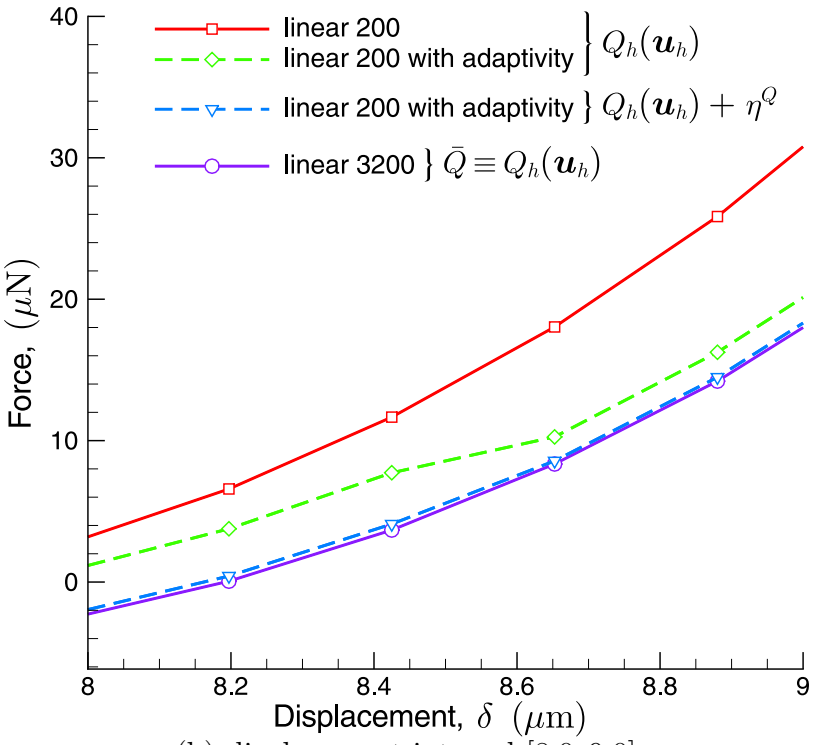


(b) displacement interval $[8.0, 9.0]$

**Figure 3.20.** Smoothing by error correction for meshes adapted using $\eta^Q$

## 3.3 Parameter Study Results

This section investigates the dependence of discretization errors on model input parameters. Section 3.3.1 presents parameter study results for the two uncertain variables, and Section 3.3.2 presents results for the thirteen design variables. The intent is to assess the need for parameter adaptive approaches to solution verification.

### 3.3.1 Uncertain variables

For the 800 linear element mesh, Figure 3.21 shows the variation of the quantity of interest error estimates $\eta^Q$ as a function of the two uncertain variables. Results are presented for the four simulation displacement steps indicated in Figure 3.3 and the parameter range is $\pm 3$ standard deviations. Figure 3.22 shows similar plots for the exact error when using the 800 linear element mesh (error measured relative to the 3200 quadratic element reference mesh). The trends in the error estimates are nearly identical to the trends in the exact errors, suggesting that the quantity of interest error estimator is a reasonable predictor of true error across a range of uncertain variable values.

The regions in parameter space where the error is largest are not consistent across timesteps. For example, in Figure 3.21, for $t = 6$ (northwest plot), the largest errors correspond to the most negative variable values, but for the other timesteps they correspond to the most positive variable values. This is likely because errors in force are strongly dependent on the total stress field, resulting from the sum of the residual pre-stress and the stress induced from the applied displacement. As expected, residual stress is an influential variable, but the sense is inconsistent for different steps since the residual pre-stress may alternate between augmenting or reducing the total stress.

Figure 3.23 shows the error estimate relative to the force predicted by the reference mesh. The relative error plots are more qualitatively consistent across most displacement steps, however for the displacement at $t = 32$ (southwest plot), the region of largest error corresponds to the most positive variable values, in contrast to the other three time steps, where it occurs for the most negative values. The relative error has significantly greater sensitivity to residual stress than to width bias.

Overall, the most important conclusion is that the error estimates are significant functions of the uncertain variables. Relative errors vary by a factor of two or more over the uncertain parameter ranges.

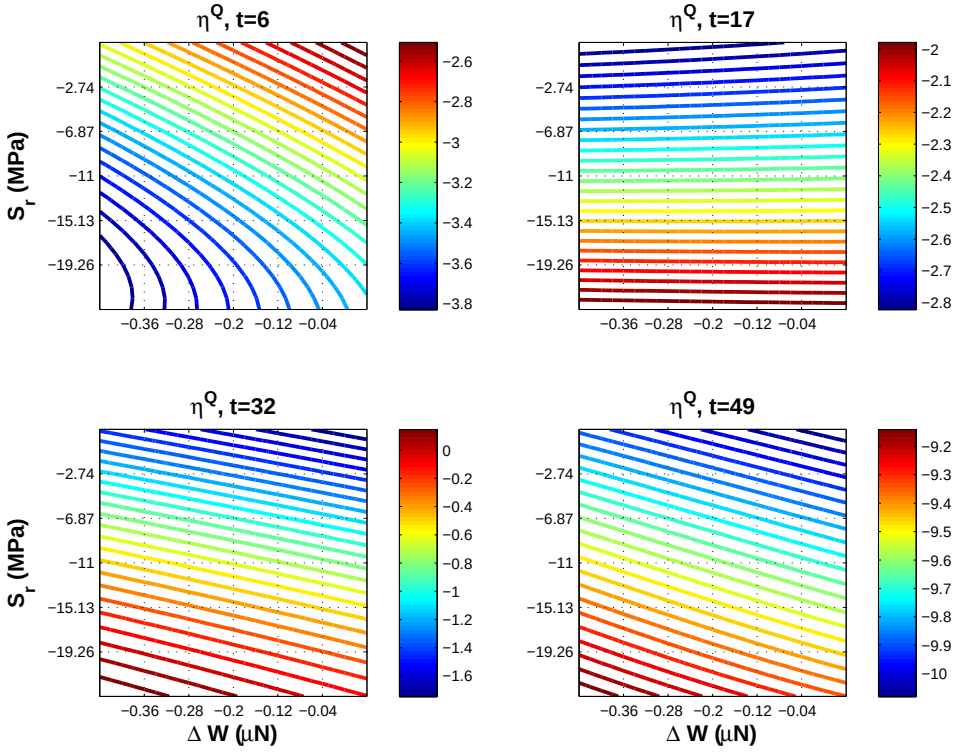


**Figure 3.21.** Estimated error in force as a function of uncertain variables.

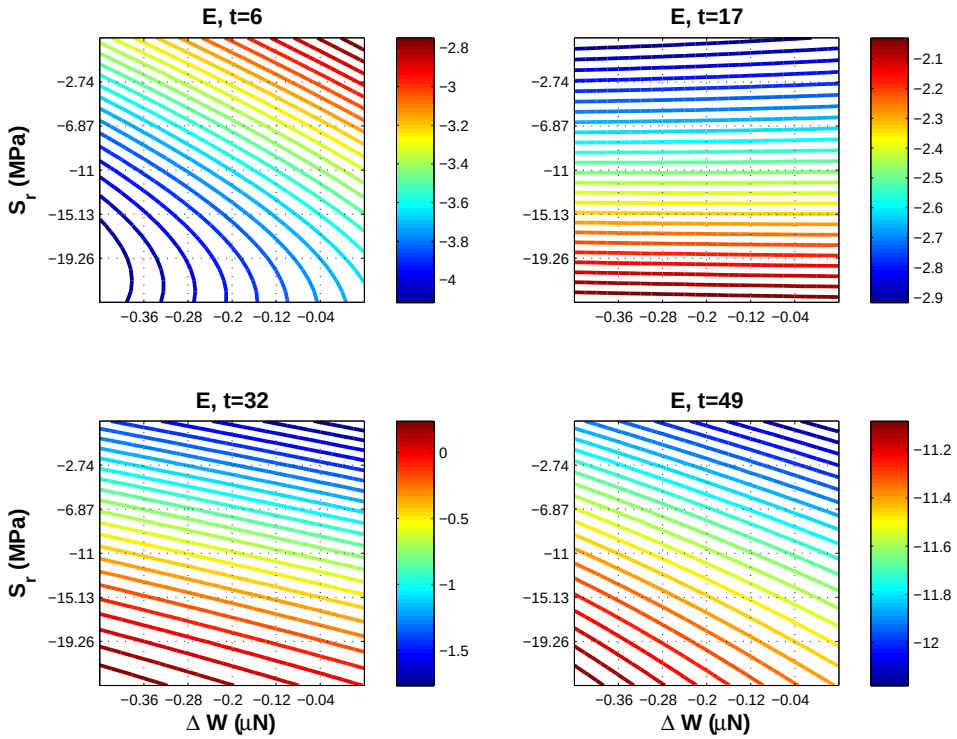


**Figure 3.22.** Exact error in force as a function of uncertain variables.

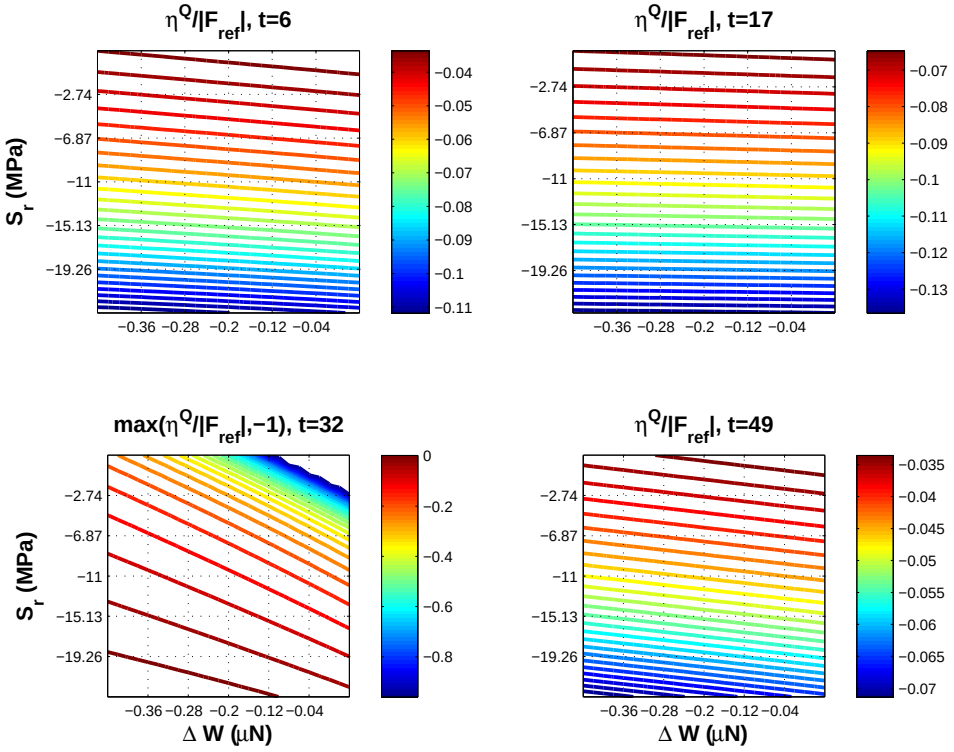


**Figure 3.23.** Estimated force error relative to force magnitude as a function of uncertain variables.

### 3.3.2 Design variables

Figure 3.24 shows the variation of the quantity of interest error estimates as a function of the thirteen design variables. Each line represents a one-dimensional parameter study, wherein one variable varies between the bounds listed in Table 3.6 and the others are anchored at nominal values (each taken to be the midpoint of the [l.b., u.b.] intervals in Table 3.6). Again, results are presented for four different displacement steps from the simulation.

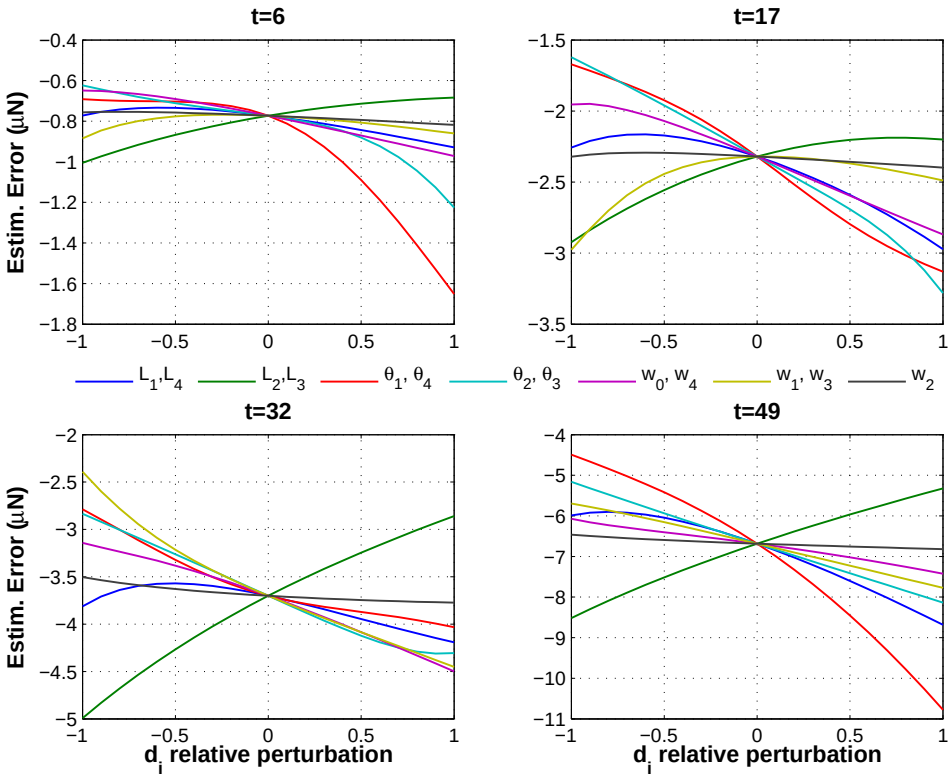


**Figure 3.24.** Estimated error in force as a function of design variables.

Once again, error estimates vary by a factor of two or more over the parameter ranges. Thus, a model with acceptable discretization errors for one set of design or uncertain parameters could have a significantly higher level of error for another. This validates the need for solution verification approaches which adapt for changing error levels as uncertainty quantification and optimization algorithms vary parameter values.

## 3.4 Uncertainty Quantification Results

This section describes uncertainty quantification for the bistable microelectromechanical system through the application of reliability analysis algorithms described in Section 2.3. The effect of uncertain variables on the response $z = F_{min}$ is evaluated using the model of the MEMS from Section 3.1, both with and without error estimation techniques from Section 2.2.

Most results in this section are generated using performance measure approach (PMA) reliability analysis (2.48) to determine the response levels $z = F_{min}$ corresponding to 13 specified probability levels

$$\bar{p} \in \{0.01, 0.05, 0.1, 0.2, \ldots, 0.8, 0.9.0.95, 0.99\} .$$

The required MPP search employs the AMV$^2$+ approximation to the limit state, as described by (2.60), with SR1 quasi-Hessians (2.74). When needed, gradients with respect to the uncertain variables $\mathbf{x}$ are computed using central differences with a 0.1% relative step size. These PMA results are compared to those resulting from Latin Hypercube Sampling (LHS) over the uncertain variable space.

For further comparison purposes, RIA formulations (2.47) are also considered, mapping specified response levels $\bar{z}$ to corresponding probability levels. The AMV$^2$+ approximation is again used to speed the convergence of the MPP search. In the RIA case, both first- and second-order probability integrations are considered, as contrasted in Section 2.3.2.2. Second-order probabilities are informed by either SR1 quasi-Hessians or full finite difference Hessians (2.72).

Cumulative distribution functions (CDFs) are used to display the results from PMA- and RIA-based reliability analyses, considering the effect of uncertain variables on the minimum force. The effect of choice of finite element meshes, polynomial degree of elements, use of quantity of interest error correction, and use of adaptivity on these CDFs is explored. We illustrate the array of potential discretization options in Figure 3.25. In the following results, "reference" denotes a fine mesh of 3200 quadratic elements.

Figure 3.26 shows CDFs generated with the reference mesh and a sequence of meshes with linear elements (200, 800, 3200, 12800) to demonstrate the convergence of CDFs under uniform refinement. Table 3.4 shows the computational time required for each of these analyses in terms of both function evaluations and average time per evaluation as well as the z-space discrete $L^2$ error between the various approximations and the reference CDF, calculated over the 13 requested probability levels $\bar{p}_i$ as

$$\sqrt{\frac{1}{13}\sum_{i=1}^{13}\left|z_{\bar{p}_i}^{ref} - z_{\bar{p}_i}^{approx}\right|^2}. \tag{3.1}$$

We plot this error versus number of nodes in Figure 3.27 for the AMV$^2$+ data in Table 3.4. The $L^2$ error for the finest linear mesh considered (12800 elements) is

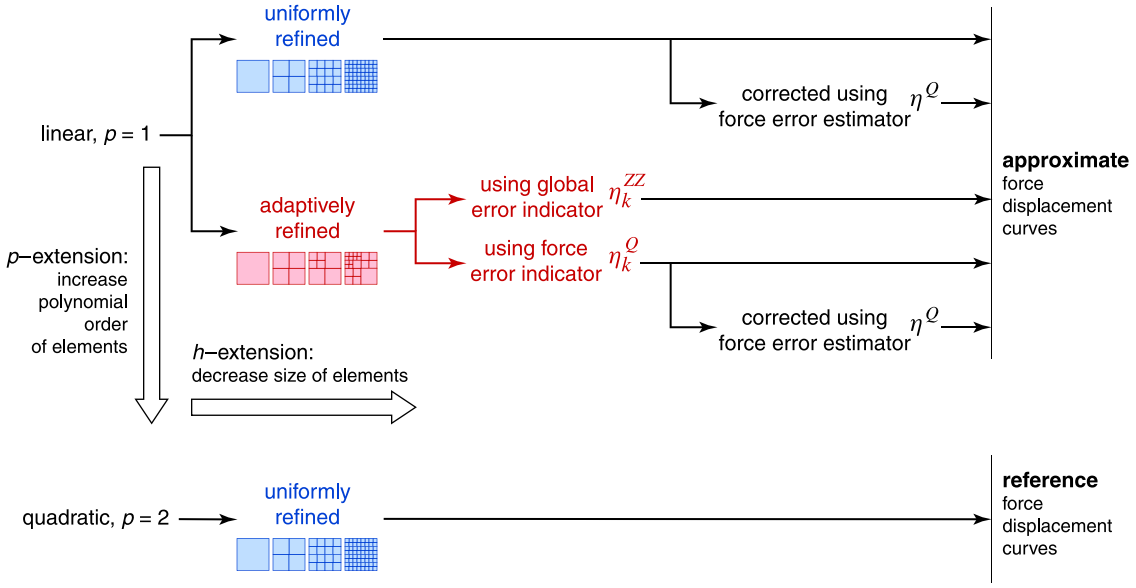


**Figure 3.25.** Possible paths used to compute approximate and reference force-displacement curves.

3.1199e-02 $\mu$N, with Aria evaluations requiring, on average, 388 seconds. Using the error correction on a linear mesh with only 800 elements yields an error of 7.6341e-02 $\mu$N, with evaluations averaging 35 seconds, less than 10% of the cost. The linear elements converge at approximately second order, while the error-corrected linear elements and quadratic elements converge at approximately fourth order.

The use of quadratic elements can result in more accurate solutions without drastic increase in computational expense. Figure 3.28 includes CDFs generated for three meshes with quadratic elements. While visually indistinguishable, the $L^2$ errors reported in Table 3.4 reveal rapid convergence as the mesh is uniformly refined (h-refinement), with, e.g., $L^2$ error 3.5667e-04 $\mu$N for an 800 element mesh. A comparison of average computation times reveals that a specified error tolerance can likely be achieved more efficiently through the use of quadratic rather than linear basis functions.

Using linear elements in conjunction with the quantity of interest error estimator $\eta^Q$ to correct the force output yields results comparable to the reference quadratic mesh. In Figures 3.29 and 3.30, CDFs are shown for two coarse (200 and 800 element) and two fine (3200 and 12800 element) meshes, respectively. The solid lines denote linear element solutions without error correction, and dashed lines indicate the corresponding quantity of interest ($\eta^Q$) corrected solutions. It is evident that the CDFs result from 800 linear element error-corrected simulations and the reference (3200 quadratic elements) simulations are quite similar. The error-corrected coarse mesh achieves this agreement at less than 8% of the cost per Aria simulation (Table 3.4). Since the

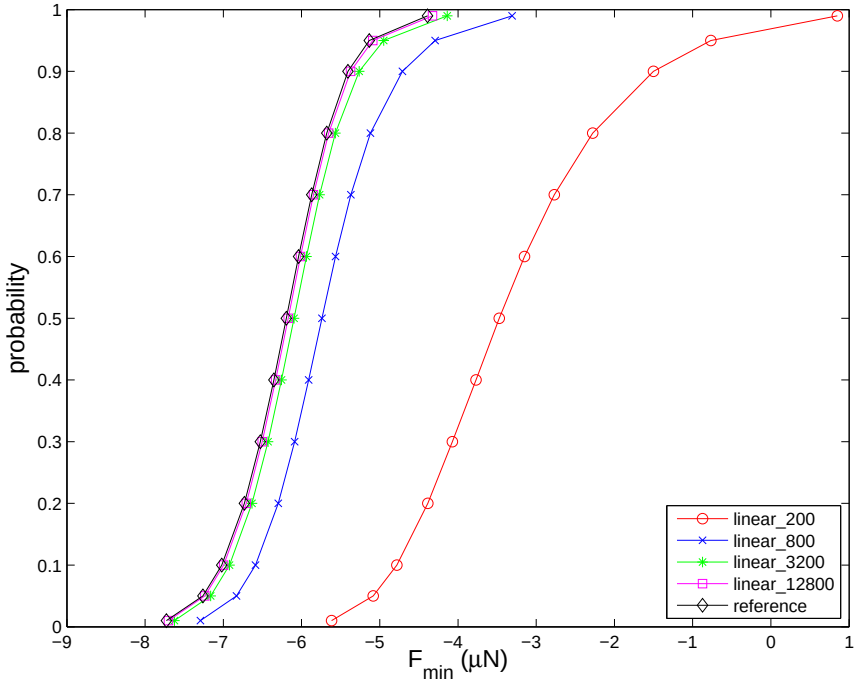


**Figure 3.26.** CDFs generated using AMV$^2$+ PMA with reference mesh (3200 quadratic elements) and 200, 800, 3200, and 12800 linear element meshes to demonstrate convergence under uniform refinement.

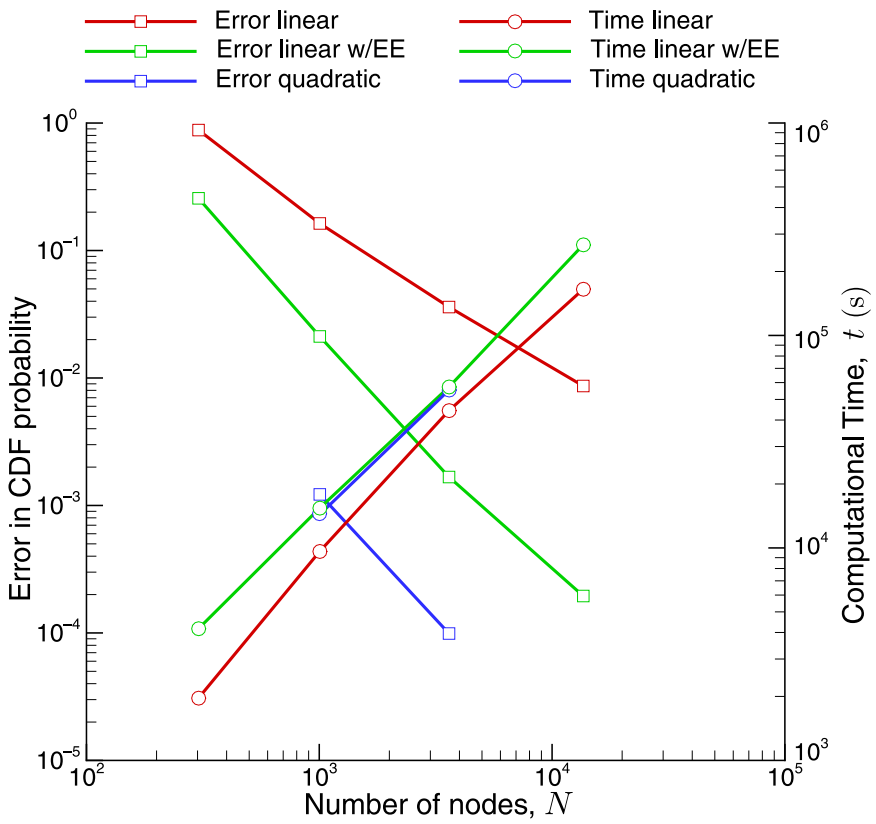


**Figure 3.27.** Plots of CDF error versus nodes using AMV$^2$+ from Table 3.4. Error rates for linear elements are second order, and for error–corrected linear and quadratic elements, the rates are fourth order.

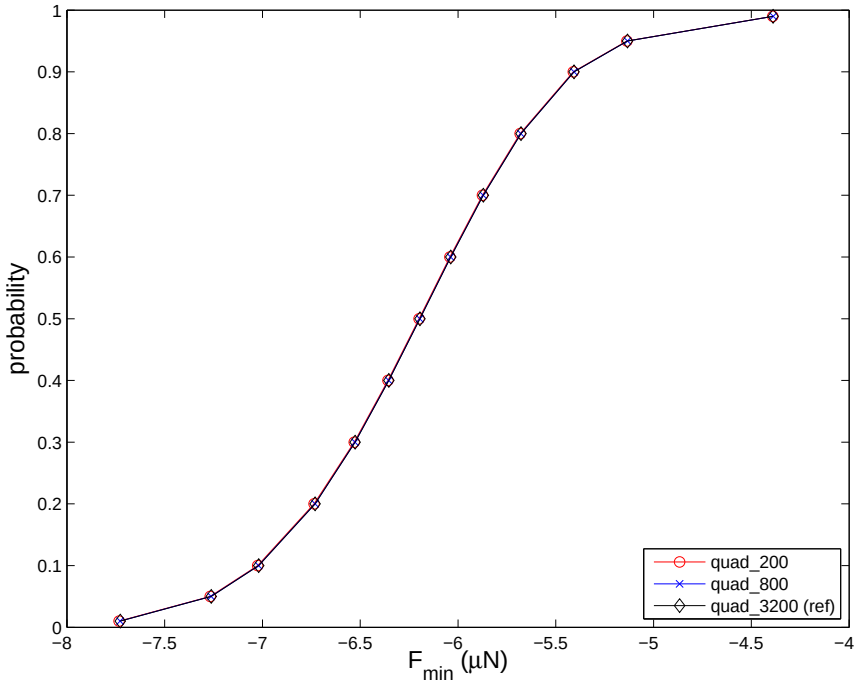


**Figure 3.28.** CDFs generated using AMV$^2$+ PMA with quadratic element meshes (200, 800, and 3200 elements).

**Table 3.4.** Computational cost and error for 13 point CDF generated with various methods and meshes. Time per evaluation is time per Aria solve, averaged across all evaluations. $L^2$ error relative to reference mesh is computed by (3.1).

| FEA type | UQ method | num. elts. | num. nodes | func. evals | time per eval (sec) | $L^2$ error in $z = F_{min}$ |
|---|---|---|---|---|---|---|
| linear | AMV$^2$+ | 200 | 303 | 340 | 5.7767 | 3.1758e+00 |
| linear w/EE | AMV$^2$+ | 200 | 303 | 485 | 8.5953 | 9.2555e-01 |
| linear | AMV$^2$+ | 800 | 1005 | 410 | 23.4885 | 5.8753e-01 |
| linear w/EE | AMV$^2$+ | 800 | 1005 | 445 | 34.6055 | 7.6341e-02 |
| linear | AMV$^2$+ | 3200 | 3609 | 475 | 93.2751 | 1.2985e-01 |
| linear w/EE | AMV$^2$+ | 3200 | 3609 | 420 | 136.2651 | 6.0263e-03 |
| linear | AMV$^2$+ | 12800 | 13617 | 425 | 388.3487 | 3.1199e-02 |
| linear w/EE | AMV$^2$+ | 12800 | 13617 | 470 | 568.3060 | 7.0266e-04 |
| quadratic | AMV$^2$+ | 200 | 1005 | 505 | 28.4588 | 4.4020e-03 |
| quadratic | AMV$^2$+ | 800 | 3609 | 475 | 116.6080 | 3.5667e-04 |
| quadratic | AMV$^2$+ | 3200 | 13617 | 360 | 477.8220 | |
| quadratic | LHS | 3200 | 13617 | 1000 | 482.5398 | |
| quadratic | RIA | 3200 | 13617 | 500 | 481.3034 | |
| quadratic | RIA 2$^{nd}$ QH | 3200 | 13617 | 460 | 482.0395 | |
| quadratic | RIA 2$^{nd}$ FDH | 3200 | 13617 | 1976 | 480.4406 | |

inclusion of adjoint error estimation calculations only adds 46–49% to the nominal per-simulation cost, a quantitatively-predictive error correction on a coarse mesh significantly outperforms a fully-converged fine mesh (which can be orders of magnitude more expensive).

Comparing refinement to error-correction strictly with linear elements, the 800 element linear mesh with error correction costs 35 seconds of CPU time, yet has CDF error (7.63e-02) that is consistent with a refined mesh without error correction consisting of somewhere in-between 3200 linear elements (error of 1.30e-01, costing 93 seconds) and 12800 linear elements (error of 3.12e-02, costing 388 seconds). In the linear basis cases considered, using error correction has similar effect to quadrupling the number of elements through uniform refinement, but at substantially less cost.

Error estimates are not always quantitatively predictive for insufficiently refined meshes. The 200 linear element results (with and without error correction, Figure 3.29) demonstrate that a level of mesh convergence is still required for the error estimate $\eta^Q$ to be predictive. Nonetheless, the level of mesh convergence required with error estimates is much lower than without.

In Figure 3.31, CDFs generated with PMA are compared to those generated with RIA using first-order probability integrations (denoted RIA AMV$^2$+) and second-order

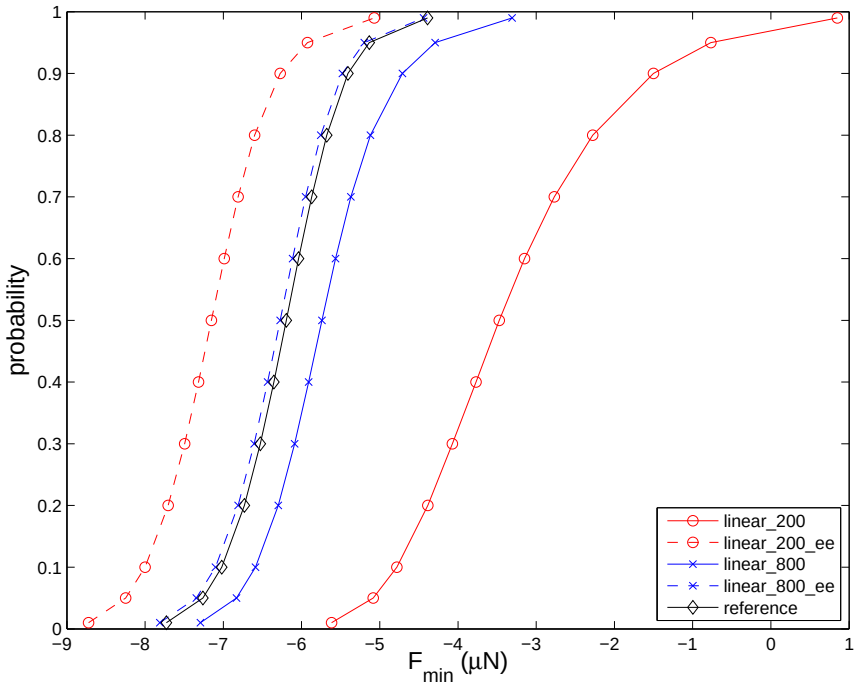


**Figure 3.29.** CDFs generated using AMV$^2$+ PMA with reference mesh (3200 quadratic elements) and two coarse linear element meshes, with and without quantity of interest error-correction. Note that the 800 linear element mesh performs similarly to the reference mesh.

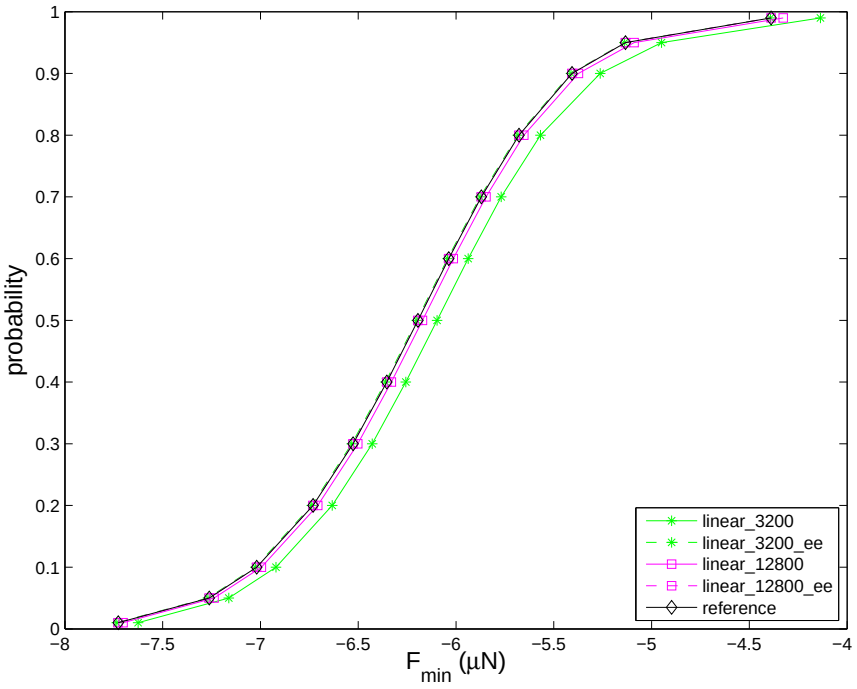


**Figure 3.30.** CDFs generated using AMV$^2$+ PMA with reference mesh (3200 quadratic elements) and two fine linear element meshes, with and without quantity of interest error-correction. Note that the 800 linear element mesh performs similarly to the reference mesh.

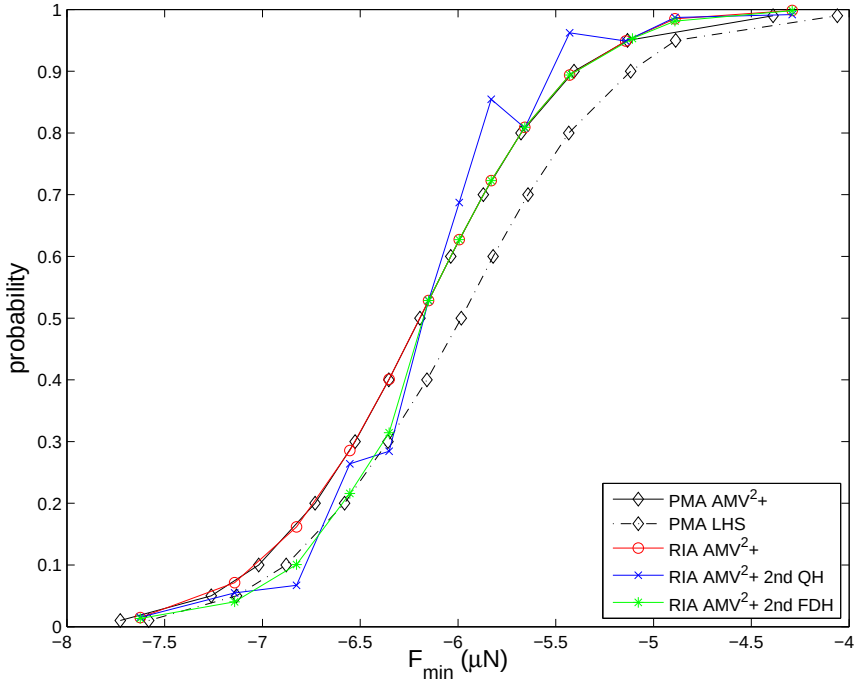


**Figure 3.31.** CDFs generated with reference mesh (3200 quadratic elements) using AMV$^2$+ PMA reliability method, LHS sampling method with 1000 samples, and AMV$^2$+ RIA reliability methods using first and second order integrations (latter with both SR1 quasi-Hessians (QH) and full finite difference Hessians (FDH).

probability integrations using SR1 quasi-Hessians and full finite difference Hessians (denoted RIA AMV$^2$+ 2nd QH and 2nd FDH, respectively) within the Hohenbichler-Rackwitz correction of (2.70). When using first-order integrations, the CDFs computed with PMA and RIA formulations agree. Second order probability integrations can better capture nonlinearity in limit states (such nonlinearity has been observed for this MEMS application) and yield more accurate estimates of probabilities (at least locally) at converged MPPs. It is evident that there is substantial curvature to the limit state, since the CDFs generated with RIA using second-order probability integrations have significant differences from the first-order results. The CDF generated using SR1 quasi-Hessians appears noisy. Changing to full finite difference Hessians (at quadruple the computational cost) smooths the second-order results. For the left tail of the CDF, the second-order probabilities are in good agreement with the LHS solution, created using 1000 samples of the uncertain variables. For the right tail, the principal curvatures are large and negative, causing numerical issues with the square root in (2.70) which result in the algorithm resorting back to the first-order probability integration for the problematic levels.

As described in Section 2.2.6, error estimates (global or quantity of interest) can also be used to drive mesh adaptivity. Figures 3.32 and 3.33 depict CDFs generated with adaptivity driven by global error ($\eta^{ZZ}$) estimation and quantity of interest error ($\eta^{Q}$) estimation, respectively. The computational cost and CDF errors for these simulations is shown in Table 3.5. While the 200 linear element CDF in Figure 3.32 is improved over that in Figure 3.26, it is evident that the discretization errors are still significant and that the convergence behavior of the PMA reliability analysis has been adversely affected. The $\eta^{Q}$ error estimator, which directly controls error in force (the quantity of interest), proved a much more effective control for mesh adaptivity. Not only do these error estimates allow more tailored mesh refinements, they also allow the use of error corrections which are not possible with global error estimates. Whereas both adapted but uncorrected CDFs in Figure 3.33 still exhibit some convergence difficulties, the adapted and corrected CDFs converge more reliably and efficiently. The total number of function evaluations needed in the error-corrected cases was 16–24% less than in the non-error-corrected cases and the resulting $L^2$ errors are 1–2 orders of magnitude smaller when correcting the force. The observed improvement in convergence behavior with error correction stems from the numerical finite differencing in the presence of changing meshes. When a small parameter offset results in a differently adapted mesh, the numerical gradient can be corrupted by the discontinuity in discretization level. This is mitigated to some degree by the use of error-correction, since the corrections can self-compensate for differing meshes (i.e., the same convergence enhancements observed under uniform refinement apply to differencing simulation results across dissimilarly adapted meshes).

**Table 3.5.** Computational cost and error for 13 point CDF generated with AMV$^2$+ PMA on various adaptive meshes using linear elements. Time per evaluation is time per Aria solve, averaged across all evaluations. $L^2$ error relative to reference mesh is computed by (3.1).

| adaptivity type | method | initial num. elts. | func. evals | time per eval (sec) | $L^2$ error in $z = F_{min}$ |
|---|---|---|---|---|---|
| $\eta^{ZZ}$ | AMV$^2$+ | 200 | 930 | 53.7512 | 5.4032e-01 |
| $\eta^{Q}$ | AMV$^2$+ | 200 | 1005 | 330.0198 | 9.6689e-01 |
| $\eta^{Q}$ | AMV$^2$+ w/EE | 200 | 845 | 329.8274 | 1.3126e-01 |
| $\eta^{Q}$ | AMV$^2$+ | 800 | 1235 | 286.4653 | 3.8277e-01 |
| $\eta^{Q}$ | AMV$^2$+ w/EE | 800 | 940 | 285.7942 | 3.3628e-02 |

Finally, we investigate the interactions between numerical gradient accuracy and the mesh adaptivity process. We plot the central differences obtained at the point

$$(\Delta W, S_r) = (-1.6921634025e{-}01, -2.0475471758e{+}01)$$

using a relative step size of 0.1%. We see in Figure 3.34 that as the refinement tolerance $QTOL$ goes to zero, the finite differences converge to the values of the

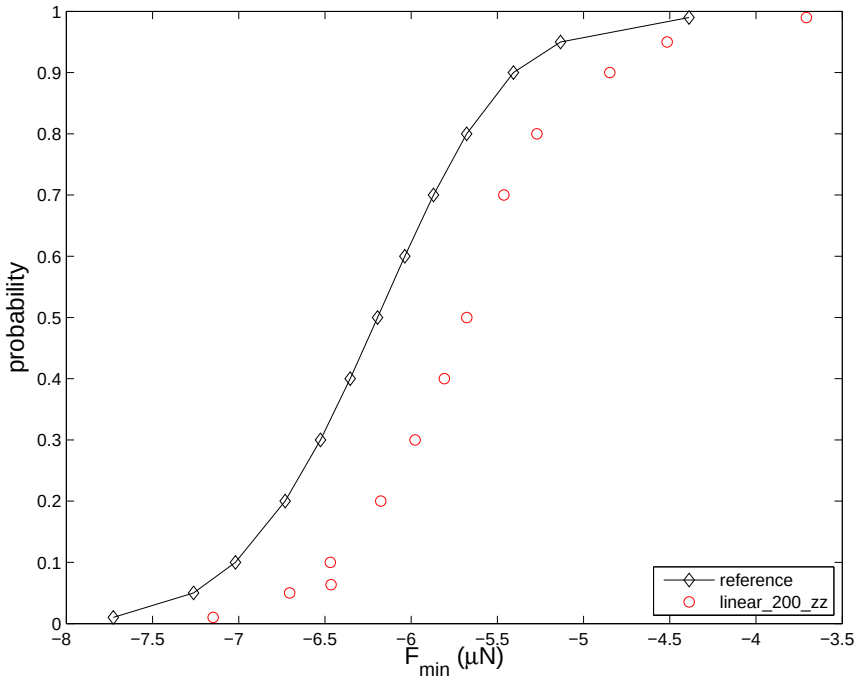


**Figure 3.32.** CDFs generated using AMV$^2$+ PMA with reference mesh (3200 quadratic elements) and $\eta^{ZZ}$-adaptive mesh with 200 initial linear elements.

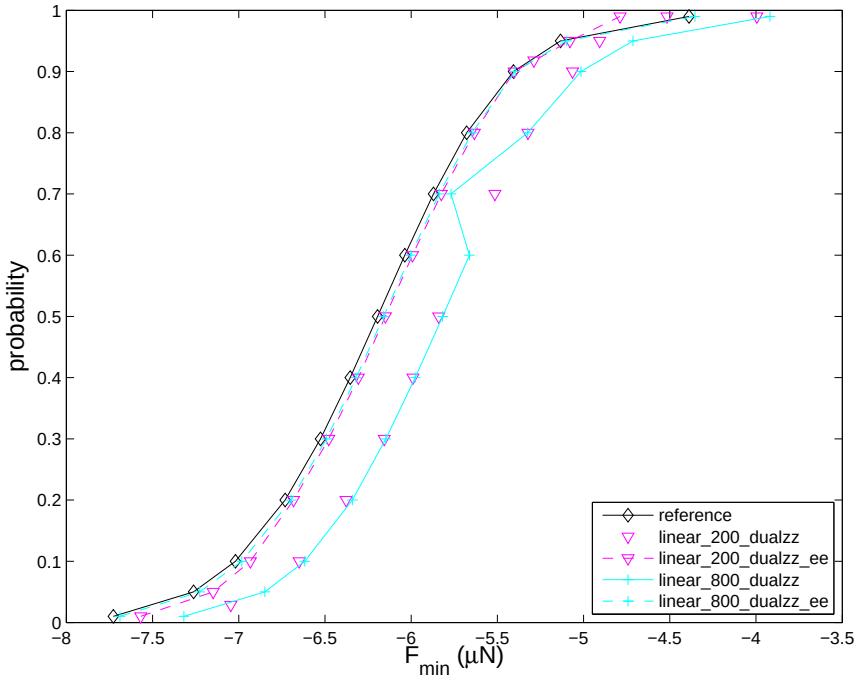


**Figure 3.33.** CDFs generated using AMV$^2$+ PMA with reference mesh (3200 quadratic elements) and $\eta^Q$-adaptive meshes with 200 and 800 initial linear elements meshes, with and without error correction in force.

reference solution (at $QTOL = 0$). However, the finite differencing may fail to be robust, as is seen when $QTOL = 0.5$. This is believed to occur when the mesh is changing locally due to adaptivity, causing a change in the minimum force that are greater than the change expected from the finite differencing using the reference solution. This leads to a recommendation for stricter control of mesh adaptivity in the presence of numerical finite differencing, as described in Section 4.2.

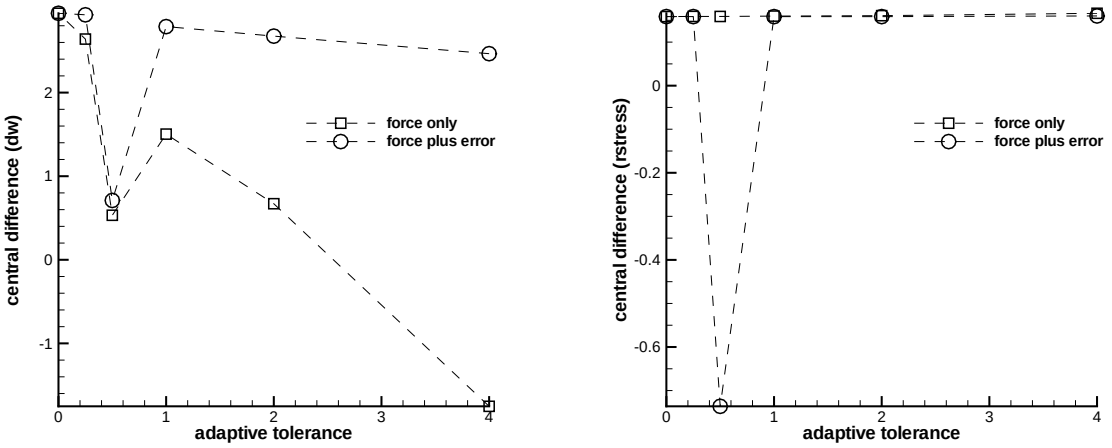


(a) width

(b) residual stress

**Figure 3.34.** Central finite differences for surface force and adaptivity using $\eta^Q$

## 3.5 Probabilistic Design Results

Given the 13 geometric design variables

$$\mathbf{d} = [L_1, L_2, L_3, L_4, \theta_1, \theta_2, \theta_3, \theta_4, W_0, W_1, W_2, W_3, W_4]$$

(described in Section 3.1 and subject to the bound constraints listed in Table 3.6) and the specified uncertain variables $\mathbf{x} = [\Delta W, S_r]$, we formulate a reliability-based design optimization problem to achieve a design that actuates reliably with at least 5 $\mu$N force. The RBDO formulation is uses the limit state

$$g(\mathbf{x}) = F_{min}(\mathbf{x}) \tag{3.2}$$

and failure is defined to be actuation force with magnitude less than 5.0 $\mu$N ($F_{min} > -5.0$). Reliability index $\beta_{ccdf} \geq 2$ is required. The RBDO problem utilizes the RIA $\bar{z} \rightarrow \beta$ approach (2.75) with $\bar{z} = -5.0$:

$$\begin{array}{lrcccl} \max & & & \mathrm{E}\left[F_{min}(\mathbf{d},\mathbf{x})\right] & & \\ \text{s.t.} & 2 & \leq & \beta_{ccdf}(\mathbf{d}) & & \\ & 50 & \leq & \mathrm{E}\left[F_{max}(\mathbf{d},\mathbf{x})\right] & \leq & 150 \\ & & & \mathrm{E}\left[E_2(\mathbf{d},\mathbf{x})\right] & \leq & 8 \end{array} \tag{3.3}$$

although the PMA $\bar{\beta} \rightarrow z$ approach (2.76) could also be used. The use of the $F_{min}$ metric in both the objective function and the reliability constraint results in a powerful problem formulation, because in addition to yielding a design with specified reliability, it also produces a robust design. By forcing the expected value of $F_{min}$ toward the $-5.0$ target while requiring two standard deviations of surety, the optimization problem favors designs with less variability in $F_{min}$. This renders the design performance less sensitive to uncertainties. The response PDF control is depicted in Figure 3.35, where the mean is maximized subject to a reliability constraint on the right tail. Alternatively, the response PDF control depicted in Figure 3.36 could be employed by maximizing the PMA $z$ level corresponding to $\bar{\beta} = -2$. This has the advantage of controlling both sides of the response PDF, but it is more computationally expensive since it requires the solution of two MPP optimization problems per design cycle instead of one. For this reason, the RIA RBDO formulation in (3.3) is used for all results in this section.

The optimization problem is solved by applying the DAKOTA software in the bi-level (nested) RBDO approach of Section 2.4.1. Design variable optimization is performed with the DOT optimizer using the modified method of feasible directions (MMFD) [65] and, for each design iterate, a complete uncertainty analysis is performed with DAKOTA's reliability methods. For this optimization, each RIA analysis is performed using AMV$^2$+ approximations with SR1 quasi-Hessians to solve the MPP optimization subproblems. This method is advantaged by its ability to provide (semi-)analytic derivatives of reliability metrics with respect to design variables for the optimizer. That is, while the derivatives of the simulation response functions

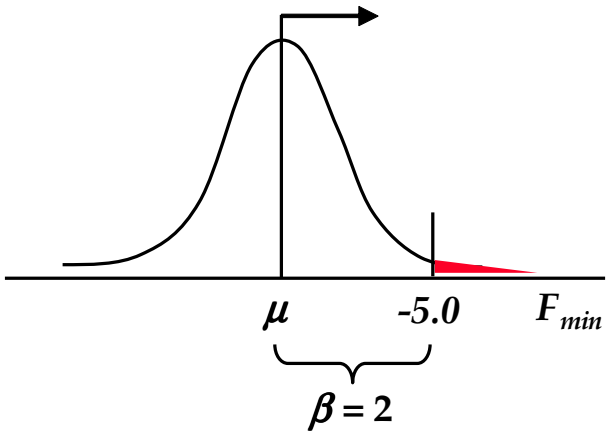


**Figure 3.35.** Response PDF control of mean and right tail.

(e.g., $F_{min}$) must be evaluated numerically, the derivatives of the reliability metrics are defined as analytic functions of these simulation response function derivatives (see Section 2.4.1). Since a primary goal of the present work is to evaluate the effect of mesh choice and error estimation on reliability analysis, the initial iterate for the gradient-based MMFD is taken to be an optimal design point from Adams, et al. [1]. Optimization is performed for various discretizations and error corrections, each using the same initial iterate. When needed, gradients of the simulation response functions with respect to the uncertain variables $\mathbf{x}$ or design variables $\mathbf{d}$ are computed using central differences with a 0.1% relative step size.

Table 3.6 contains optimal RBDO designs corresponding to the coarse (800 element) linear mesh, with and without $\eta^Q$ error correction, the finest (12800 element) linear mesh, and the reference quadratic mesh. In all except the reference mesh case, the optimizer progresses to an optimal solution where the reliability constraint $\beta$ is active and the expected value of $F_{min}$ is maximized. The optimizer progresses when using the reference mesh, but does not yield as good a value for $F_{min}$, nor as tight a constraint on the reliability metric $\beta$.

For all meshes considered, reliability-based design optimization finds device designs more robust to input uncertainties by the means depicted in Figure 3.35. The initial bistable MEMS design reported in Adams, et al. [1], had variability in $F_{min}$ of 5.6 $\mu N$ per input standard deviation, calculated as $\frac{\mathrm{E}[F_{min}]-\bar{F}_{min}}{\beta}$. As shown in Table 3.6, the optimal designs found with the present methods have variability 0.59–0.62 $\mu N$ per input standard deviation, indicating less sensitivity to input uncertainties.

As with CDF generation in Section 3.4, the error-corrected coarse mesh requires fewer iterations to converge than that without error correction, with modest per-simulation cost increase. The error-corrected 800 element coarse mesh yields a similar solution

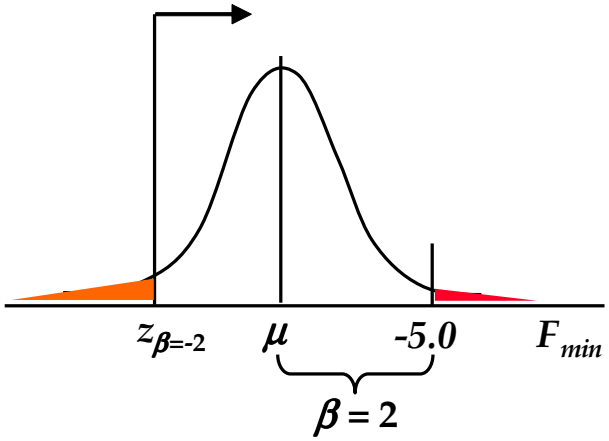


**Figure 3.36.** Response PDF control of both tails.

to the 12800 element fine mesh, but at less than 10% of the total computational cost (27 versus 373 compute hours).

Figure 3.37 depicts the force–displacement curves for the optimal designs resulting from each linear mesh. The lower panel zooms in on the area near the minimum and demonstrates the quadratic interpolation used to accurately locate the displacement, minimum force pair. There is good agreement between the refined linear solution and the $\eta^Q$ error-corrected coarse solution.

Figure 3.38 shows curves generated using the reference mesh for each of the optimal design parameter sets from Table 3.6. These "reference-verified" force-displacement curves further confirm that RBDO using the 800 linear element mesh, with $\eta^Q$ error-correction, yields an optimal design similar to the finest (12800 element) mesh. Moreover, the difference between curves in Figures 3.37 and 3.38 corresponding to the 800 linear element uncorrected case suggests caution when performing RBDO with insufficiently refined meshes.

**Table 3.6.** RBDO results for MEMS bistable mechanism: design variable bounds and optimal designs resulting from analysis with four meshes using AMV$^2$+.

| variable or metric | | | initial | optimal | | | |
|---|---|---|---|---|---|---|---|
| | | | quadratic | linear | linear | linear | quadratic |
| l.b. | name | u.b. | 3200 | 800 | 800 w/EE | 12800 | 3200 |
| 10 | $L_1\,(\mu m)$ | 35 | 28.06 | 28.33 | 28.07 | 28.04 | 28.08 |
| 10 | $L_2\,(\mu m)$ | 35 | 24.50 | 24.61 | 24.44 | 24.42 | 24.47 |
| 10 | $L_3\,(\mu m)$ | 35 | 30.83 | 31.05 | 30.63 | 30.59 | 30.72 |
| 10 | $L_4\,(\mu m)$ | 35 | 30.83 | 31.08 | 30.61 | 30.56 | 30.70 |
| 0 | $\theta_1$ (deg.) | 5 | 4.167 | 4.170 | 4.195 | 4.198 | 4.184 |
| 0 | $\theta_2$ (deg.) | 5 | 2.500 | 2.514 | 2.485 | 2.482 | 2.491 |
| 0 | $\theta_3$ (deg.) | 5 | 2.500 | 2.523 | 2.472 | 2.467 | 2.484 |
| 0 | $\theta_4$ (deg.) | 5 | 2.400 | 2.410 | 2.387 | 2.385 | 2.393 |
| 1 | $W_0\,(\mu m)$ | 3 | 1.333 | 1.313 | 1.349 | 1.354 | 1.342 |
| 1 | $W_1\,(\mu m)$ | 3 | 1.253 | 1.233 | 1.268 | 1.273 | 1.260 |
| 2 | $W_2\,(\mu m)$ | 5 | 3.500 | 3.505 | 3.485 | 3.482 | 3.491 |
| 1 | $W_3\,(\mu m)$ | 3 | 2.000 | 1.993 | 2.005 | 2.006 | 2.004 |
| 1 | $W_4\,(\mu m)$ | 3 | 1.333 | 1.327 | 1.334 | 1.333 | 1.334 |
| | $\mathrm{E}\,[F_{min}]\ (\mu N)$ | | -6.645 | -6.208 | -6.231 | -6.188 | -6.288 |
| 2 | $\beta$ | | 2.172 | 1.998 | 1.998 | 2.002 | 2.094 |
| 50 | $\mathrm{E}\,[F_{max}]\ (\mu N)$ | 150 | 57.05 | 59.19 | 57.65 | 57.87 | 57.11 |
| | $\mathrm{E}\,[E_2]\ (\mu m)$ | 8 | 6.019 | 6.156 | 6.002 | 5.996 | 6.021 |
| var. in $F_{min}$ per $\beta$ | | | 0.76 | 0.60 | 0.62 | 0.59 | 0.62 |
| num. func. evals. | | | - | 3581 | 2822 | 3149 | 1750 |
| avg. time/eval (sec) | | | - | 24.0552 | 34.4634 | 425.8951 | 479.9207 |

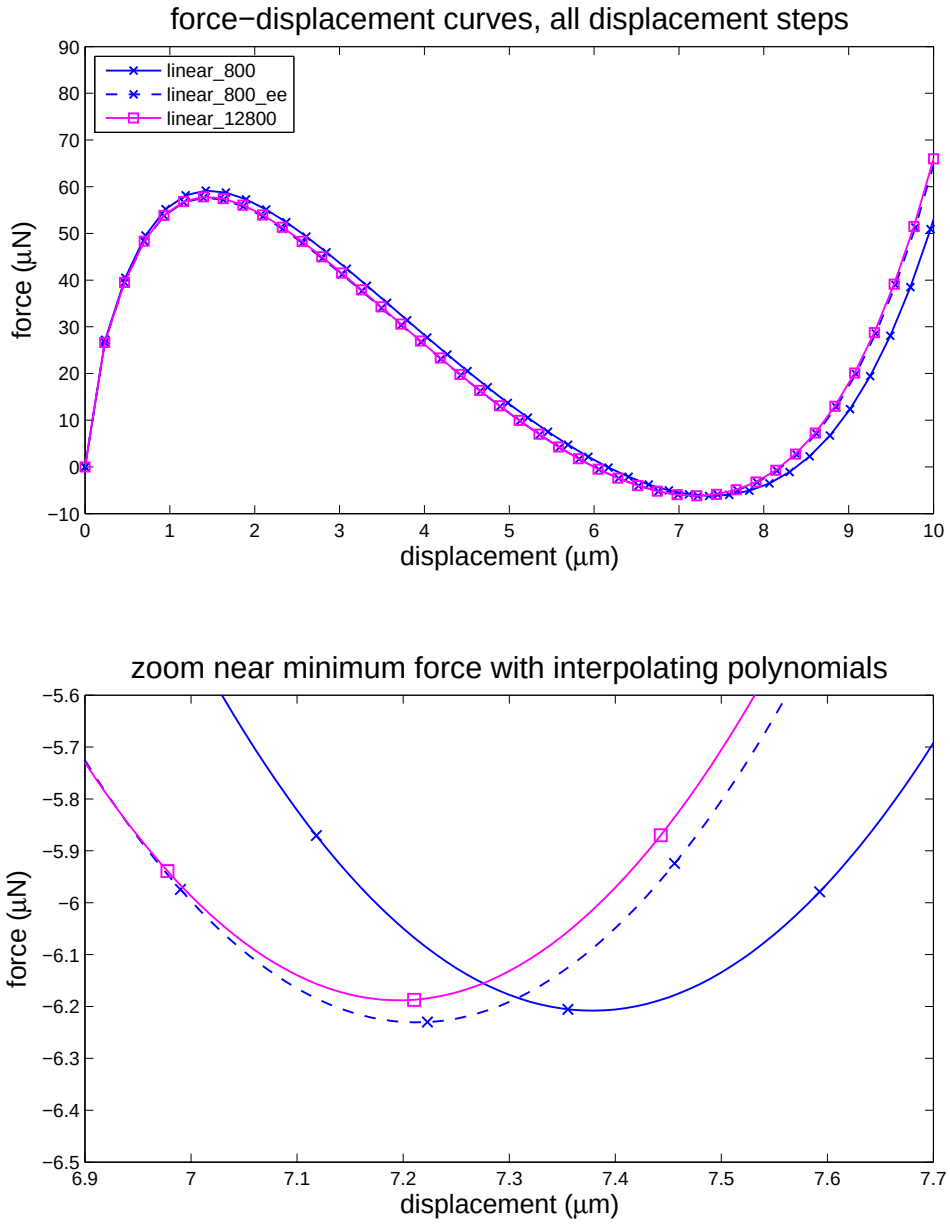


**Figure 3.37.** Optimal force–displacement curves resulting from RBDO with various meshes.

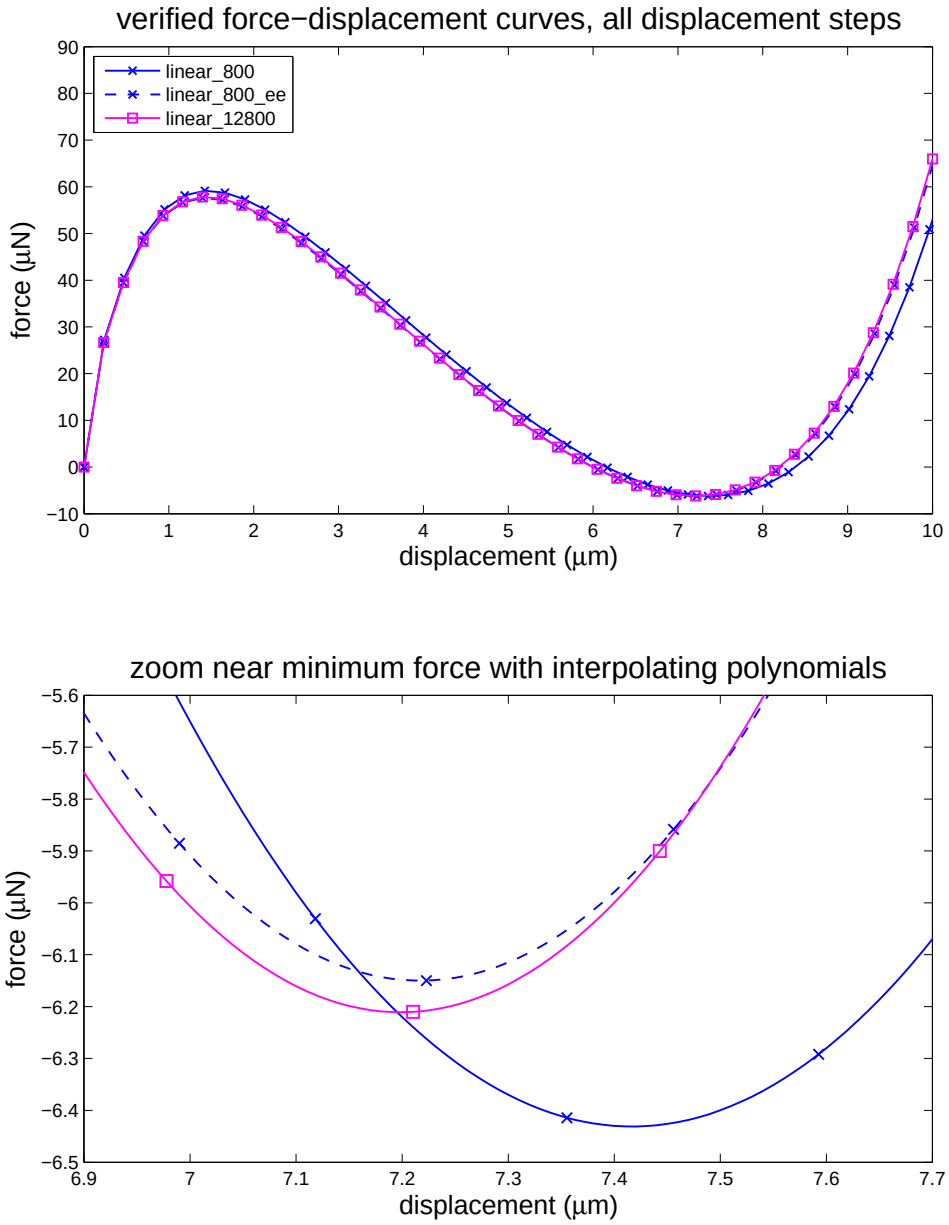


**Figure 3.38.** Verified force–displacement curves generated using reference mesh (3200 quadratic elements) with optimal geometries resulting from RBDO with various meshes.

# Chapter 4

# Accomplishments and Conclusions

This report explores the deployment of reliability analysis and error estimation capabilities to probabilistic analysis and design of microelectromechanical systems (MEMS). An error estimator is developed for the error in the surface force in finite element approximations of nonlinear elasticity models. Numerical results verify that the estimator produces accurate error estimates using both uniform and adaptively refined meshes. Error-corrected and error-controlled reliability analysis using the estimator are applied to address solution verification in an automated, on-line manner. Any dependence of solution discretization errors on random or design variables, which can occur particularly when varying geometric shape parameters, is captured. The most effective and affordable of these approaches are carried forward in probabilistic design studies for robust and reliable operation of a bistable MEMS device.

The key milestone conclusion is that on-line solution verification approaches show significant promise. In terms of accuracy, controlling or correcting for errors (or both) leads to higher confidence in the uncertainty analysis and probabilistic design recommendations. In terms of computational expense, the use of error-correction on coarse meshes (from adjoint-based quantity of interest error estimates) was shown to result in less than 10% of the simulation expense of fully converged meshes with comparable accuracy. In terms of computational reliability, the ability of the on-line approach to be parameter-adaptive precludes the possibility of using model results that are converged for one set of parameters, but not for another. And in terms of convenience, the potential elimination of the need for manual convergence studies should significantly reduce overhead for analysts and designers.

Table 4.1 summarizes these characteristics for different approaches to solution verification within UQ/RBDO studies, including no solution verification, off-line solution verification at the simulation level (e.g., Figure 3.7), off-line solution verification at the UQ/RBDO study level (e.g., Figure 3.26), and on-line solution verification using error estimation and adaptivity. Of these possibilities, the no verification and simulation-level off-line approaches are believed to be the two most common practices at this time. The on-line approaches are clearly the most desirable, but are obtained at the price of additional simulation development to support error estimation and adaptivity.

| | no verification | simulation-level off-line | study-level off-line | on-line EE/Adapt |
|---|---|---|---|---|
| Accuracy | L | M | H | H |
| Efficiency | H | M | L | H |
| Reliability | L | M | H | H |
| Convenience | H | M | L | H |

**Table 4.1.** Comparison of solution verification strategies: H = high, M = medium, L = low

## 4.1 Observations on error estimation and adaptivity

Individual observations for error estimation and adaptivity include:

- The surface force computed by Aria on sequences of *uniform* meshes of linear or quadratic elements converges at the formal rate $O(h^{2\,p}) = O(N^{-p})$, where $h$ is element size, $N$ is the number of nodes, and $p = 1, 2$ is the polynomial degree. The surface force computed by Aria on *adaptive* sequences of meshes of linear elements ($p = 1$) converges at $O(N^{-1})$ which agrees with the observed rate for *uniform* refinement. This is expected behavior for this particular problem geometry and set of boundary conditions, because the input data is smooth, resulting in a relatively smooth solution. For more complex input data, e.g., re-entrant corners, nonsmooth boundary conditions, or material interfaces, adaptivity would be expected to provide a similar rate of convergence, while uniform meshes would have a lower order of convergence.

- The *a posteriori* estimator for the quantity of interest is sufficiently accurate for the bistable MEMS problem. On the specific sets of meshes used in this study, the ratio of the estimated to the exact error (effectivity) fell in the range $[0.7, 1.4]$ on uniform meshes, and $[0.65, 0.95]$ on adaptive meshes. The accuracy of the estimator, measured by the effectivity, appeared to increase as the meshes were refined.

- The computational cost of the quantity of interest error estimator is relatively small in the bistable MEMS problem, due to the relatively small problem size (less than 20,000 elements) and the use of a direct solver. In the formulation used in the milestone, the linearized adjoint problem is solved using the same matrix as the primal problem (which, with a proper implementation, may be formulated as solving an extra right hand side of the linearized primal problem), and the gradient recovery scales as $O(N)$. For large scale problems (greater than 100,000 elements), the cost of the adjoint solve will grow with the linear solve

for the displacement. However, in a nonlinear problem such as this, the cost will be the same as an additional nonlinear iteration. The cost of the adjoint solve can be reduced through the use of an iterative solver with a looser tolerance or re-use of the preconditioner from the last linear solve for the displacements.

- The adaptive meshes based on the quantity of interest indicator generally exhibit smaller errors for the same number of nodes versus the meshes generated using the global indicator. The quantity of interest indicator produced more local mesh refinement near the surface of interest, while the global indicator tended to produce more uniform patches of elements. The advantage of the quantity of interest estimator would be stronger in more complicated boundary value problems.

- The sum of the surface force and the quantity of interest error estimate was always more accurate than the force itself, and this sum converged at a faster rate for both uniform and adaptive sequences of meshes.

- In this milestone, the quadratic elements provided a means to an inexpensive "overkill," or reference solution. This is a result of the fact that, for sufficiently smooth problems, elements of higher polynomial order than linear converge much more quickly to the exact solution.

## 4.2 Observations on UQ and RBDO

Individual observations for uncertainty quantification and probabilistic design include:

- Discretization errors were demonstrated to have a significant parameter dependence with respect to both the design and uncertain variables for this MEMS application. While one might assume that discretization error would primarily be a function of mesh density, it has been shown to also be a strong function of the internal states of the simulation. This makes a strong case for parameter adaptive approaches to solution verification for use within uncertainty and design studies.

- Our probabilistic design results satisfied the prescribed reliability ($\beta \geq 2$) and improved robustness with respect to the modeled uncertainties (reducing variability in force from 5.6 $\mu N$ per input standard deviation in the initial design to 0.59–0.62 in the final designs). However, additional uncertainties should be included in future studies to prevent a lack of robustness with respect to other shape and material variabilities. In particular, width bias should be augmented to include manufacturing uncertainties in lengths and angles (the other design variables), and small symmetry imperfections (requiring a full switch model) could have a significant effect on buckling performance.

- Reliability analysis and design methods are a good match for applications involving MEMS. For the physics studied to date, simulation results have been smooth and gradients of response metrics with respect to design and uncertain parameters have been reliable, so long as mesh changes while finite differencing are not large. Nongradient-based approaches for optimization or UQ would have been significantly more expensive.

- Our shape optimization approach regenerated structured meshes for each new set of shape parameters using FASTQ. Future enhancements will focus on smooth mesh movement using tools such as DDRIV and MESQUITE. This approach is distinct from topology optimization, which is a large-scale approach that designs the material density for every element in a computational domain.

- Numerical differencing for gradients requires tight control of mesh schedules employed during adaptive refinement procedures. For example, multiple Aria simulations are performed as a part of the finite–difference approximation to the derivative of $F_{min}$ with respect to a given design or uncertain parameter. The introduction of dynamic adaptivity means that these simulations may be performed for different mesh schedules due to the parameter change. It has been shown in this work that this may lead to inaccurate finite–difference approximations in some situations. A possible future remedy would be for Aria to re-use a previously generated adaptive mesh schedule while finite differencing, such that one can be assured of differencing simulation results across the same discretization. Support for analytic gradients would also address this issue.

- Second-order reliability analysis methods were more efficient and robust than standard first-order techniques. The Sandia-developed AMV$^2$+ method using SR1 Hessian updates was successful at converging to MPPs when the industry-standard AMV+ technique was not. Future work will extend AMV+ and AMV$^2$+ to use trust-region management of surrogate limit state models, which will further improve their robustness.

- Optimizers are highly proficient at locating weaknesses in a computational model and exploiting them in seeking designs which better satisfy the objective and constraints. The probability integration within a reliability analysis is such a weakness, since a first-order or partial second-order approximation to the limit state centered at the MPP can be an inaccurate representation of the true limit state and associated failure probability. In particular, a design problem with active reliability constraints will approach the failure domain as tightly as possible, and points where the failure region encircles the design (e.g., Figure 1.4b) will not have their reliability represented accurately by low-order approximations. While this situation may be relatively uncommon for uncertainty analysis by itself, we have found that it is much more prevalent for designs that are optimized for probabilistic performance. That is, standard integration approaches will often be fine for uncertainty analysis, but need to be "hardened" for use

in RBDO to prevent optimizer exploitation and resulting under-estimation of failure probabilities. Future work in this area is described in [14].

- The error-corrected approach was the most efficient for both UQ and RBDO. However, the possibility of having error-corrected results that are not yet converged (e.g., the linear 200 corrected case in Figure 3.29) is a concern. The combination of error-controlled and error-corrected approaches, while not as efficient as error-corrected alone, addresses this concern and provides a higher confidence in the UQ/RBDO results. Tuning the combination of error-control and error-correction for improved computational efficiency (e.g., by limiting adaptivity cycles) appears to be a fruitful direction.

- The use of error-corrected approaches to UQ and RBDO is related to the area of multifidelity surrogate-based optimization (SBO). In multifidelity SBO, correction factors are periodically computed using the difference between low and high fidelity models [29]. In the error-corrected UQ and RBDO approaches from this report, a single-fidelity approach is used where a low fidelity, unconverged model is continuously corrected based on error estimates to approximate fully-converged results. Since multifidelity SBO updates the correction factors infrequently in order to minimize use of the expensive high fidelity model, continuous correction factors from error estimation could accelerate the SBO process and remove the need for trust-region management.

- More robust determination of values and derivatives with respect to design parameters of key points of interest in the response function could improve performance and accuracy. Aria is capable of using the LOCA package [59] for automated parameter continuation, turning point tracking and sensitivity analysis. The LOCA package is capable of providing very accurate locations of stability turning points as well as tracking those turning points across variations of other design parameters ("turning point tracking and continuation"). Significant improvements in performance and accuracy would be possible if Aria would better expose the LOCA features to improve interoperability with DAKOTA.

## 4.3 Accomplishments and Capability Development

This milestone crosscuts multiple centers, with components including the uncertainty analysis and probabilistic design capabilities from DAKOTA (1400), global norm and quantity of interest error estimates from Coda (1500), nonlinear mechanics analysis from Aria (1500), data structures and $h$-refinement algorithms from SIERRA (1500), and MEMS model development and MESA program relevance (1700). New capabilities have been developed and tested within the codes by their respective teams for use in this milestone, including:

- nonlinear elasticity model for large displacements

- postprocessed reaction forces on domain boundaries
- mesh $h$-adaptivity with hanging nodes
- quantity of interest error estimator for reaction forces in nonlinear elastic problems
- capability to solve linearized adjoint approximation on same mesh
- least squares based gradient recovery and ZZ indicator
- adaptive control of surface force error in a transient nonlinear quasistatic problem – the capability to adapt the mesh to ensure the accuracy of the reaction force within a user specified tolerance
- capability to compute CDF using uncorrected and error corrected output on both uniform and adaptive meshes
- second-order surrogate-based reliability analysis and design methods and semi-analytic probabilistic design sensitivities in DAKOTA.

# References


[1] B. M. Adams, M. S. Eldred, and J. W. Wittwer. Reliability-based design optimization for shape design of compliant micro-electro-mechanical systems. In *Proceedings of the 11th AIAA/ISSMO Multidisciplinary Analysis and Optimization Conference*, number AIAA-2006-7000, Portsmouth, VA, September 6–8, 2006.

[2] H. Agarwal, J. E. Renaud, J. C. Lee, and L. T. Watson. A unilevel method for reliability based design optimization. In *Proceedings of the 45th AIAA/ASME/ASCE/AHS/ASC Structures, Structural Dynamics, and Materials Conference*, number AIAA-2004-2029, Palm Springs, CA, April 19–22, 2004.

[3] M. Ainsworth and J. T. Oden. *A Posteriori Error Estimation in Finite Element Analysis*. John Wiley and Sons, 2000.

[4] J. J. Allen. *Micro Electro Mechanical System Design*. Taylor and Francis, Boca Raton, 2005.

[5] M. Allen and K. Maute. Reliability-based design optimization of aeroelastic structures. *Struct. Multidiscip. O.*, 27:228–242, 2004.

[6] G. K. Ananthasuresh, S. Kota, and Y Gianchandani. A methodical approach to the design of compliant micromechanisms. In *Proc. IEEE Solid-State Sensor and Actuator Workshop*, pages 189–192, Hilton Head Island, SC, 1994.

[7] I. Babuška, J. Chandra, and J. E. Flaherty, editors. *Adaptive computational methods for partial differential equations*. SIAM, 1983.

[8] I .Babuška and A. Miller. Post-processing approach in the finite element method - part 1: Calculation of displacements, stresses and other higher derivatives of the displacements. *Int. J. Numer. Meth. Engrg*, 20(6):1085–1109, 1984.

[9] I. Babuška and A. Miller. Post-processing approach in the finite element method - part 3: A posteriori error estimates and adaptive mesh selection. *Int. J. Numer. Meth. Engrg*, 20(12):2311–2324, 1984.

[10] I. Babuška and W. C. Rheinboldt. Error estimates for adaptive finite element computations. *SIAM J. Numer. Anal.*, 15(4):736–754, 1978.

[11] I. Babuška and T. Strouboulis. *The finite element method and its reliability*. Oxford University Press, 2001.

[12] I .Babuška, O. C. Zienkiewicz, and J. Gago, editors. *Accuracy estimates and adaptive refinements in finite element computations*, Wiley Series in Numerical Methods in Engineering. John Wiley & Sons, 1984.

[13] R. Becker and R. Rannacher. A feed-back approach to error control in finite element methods: basic analysis and examples. *East-West J. Numer. Math.*, 4(4):237–264, 1996.

[14] B. J. Bichon, M. S. Eldred, L. P. Swiler, S. Mahadevan, and J. M. McFarland. Multimodal reliability assessment for complex engineering applications using efficient global optimization. In *abstract submitted for 9th AIAA Non-Deterministic Approaches Conference*, Honolulu, HI, April 23–26, 2007.

[15] G. E. P. Box and D. R Cox. An analysis of transformations. *J. Royal Stat. Soc.*, 26:211–252, 1964.

[16] K. Breitung. Asymptotic approximation for multinormal integrals. *J. Eng. Mech., ASCE*, 110(3):357–366, 1984.

[17] S. C. Brenner and L. R. Scott. *The Mathematical Theory of Finite Element Methods*. Springer, New York, 2nd edition, 2002.

[18] G. F. Carey. A mesh-refinement scheme for finite element computations. *Comput. Mech. App. Mech. Engrg.*, 17/18:541–560, 1976.

[19] G. F. Carey. *Computational grids: generation, adaptation, and solution strategies*. Taylor & Francis, 1997.

[20] X. Chen and N .C. Lind. Fast probability integration by three-parameter normal tail approximation. *Struct. Saf.*, 1:269–276, 1983.

[21] H. W. Coleman and W. G. Steele. *Experimentation and Uncertainty Analysis for Engineers*. Wiley, New York, 2nd edition, 1999.

[22] T. D.Blacker. FASTQ users manual, version 1.2. Technical Report SAND88-1326, Sandia National Laboratories, Albuquerque, NM, July 1998.

[23] A. Der Kiureghian and P. L. Liu. Structural reliability under incomplete probability information. *J. Eng. Mech., ASCE*, 112(1):85–104, 1986.

[24] X. Du and W. Chen. Sequential optimization and reliability assessment method for efficient probabilistic design. *J. Mech. Design*, 126:225–233, 2004.

[25] H. C. Edwards. Sierra framework for massively parallel adaptive multiphysics application. Technical Report SAND2004-6277C, Sandia National Laboratories, Albuquerque, NM, July 2005.

[26] M. S. Eldred, H. Agarwal, V. M. Perez, S. F. Wojtkiewicz, Jr., and J. E. Renaud. Investigation of reliability method formulations in DAKOTA/UQ. *Structure & Infrastructure Engineering: Maintenance, Management, Life-Cycle Design & Performance*. to appear.

[27] M. S. Eldred and B. J. Bichon. New second-order reliability formulations for reliability analysis and design. in preparation.

[28] M. S. Eldred and A. A. Giunta. Implementation of a trust region model management strategy in the DAKOTA optimization toolkit. In *Proceedings of the 8th AIAA/USAF/NASA/ISSMO Symposium on Multidisciplinary Analysis and Optimization*, number AIAA-2000-4935, Long Beach, CA, September 6–8, 2000.

[29] M. S. Eldred, A. A. Giunta, and S. S. Collis. Second-order corrections for surrogate-based optimization with model hierarchies. In *Proceedings of the 10th AIAA/ISSMO Multidisciplinary Analysis and Optimization Conference*, Albany, NY,, Aug. 30–Sept. 1, 2004. AIAA Paper 2004-4457.

[30] M. S. Eldred, A. A. Giunta, B. G. van Bloemen Waanders, S. F. Wojtkiewicz, Jr., W. E. Hart, and M. P. Alleva. DAKOTA, a multilevel parallel object-oriented framework for design optimization, parameter estimation, uncertainty quantification, and sensitivity analysis. version 3.1 users manual. Technical Report SAND2001-3796, Sandia National Laboratories, Albuquerque, NM, Revised April 2003.

[31] M. S. Eldred, A. A. Giunta, S. F. Wojtkiewicz Jr., and T. G. Trucano. Formulations for surrogate-based optimization under uncertainty. In *Proceedings of the 9th AIAA/ISSMO Symposium on Multidisciplinary Analysis and Optimization*, number AIAA-2002-5585, Atlanta, GA, September 4–6, 2002.

[32] K. Eriksson and C. Johnson. Adaptive methods for parabolic problems i: a linear model problem. *SIAM J. Numer. Anal.*, 1991.

[33] D. Estep. A posteriori error bounds and global error control for approximation of ordinary differential equations. *SIAM J. Numer. Anal.*, 32(1):1–21, 1995.

[34] D. Estep, M. Holst, and M. Larson. Generalized green's functions and the effective domain of influence. *SIAM J. Sci. Comput.*, 26(4):1314–1339, 2005.

[35] D. Estep, M. Holst, and D. Mikulencak. Accounting for stability: a posteriori error estimates based on residuals and variational analysis. *Comun. Numer. Meth. Engrg.*, 18(1):15–30, 2002.

[36] G. M. Fadel, M. F. Riley, and J.-F. M. Barthelemy. Two point exponential approximation method for structural optimization. *Structural Optimization*, 2(2):117–124, 1990.

[37] P. E. Gill, W. Murray, M. A. Saunders, and M. H. Wright. User's guide for npsol 5.0: A fortran package for nonlinear programming. Technical Report SOL 86-1, System Optimization Laboratory, Stanford University, Stanford, CA, Revised July 1998.

[38] A. Haldar and S. Mahadevan. *Probability, Reliability, and Statistical Methods in Engineering Design*. Wiley, New York, 2000.

[39] M. Hohenbichler and R. Rackwitz. Sensitivity and importance measures in structural reliability. *Civil Eng. Syst.*, 3:203–209, 1986.

[40] M. Hohenbichler and R. Rackwitz. Improvement of second-order reliability estimates by importance sampling. *J. Eng. Mech., ASCE*, 114(12):2195–2199, 1988.

[41] H. P. Hong. Simple approximations for improving second-order reliability estimates. *J. Eng. Mech., ASCE*, 125(5):592–595, 1999.

[42] B. D. Jensen, M. B. Parkinson, K. Kurabayashi, L. L. Howell, and M. S. Baker. Design optimization of a fully-compliant bistable micro-mechanism. In *Proc. 2001 ASME Intl. Mech. Eng. Congress and Exposition*, New York, NY, November 11–16, 2001.

[43] A. Karamchandani and C. A. Cornell. Sensitivity estimation within first and second order reliability methods. *Struct. Saf.*, 11:95–107, 1992.

[44] D. C. Kemeny, L. L Howell, and S. P Magleby. Using compliant mechanisms to improve manufacturability in MEMS. In *Proc. 2002 ASME DETC*, number DETC2002/DFM-34178, 2002.

[45] F. Larsson, P. Hansbo, and K. Runesson. Strategies for computing goal–oriented a posteriori error measures in non–linear elasticity. *Int. J. Numer. Meth. Engrg.*, 55:879–894, 2002.

[46] R. Liu, B. Paden, and K. Turner. MEMS resonators that are robust to process-induced feature width variations. *J. Microelectromech. Syst.*, 11:505–551, 2002.

[47] R. W. Logan and C. K. Nitta. Comparing 10 methods for solution verification, and linking to model validation. *Journal of Aerospace Computing, Information, and Communication*, 3:354–373, 2006.

[48] K. Maute and D. M. Frangopol. Reliability-based design of MEMS mechanisms by topology optimization. *Comput. Structures*, 81:813–824, 2003.

[49] A. Mawardi and R. Pitchumani. Design of microresonators under uncertainty. *J. Microelectromech. Syst.*, 14:63–69, 2005.

[50] J. C. Meza. OPT++: An object-oriented class library for nonlinear optimization. Technical Report SAND94-8225, Sandia National Laboratories, Albuquerque, NM, March 1994.

[51] M. Paraschivoiu and A. Pater. A hierarchical duality approach to bounds for the outputs of partial differential equations. *Comput. Meth. Appl. Mech. Engrg.*, 158:389–407, 1998.

[52] S. Prudhomme and J. T. Oden. On goal-oriented error estimation for elliptic problems: application to the control of pointwise errors. *Comput. Meth. Appl. Mech. Engin.*, 176(1–4):313–331, 1999.

[53] J. Qiu and A. H. Slocum. A curved-beam bistable mechanism. *J. Microelectromech. Syst.*, 13(2):137–146, 2004.

[54] R. Rackwitz. Optimization and risk acceptability based on the Life Quality Index. *Struct. Saf*, 24:297–331, 2002.

[55] R. Rackwitz and B. Fiessler. Structural reliability under combined random load sequences. *Comput. Struct.*, 9:489–494, 1978.

[56] R. Rannacher. Adaptive galerkin finite element methods for partial differential equations. *J. Comput. App. Math.*, 128:205–233, 2001.

[57] R. Ranncher and F.-T. Suttmeirer. A feed–back approach to error control in finite element methods: application to linear elasticity. *Comput. Mech.*, 19:434–446, 1997.

[58] M. Rosenblatt. Remarks on a multivariate transformation. *Ann. Math. Stat.*, 23(3):470–472, 1952.

[59] A.G. Salinger, E.A. Burroughs, R.P. Pawlowski, E.T. Phipps, and L.A. Romero. Bifurcation tracking algorithms and software for large scale applications. *Intl. J. Bifurcation Chaos*, 15(3):1015–1032, 2005.

[60] A. Saltelli, K. Chan, and E. M Scott. *Sensitivity Analysis*. Wiley, New York, 2000.

[61] L. Schenato, W. C. Wu, L. E. Ghaoui, and K. Pister. Process variation analysis for MEMS design. *Proc. SPIE*, 4236:272–279, 2001.

[62] L. R. G Treloar. The elasticity of a network of long-chain molecules I. *Trans. Faraday Soc.*, 39:36–41, 1943.

[63] L. R. G Treloar. The elasticity of a network of long-chain molecules II. *Trans. Faraday Soc.*, 39:241–246, 1943.

[64] J. Tu, K. K. Choi, and Y. H. Park. A new study on reliability-based design optimization. *J. Mech. Design*, 121:557–564, 1999.

[65] Vanderplaats Research and Development, Inc., Colorado Springs, CO. *DOT Users Manual, Version 4.20*, 1995.

[66] L. Wang and R. V. Grandhi. Efficient safety index calculation for structural reliability analysis. *Comput. Struct.*, 52(1):103–111, 1994.

[67] T. Wildey, S. Tavener, and D. Estep. *A posteriori* error estimation of approximate boundary fluxes. in preparation.

[68] J. W. Wittwer. *Simulation-based Design under Uncertainty for Compliant Microelectromechanical Systems*. PhD thesis, Brigham Young University, Salt Lake City, UT, April 2005.

[69] J. W. Wittwer, M. S. Baker, and L. L. Howell. Robust design and model validation of nonlinear compliant micromechanisms. *J. Microelectromechanical Sys.*, 15(1), 2006. to appear.

[70] S. F. Wojtkiewicz, Jr., M. S. Eldred, R. V. Field, Jr., A. Urbina, and J. R. RedHorse. A toolkit for uncertainty quantification in large computational engineering models. In *Proceedings of the 42rd AIAA/ASME/ASCE/AHS/ASC Structures, Structural Dynamics, and Materials Conference*, number AIAA-2001-1455, Seattle, WA, April 16–19, 2001.

[71] Y.-T. Wu. Computational methods for efficient structural reliability and reliability sensitivity analysis. *AIAA J.*, 32(8):1717–1723, 1994.

[72] Y.-T. Wu, H. R. Millwater, and T. A. Cruse. Advanced probabilistic structural analysis method for implicit performance functions. *AIAA J.*, 28(9):1663–1669, 1990.

[73] Y.-T. Wu, Y. Shin, R. Sues, and M. Cesare. Safety-factor based approach for probability-based design optimization. In *Proceedings of the 42rd AIAA/ASME/ASCE/AHS/ASC Structures, Structural Dynamics, and Materials Conference*, number AIAA-2001-1522, Seattle, WA, April 16–19, 2001.

[74] Y.-T. Wu and P. H. Wirsching. A new algorithm for structural reliability estimation. *J. Eng. Mech., ASCE*, 113:1319–1336, 1987.

[75] S. Xu and R. V. Grandhi. Effective two-point function approximation for design optimization. *AIAA J.*, 36(12):2269–2275, 1998.

[76] O. C. Zienkiewicz and J. Z. Zhu. A simple error estimator and adaptive procedure for practical engineering analysis. *Int. J. Num. Meth. Eng.*, 24:337–357, 1987.

[77] T. Zou, S. Mahadevan, and R. Rebba. Computational efficiency in reliability-based optimization. In *Proceedings of the 9th ASCE Specialty Conference on Probabilistic Mechanics and Structural Reliability*, Albuquerque, NM, July 26–28, 2004.

DISTRIBUTION:

1 Ivo Babuška
ICES
1 University Station, C0200
Austin, Texas 78712

1 Graham F. Carey
ICES
1 University Station, C0200
Austin, Texas 78712

1 Donald J. Estep
Department of Mathematics
101 Weber Building
Colorado State University
Fort Collins, CO 80523-1874

1 Marc Garbey
Dept. of Computer Science
501 Philipp G-Hoffman Hall, Room 210
University of Houston
Houston, TX 77204-3010

1 Roger Ghanem
254C Kaprielian Hall
Dept. of Civil Engineering
3620 S. Vermont Ave.
University of Southern California
Los Angeles, CA 90089-2531

1 Raphael Haftka
Dept. of Aerospace and Mechanical Engineering and Engineering Science
P.O. Box 116250
University of Florida
Gainesville, FL 32611-6250

1 Richard Hills
New Mexico State University
College of Engineering, MSC 3449
P.O. Box 30001
Las Cruces, NM 88003

1 Michael J. Holst
Department of Mathematics
Dept. 0112 APM 5739
9500 Gilman Drive
La Jolla, CA 92093-0112

1 Sankaran Mahadevan
Department of Civil and Environmental Engineering
Box 1831, Station B
Vanderbilt University
Nashville, TN 37235

1 Kurt Maute
Department of Aerospace Engineering Sciences
University of Colorado at Boulder
Room ECAE 183, Campus Box 429
Boulder, Colorado 80309-0429

1 J. Tinsley Oden
ICES
1 University Station, C0200
Austin, Texas 78712

1 John E. Renaud
University of Notre Dame
Aerospace and Mechanical Engineering
365 Fitzpatrick Hall
Notre Dame, IN 46556-5637

1 Christopher J. Roy
Department of Aerospace Engineering
211 Aerospace Engineering Bldg.
Auburn University
Auburn, AL 36849-5338

1 Simon J. Tavener
Department of Mathematics
101 Weber Building
Colorado State University
Fort Collins, CO 80523-1874

1 Steven F. Wojtkiewicz, Jr.
Department of Civil Engineering
University of Minnesota
500 Pillsbury Drive S.E.
Minneapolis, MN 55455-0116

7 Lawrence Livermore National Laboratory
7000 East Ave.
P.O. Box 808
Livermore, CA 94550
Attn: Scott Brandon, MS L-023
Frank Graziani, MS L-095
Richard Klein, MS L-023
Roger Logan, MS L-125
Jim McEnerney, MS L-023
Cynthia Nitta, MS L-096
Charles Tong, MS L-560

3 Los Alamos National Laboratory
Mail Station 5000
P.O. Box 1663
Los Alamos, NM 87545
Attn: Marc Anderson, MS T080
Scott Doebling, MS T080
Francois Hemez, MS T006

1 MS 0139 A. L. Hale, 1900

1 MS 0139 P. Yarrington, 1902

1 MS 0139 R. K. Thomas, 1904

1 MS 0316 S. A. Hutchinson, 1437

1 MS 0316 E. R. Keiter, 1437

1 MS 0316 J. N. Shadid, 1437

1 MS 0370 T. G. Trucano, 1411

1 MS 0380 J. Jung, 1542

1 MS 0380 H. S. Morgan, 1540

3 MS 0382 B. Carnes, 1543

3 MS 0382 K. D. Copps, 1543

1 MS 0382 S. W. Bova, 1541

1 MS 0382 C. Newman, 1541

1 MS 0382 S. E. Gianoulakis, 1541

1 MS 0382 D. C. Neckels, 1543

1 MS 0382 J. R. Stewart, 1543

1 MS 0382 S. R. Subia, 1541

1 MS 0557 T. L. Paez, 1533

1 MS 0779 J. C. Helton, 1533

1 MS 0826 D. J. Rader, 1513

1 MS 0828 K. Dowding, 1533

1 MS 0828 A. A. Giunta, 1533

1 MS 0828 W. L. Oberkampf, 1533

1 MS 0828 M. Pilch, 1533

1 MS 0828 J. R. Red-Horse, 1533

1 MS 0828 V. J. Romero, 1533

1 MS 0836 R. E. Hogan, 1516

1 MS 0836 J. S. Lash, 1514

3 MS 0836 M. M. Hopkins, 1514

3 MS 0836 P. K. Notz, 1514

1 MS 0847 R. V. Field, 1526

1 MS 1064 J. A. Mitchell, 2614

1 MS 1069 J. W. Wittwer, 1769-1

1 MS 1069 M. R. Platzbecker, 1769-1

1 MS 1243 S. N. Kempka, 5535

1 MS 1318 B. M. Adams, 1411

3 MS 1318 B. J. Bichon, 1411

3 MS 1318 M. S. Eldred, 1411

1 MS 1318 P. Knupp, 1411

1 MS 1318 S. A. Mitchell, 1411

1 MS 1318 L. P. Swiler, 1411

1 MS 1318 D. E. Womble, 1410

1 MS 1320 S. S. Collis, 1414

| | | | |
|---|---|---|---|
| 1 | MS | 9051 | B. J. Debusschere, 8351 |
| 1 | MS | 9051 | H. Najm, 8351 |
| 1 | MS | 9159 | H. R. Ammerlahn, 8962 |
| 1 | MS | 9159 | P. D. Hough, 8962 |
| 1 | MS | 9159 | M. L. Martinez-Canales, 8962 |
| 2 | MS | 9018 | Central Technical Files, 8944 |
| 2 | MS | 0899 | Technical Library, 4536 |